

Supersymmetry with Multijet Events at CMS: an Experimental Strategy

Dissertation

zur

Erlangung der naturwissenschaftlichen Doktorwürde
(Dr. sc. nat.)

vorgelegt der

Mathematisch-naturwissenschaftlichen Fakultät

der

Universität Zürich

von

Tanja Rommerskirchen

aus

Deutschland

Promotionskomitee

Prof. Dr. C. Amsler (Vorsitz)

Prof. Dr. V. Chiochia

Dr. A. Schmidt

Dr. S. de Visscher

Zürich, 2010

Abstract

In 2010 the LHC has started to collide protons with center-of-mass energies of 7 TeV and 10 TeV will be reached in the coming years. These high energies allow to search for new phenomena beyond the current experimental limits. In this thesis a search strategy for a missing energy signature compatible with cold dark matter is presented, using event topologies with exactly 2 to 6 hadronic jets. Missing energy signatures are predicted by many models beyond the Standard Model, e.g. R -parity conserving Supersymmetry. The missing energy is due to high momenta particles which do not, or only very weakly, interact with the detector material and are therefore not detected. This undetected particles lead to typical distributions of the relative momenta and the angular distance of jets. Four kinematic variables are introduced in this thesis which exploit jet kinematics to discriminate against the dominant background from QCD multi-jet events. The variables are compared in terms of their signal sensitivity but also their robustness against systematic uncertainties. The main emphasis of this approach is on developing a robust analysis technique that is suited to the early collision data at the LHC.

The expected event yields are reported for selected low mass SUSY parameter sets and the Standard Model backgrounds for a data sample of 100 pb^{-1} at a center-of-mass energy of 10 TeV. A discovery of SUSY with the LM1 mSuGra parameter-set would be possible with an integrated luminosity of $\mathcal{L} = 39_{-10}^{+21+31} \text{ pb}^{-1}$ for dijet events and with $\mathcal{L} = 25 + 19_{-4}^{+6} \text{ pb}^{-1}$ for events with more jets. Taking into account the current center-of-mass energy of the LHC of 7 TeV the corresponding luminosities could be reached in less than a year.

In future tagging b -quarks with the CMS pixel detector will become important for SUSY and other searches. Therefore pixel detector measurements made with data from cosmic muon showers are compared to the predictions of Monte Carlo simulations.

Zusammenfassung

Im Jahr 2010 hat der LHC damit begonnen, Protonen mit einer Schwerpunktsenergie von 7 TeV kollidieren zu lassen, 10 TeV sollen in den kommenden Jahren erreicht werden. Diese hohen Energien erlauben die Suche nach neuen Phänomenen jenseits der heutigen experimentellen Ausschlussgrenzen. In dieser Doktorarbeit wird eine Strategie zur Suche nach Ereignissen mit fehlender transversaler Energie, der Signatur von kalter dunkler Materie, entwickelt. Ereignisse mit fehlender transversaler Energie werden von vielen Modellen jenseits des Standardmodells der Teilchenphysik vorhergesagt, z.B. R -Paritäts erhaltende Supersymmetrie (SUSY). Die fehlende Energie in der Messung stammt dabei von hochenergetischen Teilchen die nicht, oder nur schwach, mit dem Detektor interagieren. Es resultieren daraus typische Verteilungen der relativen Impulse und Winkelabstände von Jets. Vier Variablen, die die Kinematik von Jets nutzen um den dominanten Untergrund durch QCD Vieljetereignisse zu unterdrücken, werden in dieser Doktorarbeit eingeführt. Die Variablen werden in Bezug auf ihre Signalsensitivität aber auch ihrer Robustheit gegen systematische Unsicherheiten verglichen. Das Hauptaugenmerk dieses Ansatz ist die Entwicklung einer robusten Technik die sich für die Analyse der ersten Kollisionsdaten des LHC eignet.

Die erwartete Anzahl von selektierten Ereignissen, bei einer integrierten Luminosität von 100 pb^{-1} und einer Schwerpunktsenergie von 10 TeV, wird für eine Auswahl von SUSY Parametersätzen und Standardmodell Untergründen angegeben. Eine Entdeckung von SUSY, falls es mit dem LM1 mSuGra Parametersatz realisiert ist, sollte mit einer integrierten Luminosität von $\mathcal{L} = 39_{-10}^{+21+31} \text{ pb}^{-1}$ für Ereignisse mit zwei Jets und mit $\mathcal{L} = 25 + 19_{-4}^{+6} \text{ pb}^{-1}$ für Ereignisse mit mehr Jets möglich sein. Wird die tatsächliche aktuelle Schwerpunktsenergie des LHC von 7 TeV in Betracht genommen, sollten die nötigen Luminositäten in weniger als einem Jahr erreichbar sein.

In der Zukunft wird das "taggen" von b -quarks wichtig werden, für SUSY Suchen aber auch für andere Analysen. Aus diesem Grund werden Pixeldetektormessungen für kosmische Muonen mit den Vorhersagen durch Monte Carlo Simulationen verglichen.

Contents

Abstract	i
Zusammenfassung	iii
Introduction	1
1 Supersymmetry	3
1.1 Introduction	3
1.2 Minimal Particle Content of a Supersymmetric Theory	5
1.3 General Soft Broken SUSY	6
1.4 SUSY Phenomenology	7
2 LHC and the CMS Detector	13
2.1 Physics at Proton - Proton Colliders	13
2.2 LHC Design	15
2.3 CMS Detector	17
2.3.1 Muon System	18
2.3.2 Hadron Calorimeter	18
2.3.3 Electromagnetic Calorimeter	20
2.3.4 Inner Tracking System	21
2.4 Comparison of Cosmic Ray Data with Simulation	25
3 From Event Generation to Reconstruction	31
3.1 Event Generators	32
3.2 Reconstruction	34
3.2.1 Jet Reconstruction	35
3.2.2 Jet Energy Corrections	36
3.2.3 Jet Quality Criteria	38
3.2.4 Muon Reconstruction	38
3.2.5 Muon Isolation	39
3.2.6 Muon Quality Criteria	40
3.2.7 Electron Reconstruction	41
3.2.8 Electron Isolation	41
3.2.9 Missing Transverse Energy (calorimeter based)	42
3.2.10 Trigger and Data Acquisition	44

4	Supersymmetry in Multijet Events	45
4.1	Monte Carlo Data Samples	45
4.1.1	Signal	45
4.1.2	Background	45
4.2	Kinematic Quantities	46
4.3	Properties of mSuGra Points	47
4.4	Online Selection	51
4.5	Object Definition	51
4.6	Offline Preselection	54
4.7	Final Variables	55
4.7.1	Dependence on Jet-Multiplicity	64
4.8	First Method to Quantify the Statistical Significance of a Signal	67
4.9	Systematic Uncertainties and Statistical Significance	69
4.9.1	Choice of Final Selection Cuts	70
4.9.2	Uncertainties on Event Yields	74
4.9.3	Conclusion	75
4.10	Background and Signal Composition after the Event Selection	77
4.11	A Second Method for Evaluating the Signal Significance	79
4.11.1	Introduction	79
4.11.2	The Profile-Likelihood Method	81
4.11.3	Systematic Uncertainties	84
4.11.4	Calculating a Statistical Significance	86
4.11.5	Conclusion and Prospects	86
5	Conclusions and Prospects	89
A		91
A.1	Coordinate System	91
A.1.1	Global Coordinate System	91
A.1.2	Local Pixel Coordinate System	92
A.2	Kinematic Quantities	93
A.3	Abbreviations	94
B		95
B.1	Quantification of the Sensitivity of a Search for New Phenomena	95
B.2	Control Distributions	96
B.3	Event yields after Detector Performance Degradations	100
	Bibliography	101

Introduction

In the year 2010 the Large Hadron Collider (LHC) [1] at the European laboratory for Particle Physics CERN has started to collide protons at a center of mass energy of 7 TeV. This energy will be increased to 10 or even 14 TeV in the following years. The LHC is the most powerful particle accelerator in the world. Four large experiments (CMS [2], ATLAS [3], LHCb [4] and ALICE [5]) and two small angle scattering experiments (TOTEM [6] and LHCf [7]) monitor and analyze the particles produced in proton collisions. The purpose of these experiments is to understand the properties and interactions of the smallest constituents of matter and to test the Standard Model (SM) of particle physics [8]. The SM retraces the complexity of particle interactions found in several experiments to a few fundamental symmetries, called local gauge symmetries. In this model particles interact by exchanging gauge bosons. The SM is currently the best description of the subatomic world. However, it incorporates only three out of the four fundamental forces, omitting gravity. In addition, open questions such as the nature of dark matter [9] and the Hierarchy Problem [10] pose potential difficulties to the SM. It is therefore widely believed that it is only part of a broader picture that includes new physics.

Supersymmetry (SUSY) [10] is one of the possible extensions of the SM, which solves not only the Hierarchy Problem but can under certain conditions (R -parity conservation) provide a lightest stable particle compatible with expectations from dark matter searches [9]. SUSY theories introduce a wide range of new heavy particles. Their masses and couplings depend on a set of free parameters. Previous searches at lepton and hadron colliders excluded a range of possible parameter-sets [11]. The experiments at the LHC will extend the current exclusion limits or discover SUSY.

This thesis focusses on the SUSY discovery potential with the CMS detector and early LHC data at a center of mass energy of 10 TeV. It concentrates on events with large missing energy and multiple high momentum jets, as predicted by most R -parity conserving SUSY scenarios which provide heavy colored particles such as gluinos (\tilde{g}) and squarks (\tilde{q}). It is sensitive to a wide range of parameter-sets. The relatively high cross-section associated to the production of heavy colored particles makes the analysis suitable for early data.

A jet based search is particularly challenging at a hadron collider owing to the overwhelmingly large cross-section of QCD multijet production and also to the systematic uncertainty in the jet energy resolution of the detector. A large part of the presented analysis is therefore dedicated to the task of understanding and controlling this uncertainty.

This thesis starts with an introduction to the theory of particle physics presenting the SM and SUSY. The dependence of the SUSY phenomenology on the mass of squarks and gluinos is discussed. Chapter 2 describes the experimental setup used in this analysis, the "hardware" of the CMS detector. A special part of this chapter is dedicated to a comparison of the predicted and the measured charge deposited by cosmic ray muons in the pixel detector. This comparison has been made with 2008 data. Chapter 3 describes the various tools necessary to span the gap between intricate theoretical models and the actual expected output of the detector. The reconstruction, energy correction and quality criteria of jets employed in this analysis are discussed in great detail. In chapter 4 the complete analysis strategy from online selection to statistical interpretation is presented. After a common pre-selection the performance of several kinematic variables is studied. The variables are compared in terms of their signal sensitivity and their robustness against systematic uncertainties. In addition, a new robust method for evaluating a signal significance is presented. All variables are given in natural units.

This thesis is an extension of my contribution to the following publications:

- "SUSY searches with dijet events", CMS Collaboration, CMS PAS SUS-08-005, (2008)
- "Search strategy for exclusive multi-jet events from Supersymmetry at CMS", CMS Collaboration, CMS PAS SUS-09-001, (2009)

Chapter 1

Supersymmetry

1.1 Introduction

The Standard Model (SM) is the established theory of Particle Physics. It deals with the basic building blocks of matter and their interactions. At scales smaller than 1 fm even protons and neutrons, the constituents of atomic nuclei, do not appear as pointlike, but can be found to consist of other particles, the quarks. Until now no substructure of quarks has been discovered [11]. Therefore they are assumed to be elementary fermions. Electrons and neutrinos are another kind of fermions which are also assumed to be elementary. An overview on the fundamental fermions in the SM is given in Table 1.1. To each of these fermions belongs an anti-particle with the same mass but opposite charge. The forces between fermions are carried by particles with an integer spin, the gauge bosons.

Table 1.1: The different fermions and their electrical charges

class	family			electrical charge [e]
	I	II	III	
leptons	e	μ	τ	1
	ν_e	ν_μ	ν_τ	0
quarks	u	c	t	2/3
	d	s	b	-1/3

The interactions between fermions and bosons are described by gauge theories. Extensive information about the SM and gauge theories in particular can be found in the literature e.g. in the books of P. Schmüser [12] and C. Berger [8].

One of the problems of gauge theories is that they predict massless W and Z gauge bosons, which is in contradiction to experimental observations. One of the simplest ways of explaining massive gauge bosons, and keeping the concept of gauge theories as well, is the Higgs mechanism. It predicts an additional particle, the Higgs boson. By interacting with the Higgs field bosons and fermions acquire mass. The SM Higgs mechanism works only if the Higgs mass is less than ~ 1 TeV [12].

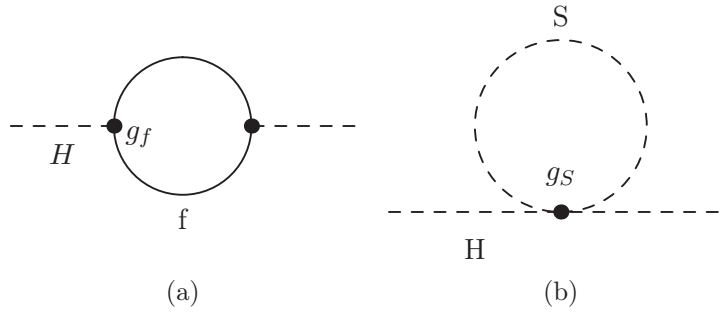


Figure 1.1: One-loop quantum corrections to the Higgs squared mass parameter m_H^2 , due to (a) a Dirac fermion, and (b) a scalar S .

Radiative corrections such as those shown in Fig. 1.1 change the Higgs boson mass m_H by Δm_H :

$$\Delta m_H^2 = -\frac{|g_f|^2}{8\pi^2} \Lambda^2 + \dots, \quad (1.1)$$

where Λ is an energy cutoff, to prevent the correction from becoming infinite and g_f is the coupling constant for the coupling of a fermion f to the Higgs boson. Physically Λ could be interpreted as the scale where new physics alters the high energy behaviour of the theory. This could be any scale between the electro-weak scale M_W and the Planck scale $M_{Pl} = 1.2 \times 10^{19}$ GeV. Such radiative corrections could increase the Higgs mass to values much larger than 1 TeV.

Similar corrections arise from boson loops corresponding to Fig. 1.1 (b), where a complex scalar particle S interacts with the Higgs boson. The correction to the Higgs boson mass is the following [10]:

$$\Delta m_H^2 = \frac{g_S}{16\pi^2} [\Lambda^2 - 2m_S^2 \ln(\Lambda/m_S) + \dots], \quad (1.2)$$

where g_S is the coupling constant for the coupling of a scalar to the Higgs field and m_S is the mass of the scalar. If each fermion is accompanied by two complex scalars with $g_S = |g_F|^2$ the quadratic divergences proportional to Λ^2 in equation 1.1 and 1.2 cancel each other. Such a relation between couplings of fermions and bosons would stabilize the Higgs mass and exists naturally in the context of Supersymmetry (SUSY).

A more detailed discussion of the problem introduced by unknown heavy particles and their direct or indirect interaction with the Higgs field can be found in Ref. [10]. The following summary of SUSY is also based on this Reference. SUSY is a symmetry¹ which relates the masses and couplings of bosons and fermions. A supersymmetric transformation Q turns a bosonic state into a fermionic state and vice versa:

¹Feynman: "A thing is symmetrical, if there is something we can do to it so that after we have done it, it looks the same as before."

$$\begin{aligned}
 Q|\text{Boson} \rangle &\sim |\text{Fermion} \rangle \\
 Q|\text{Fermion} \rangle &\sim |\text{Boson} \rangle
 \end{aligned}
 \tag{1.3}$$

Where Q is the generator of SUSY. An unbroken supersymmetric theory should be invariant under such a transformation.

1.2 Minimal Particle Content of a Supersymmetric Theory

The irreducible representations of the SUSY algebra are supermultiplets containing fermions and bosons which can be transformed into each other by supersymmetric transformations. The fermions and bosons thus associated to each other are called superpartners. The dimensionless couplings of fermions and associated scalars are related to each other by:

$$g_S = |g_f|^2. \tag{1.4}$$

This is needed to cancel the quadratic divergences of the Higgs boson mass from fermion loops (Sect. 1.1). In an unbroken supersymmetric theory these superpartners have the same mass, electric charge, weak isospin and color degrees of freedom. Each supermultiplet contains the same number of fermionic (n_F) and bosonic (n_B) degrees of freedom. Two kinds of supermultiplets can be distinguished, chiral and gauge supermultiplets.

The chiral supermultiplets contain the SM fermions which have two spin helicity states ($n_F = 2$) and their associated scalars (spin 0 bosons). The left- and right-handed fermions have each their own scalar partner ($n_B = 2$). The names of the scalars are constructed by prepending an s to the name of the associated SM fermion. The symbols of the bosons are denoted by drawing a tilde above the symbol for the associated fermion, e.g. squark, \tilde{q} .

The gauge supermultiplets contain the SM gauge fields (spin 1 bosons), which have two helicity states ($n_B = 2$) if the bosons are massless, and their associated supersymmetric spin 1/2 fermions. In order to allow for a renormalizable theory the vector bosons need to be massless, at least before the gauge symmetry is spontaneously broken. The left and right handed components of particles in a gauge supermultiplet have the same gauge transformation properties. The names for the supersymmetric fermions are constructed by prepending an *ino* to the name of the associated SM boson. The symbols of the fermions are denoted by the same symbol as the bosonic supersymmetric partner but with a tilde on top, e.g. gluino, \tilde{g} .

The minimal set of particles necessary to construct a supersymmetric theory are given in Table 1.2 for chiral supermultiplets and in Table 1.3 for gauge supermultiplets. Models containing only these particles are called MSSM (Minimal Supersymmetric Standard Models). The tables employ the two-component Weyl spinor notation. The Weyl notation simply writes the four-component Dirac spinor ψ_D in terms of two two-component spinors, a left-handed Weyl spinor and a right-handed Weyl spinor. The hermitian conjugate of any left-handed Weyl spinor is a right-handed Weyl spinor. By convention, all chiral supermultiplets are defined in terms of left-handed Weyl spinors. Only the conjugates of right-handed quarks, leptons and their superpartners appear therefore in this table.

Table 1.2: Chiral supermultiplets in the MSSM. The spin-0 fields are complex scalars, and the spin-1/2 fields are left-handed Weyl fermions [10].

Names	spin 0	spin 1/2	SU(3) _C , SU(2) _L , U(1) _Y
squarks, quarks (x 3 families)	$(\tilde{u}_L, \tilde{d}_L)$	(u_L, d_L)	$(\mathbf{3}, \mathbf{2}, \frac{1}{6})$
	\tilde{u}_R^*	u_R^\dagger	$(\bar{\mathbf{3}}, \mathbf{1}, -\frac{2}{3})$
	\tilde{d}_R^*	d_R^\dagger	$(\bar{\mathbf{3}}, \mathbf{1}, \frac{1}{3})$
sleptons, leptons (x 3 families)	$(\tilde{\nu}, \tilde{e}_L)$	(ν, e_L)	$(\mathbf{1}, \mathbf{2}, -\frac{1}{2})$
	\tilde{e}_R^*	e_R^\dagger	$(\mathbf{1}, \mathbf{1}, 1)$
Higgs, higgsinos	(H_u^+, H_u^0)	$(\tilde{H}_u^+, \tilde{H}_u^0)$	$(\mathbf{1}, \mathbf{2}, +\frac{1}{2})$
	(H_d^0, H_d^-)	$(\tilde{H}_d^0, \tilde{H}_d^-)$	$(\mathbf{1}, \mathbf{2}, -\frac{1}{2})$

Table 1.3: Gauge supermultiplets in the MSSM.

Names	spin 1/2	spin 1	SU(3) _C , SU(2) _L , U(1) _Y
gluino, gluon	\tilde{g}	g	$(\mathbf{8}, \mathbf{1}, 0)$
winos, W-bosons	$\tilde{W}^\pm, \tilde{W}^0$	W^\pm, W^0	$(\mathbf{1}, \mathbf{3}, 0)$
binos, B-bosons	\tilde{B}^0	B^0	$(\mathbf{1}, \mathbf{1}, 0)$

General supersymmetric theories conserve neither baryon nor lepton number thus allowing in principle disastrous proton decays. Many supersymmetric models therefore prohibit these decays by requiring R -parity conservation,

$$R = (-1)^{3(B-L)+2S} = \text{const.} \quad (1.5)$$

where B, L and S are the baryon number, lepton number and spin. All SM particles and the Higgs bosons have R -parity $R = +1$, while all of the squarks, sleptons, gauginos and higgsinos have R -parity $R = -1$. The consequence of R -parity conservation is that SUSY-particles are produced in pairs and that the lightest SUSY particle (LSP) is stable, and therefore a good candidate for dark matter [9].

1.3 General Soft Broken SUSY

In an unbroken supersymmetric theory SM particles and their superpartners have the same mass. This is in contradiction to experimental results, as no such superpartners have been found. Therefore SUSY must be broken.

To preserve SUSY as cure for the Higgs hierarchy problem (Sect. 1.1) the relationship between the dimensionless couplings of fermions and their superpartners $g_s = |g_f|^2$ needs to be maintained.

One possible solution is "soft" SUSY breaking, i.e. to have an effective Lagrangian which splits into a SUSY preserving part L_{SUSY} containing all the gauge and Yukawa interactions

and a term L_{soft} which violates SUSY and contains all allowed terms that do not introduce quadratic divergences in the theory [13]:

$$L = L_{SUSY} + L_{soft}. \quad (1.6)$$

Remaining corrections to the Higgs mass must be of the form (Eq.: 1.2 and 1.1):

$$\Delta m_H^2 = m_{soft}^2 \left[\frac{\lambda}{16\pi^2} \ln(\Lambda/m_{soft}) + \dots \right], \quad (1.7)$$

if SUSY is broken "softly". Here m_{soft} is the largest mass scale associated with the soft terms and λ is generic for various dimensionless couplings. The dots in the equation represent terms that are independent of Λ (the momentum space cutoff introduced in Sect. 1.1) and higher loop corrections which depend on Λ through powers of logarithms. In order to conserve SUSY as cure for the Hierarchy Problem m_{soft} cannot be too large. Assuming $\Lambda \sim M_P$ and $\lambda \sim 1$ one finds that m_{soft} should be about 1 TeV in order to agree with current experimental upper limits on the mass of the W and Z bosons without introducing a fine-tuning problem [10]. Should m_{soft} , and therefore also the masses of at least the lightest superpartners, really be of the order of 1 TeV, experiments at the CERN Large Hadron Collider would stand a chance to discover SUSY.

Once SUSY and electroweak symmetry are broken, particles with the same quantum number will in general mix. Neutral gauginos (\tilde{B} and \tilde{W}^0) and higgsinos (\tilde{H}_u^0 and \tilde{H}_d^0) mix and form four mass eigenstates called neutralinos $\tilde{\chi}_i^0$ ($i = 1, 2, 3, 4$). The charged higgsinos (\tilde{H}_u^+ and \tilde{H}_d^-) and winos (\tilde{W}^+ and \tilde{W}^-) mix and form two mass eigenstates with charge = ± 1 called charginos $\tilde{\chi}_i^\pm$ ($i = 1, 2$). By convention, these mass eigenstates are labeled in ascending order, so that $m_{\tilde{\chi}_1^0} < m_{\tilde{\chi}_2^0} < m_{\tilde{\chi}_3^0} < m_{\tilde{\chi}_4^0}$ and $m_{\tilde{\chi}_1^\pm} < m_{\tilde{\chi}_2^\pm}$. The lightest neutralino, $\tilde{\chi}_1^0$, is usually assumed to be the LSP, unless there is a lighter gravitino or unless R -parity is not conserved. It is the only MSSM particle that can make a good dark matter candidate [10]. The Higgs scalar mass eigenstates consist of two CP-even neutral scalars h^0 and H^0 , one CP-odd neutral scalar A^0 , and a charge +1 scalar H^+ and its conjugate a charge -1 scalar H^- .

1.4 SUSY Phenomenology

Due to inclusion of the additional mass terms in L_{soft} , necessary for breaking SUSY, the general MSSM contains more than 100 parameters (masses, phases and mixing angles). Hence it is nearly impossible to study the complete parameter space of MSSM. To estimate the ability of the CMS detector to discover SUSY special constrained models are chosen as guidelines of what to expect if SUSY is realized in nature.

One of these constrained models is mSuGra (minimal Super Gravity) [10]. The speciality of mSuGra is that it requires all squarks, sleptons, and Higgs bosons to have a common mass m_0 and all gauginos to have a common mass $m_{1/2}$ at the GUT [14] scale. Mass splitting between these particles occurs when the masses are evaluated at the weak scale using the Renormalization Group Equations (RGE) [15]. This feature of mSuGra makes it the

SUSY model with the least number of parameters. The five parameters which characterize a point in the mSuGra space are commonly chosen as m_0 , $m_{1/2}$, $\text{sign}(\mu)$, A_0 , $\tan\beta$. The parameter A_0 is the common value of the Higgs-sfermion-sfermion coupling, μ the SUSY conserving Higgs mass and $\tan\beta$ is the ratio of the vacuum expectation values of the two MSSM Higgs doublets.

The dominant sparticle production mechanism in a proton-proton collider like the LHC is for most SUSY models gluon-gluon and gluon-quark fusion as presented in Fig. 1.2. The relative contributions of the depicted production processes vary for the different parameter sets. The corresponding cross-sections can be found in Ref. [16]. Should for example SUSY be realized with the parameter-set LM1, the gluino would be heavier than any of the squarks, the production of $\tilde{q}\tilde{g}$ (Fig. 1.2 d - f) would be dominant (52%) and the second leading contribution would be squark-pair production (Fig. 1.2 g - j) with 29% [16]. The relative contributions of decay processes depend on the parameter sets as well, e.g. at LM1 the dominant decay process of the gluino would be $\tilde{g} \rightarrow q\tilde{q}$. This decay is always dominant when kinematically allowed. If gluinos are heavier than any of the squarks the decay chain of the produced sparticles is expected to be [16]:

$$\tilde{g} \rightarrow \tilde{q}\bar{q}, \tilde{q} \rightarrow q\tilde{\chi}. \quad (1.8)$$

For gluinos lighter than any of the squarks a typical decay chain would be instead:

$$\tilde{q} \rightarrow \tilde{g}q, \tilde{g} \rightarrow q\bar{q}\tilde{\chi}. \quad (1.9)$$

When some of the squarks are lighter and some heavier than the gluino the possible decay chains become more complicated. Fig. 1.3 shows two possible cascade decays of the gluino into the final LSP. The experimental signature corresponding to these decay chains, typical for a wide range of parameter-sets in R -parity conserving MSSM SUSY models, is:

1. Large missing energy originating from the two lightest stable particles in the final states of the squark and gluino decays. These lightest stable particles are assumed to be neutral in accord with cosmological arguments [9]. They would therefore not interact with the detector and remain undetected.
2. Multiple jets produced in the hadronic decays of the squarks and gluinos. Due to the mass difference between the primary SUSY particles and their decay products these jets are commonly of high momenta.
3. Multiple leptons produced in cascade decays like the one shown in Fig. 1.3 (b).

R -parity conserving SUSY events are characterized by their signature as n leptons + m jets + \cancel{E}_T , where $m, n \geq 0$, and \cancel{E}_T is the component of missing transverse energy emitted transverse to the beam pipe. In hadron colliders only the transverse component of the missing energy is a meaningful observable. To discover SUSY and identify in which way SUSY is realized in nature, it is necessary to cover as many of the various signatures ($n = 0, 1, \dots$ and $m = 0, 1, \dots$) as possible.

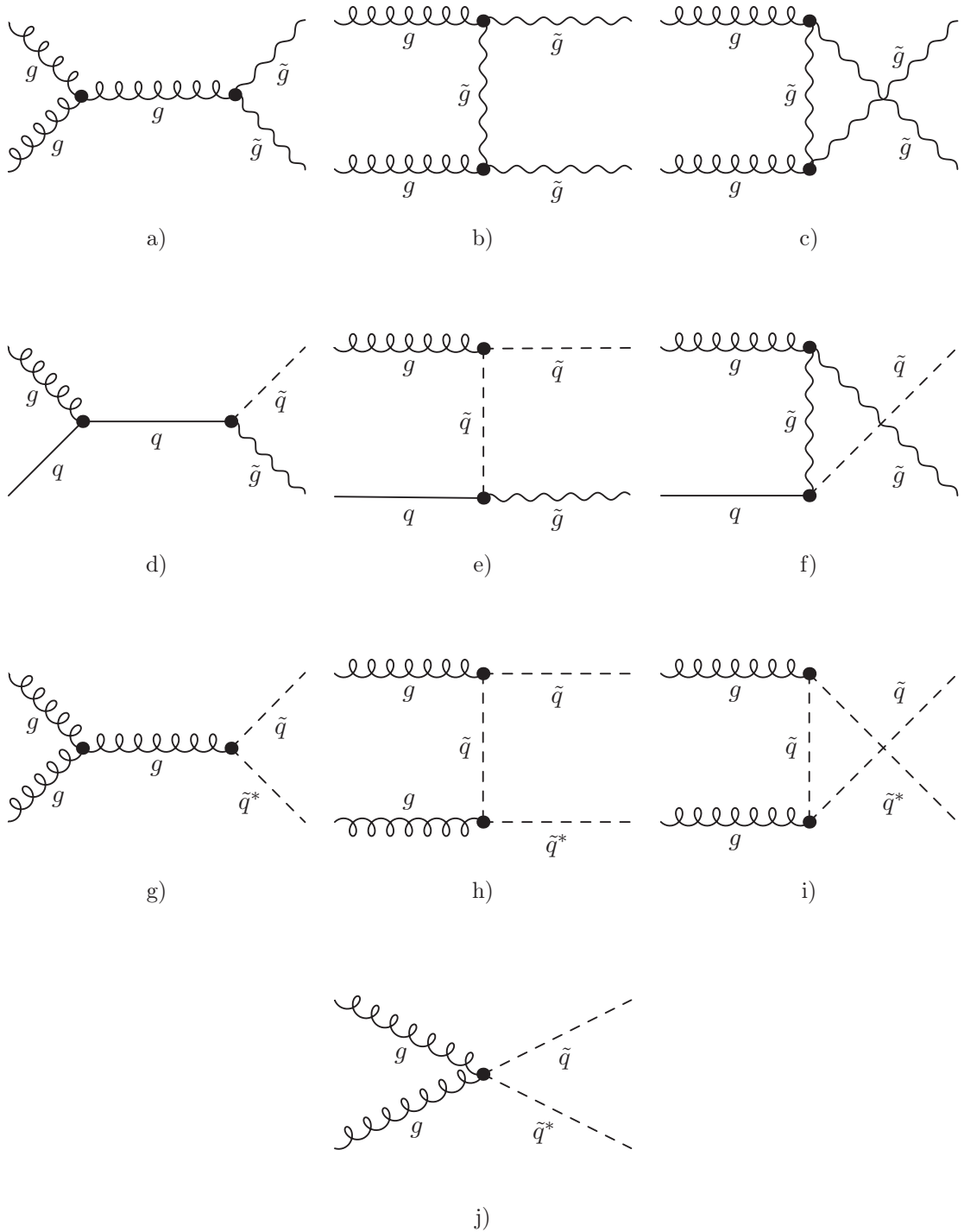


Figure 1.2: Feynman diagrams for gluino and squark production at hadron colliders from gluon-gluon and gluon-quark fusion. These production mechanisms are dominant at proton-proton colliders for most SUSY models [10].

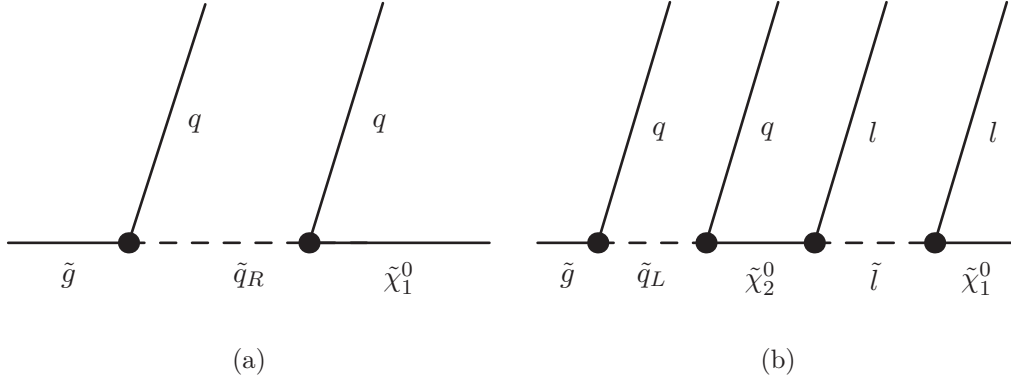


Figure 1.3: Two of the many possible examples of gluino cascade decays [10].

At the e^+e^- collider LEP at CERN (1989 - 2000) and the Tevatron [17] $p\bar{p}$ collider located at Fermilab searches for these topologies have been conducted and the results have been interpreted in terms of the mSuGra and other SUSY models [11]. The resulting limits within the mSuGra framework are presented in Fig. 1.4(a) for the CDF experiment in the $(m_{\tilde{g}}, m_{\tilde{q}})$ plane and in Fig. 1.4(b) for the D0 experiment in the $(m_0, m_{1/2})$ plane for fixed values of A_0 , $\tan\beta$ and μ . The theoretical limits shown in this figure correspond to parameter combinations which don't allow for a valid mSuGra solution or for electroweak symmetry breaking. The presented CDF and D0 limits result from squark and gluino searches in multi-jet final states with missing transverse energy. The LEP limits have been obtained from slepton and chargino searches assuming squark and slepton mass unification. The chargino decays, in the mass range accessible at LEP energies, are mediated by virtual W and sfermion exchange. Chargino searches have been conducted for all-hadronic $(q\bar{q}'q\bar{q}'\tilde{\chi}_1^0\tilde{\chi}_1^0)$, mixed $(q\bar{q}'l\nu\tilde{\chi}_1^0\tilde{\chi}_1^0)$ and fully leptonic $(l\nu l\nu\tilde{\chi}_1^0\tilde{\chi}_1^0)$ topologies, no excess over SM background has been observed. Slepton searches at LEP have been conducted for final states consisting either of two leptons whose difference in azimuth is smaller than 180° or of one single energetic electron. Two lepton final states are expected for pair-produced sleptons which decay into a lepton and a LSP. The derived limits depend on the mass of the LSP $m_{\tilde{\chi}_1^0}$.

- Smuon masses below 95 GeV to 99 GeV (depending on $m_{\tilde{\chi}_1^0}$) are excluded if the $\tilde{\mu}_R - \tilde{\chi}_1^0$ mass difference is larger than 5 GeV.
- Stau masses smaller than 86 to 95 GeV are excluded, if the stau- $\tilde{\chi}_1^0$ mass difference is larger than 7 GeV.
- Selectron masses below 100 GeV are excluded for $m_{\tilde{\chi}_1^0} < 85$ GeV.

A limit of 73 GeV on the selectron mass can be deduced from the search for a single energetic electron as expected for associated $\tilde{e}_R\tilde{e}_L$ production. This limit is independent of $m_{\tilde{\chi}_1^0}$.

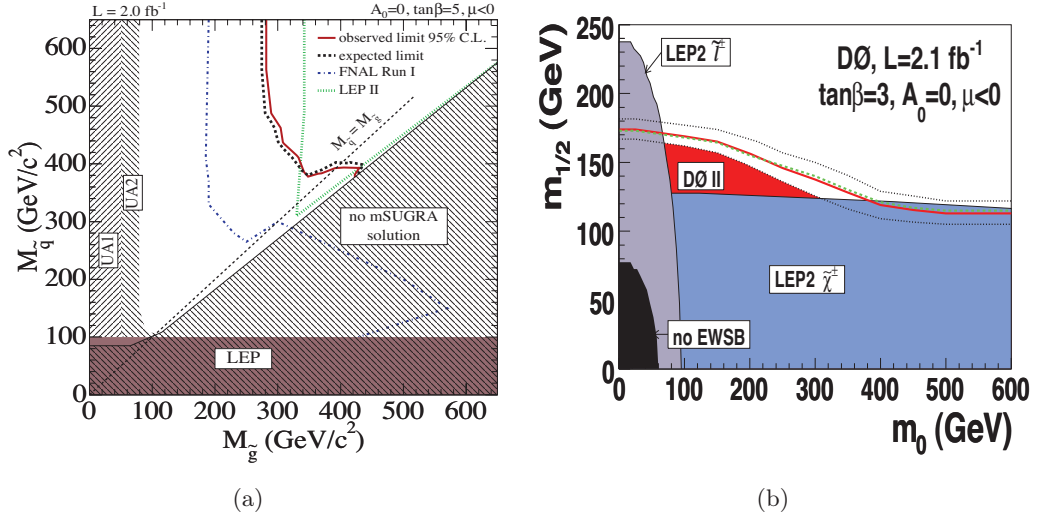


Figure 1.4: Regions in the $(m_{\tilde{g}}, m_{\tilde{q}})$ plane excluded by CDF Run II (a) and regions excluded in the $(m_0, m_{1/2})$ plane by D0 Run II (b), the chosen values of A_0 , $\tan\beta$ and μ are denoted in the figures. Theoretical limits and search limits from earlier experiments are also shown.

The high center-of-mass energy at the $p\bar{p}$ collider LHC will allow to extend these current exclusions limits or to discover SUSY. In $p\bar{p}$ collisions, the most copiously produced SUSY particles are expected to be the colored ones corresponding to multi-jet event topologies. The present analysis studies the full-hadronic search channel based on large missing energy, multiple hard jets and no leptons. The particular properties of the studied search channel are exploited to develop a search method with high background suppression and SUSY signal efficiency, but also safety against systematic uncertainties.

Table 1.4: mSuGra parameter values and leading order cross-sections for the different parameter-sets studied in this analysis. Masses are given in units of GeV [16].

Point	m_0	$m_{1/2}$	$\tan\beta$	$\text{sign}(\mu)$	A_0	σ LO(pb)
LM0	200	160	10	+	-400	110
LM1	60	250	10	+	0	16.1
LM2	185	350	35	+	0	2.4
LM3	330	240	20	+	0	11.8
LM4	210	285	10	+	0	6.7
LM5	230	360	10	+	0	1.9

The mSuGra parameter-space can be divided into separate regions with similar event topologies, depending on the mass differences between the various gluinos and squarks. The studied parameter-sets are placed in different parameter-space regions thus covering a wide range of possible topologies. The sets are given in Table 1.4 and depicted as points in the $m_0 - m_{1/2}$ plane for fixed values of $\tan\beta$, A_0 and $\text{sign}(\mu)$ in Fig. 1.5. Some important mass relations are marked with green lines. The regions excluded by LEP data

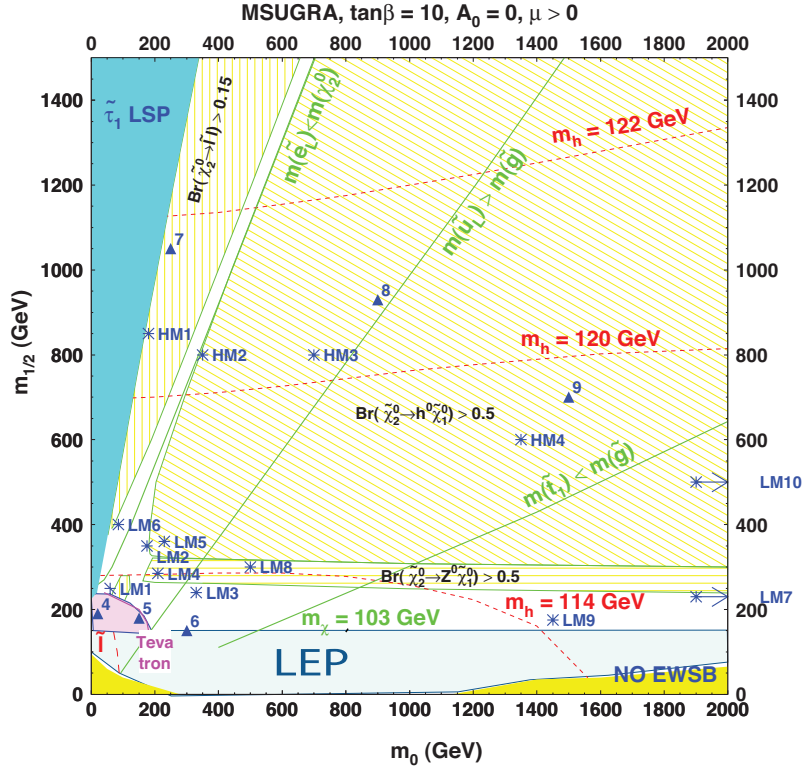


Figure 1.5: The $(m_0, m_{1/2})$ plane for fixed values of A_0 , $\tan\beta$ and μ , the positions of the studied parameter-sets are marked by stars (Ref. [16]). The regions shaded in yellow or turquoise are excluded theoretically, either because the $\tilde{\tau}_1$ would be the LSP or because there is no radiative electroweak symmetry breaking possible. The regions excluded by LEP and Tevatron experiments are shaded in bright blue and violet respectively. Also shown are the regions of interest for the decay of the $\tilde{\chi}_2^0$ (yellow dashed areas delineated by thin green lines.)

are indicated by an area shaded in light blue, the theoretically excluded regions are shaded in yellow and turquoise.

Even though the full-hadronic channel has a high sensitivity to SUSY signals, it is also a particularly challenging channel at a hadron collider. The main reasons are the overwhelmingly large cross-section of QCD multi-jet production and also the systematic uncertainties on the jet energy resolution of the detector. The following chapter concentrates therefore on the physics at hadron colliders and the design and performance of the CMS detector. A possible extension of the presented analysis could exploit the flavor of the produced jets, as extracted e.g. by b-tagging algorithms. The additional information about the b-jet multiplicity could be used to suppress background from light pair-produced quarks and to constrain the SUSY parameter-space in case of a discovery. A well performing and understood pixel detector is crucial for an effective b-tagging. A part of the next chapter is therefore dedicated to a comparison of cosmic ray data with simulation.

Chapter 2

LHC and the CMS Detector

The Compact Muon Solenoid (CMS) detector is one of the four large detectors at the Large Hadron Collider (LHC). LHC is situated at the European Organization for Nuclear Research (CERN) on the border between France and Switzerland. CERN was founded in 1954. It has hosted several large particle accelerators over time, first the 28 GeV Proton Synchrotron (PS), then the Super Proton Synchrotron (SPS), then the e^+e^- collider LEP (Large Electron-Positron collider), and currently the LHC. The LHC is the worlds most powerful particle accelerator.

2.1 Physics at Proton - Proton Colliders

The task of particle colliders, like the LHC, is to collide as many particles as possible with energies high enough to create new particles. The cross section σ of a physics process gives a measure for its probability. The event rate $\frac{dN}{dt}$ of a certain process is proportional to its cross section, the factor of proportionality is the luminosity \mathcal{L} .

$$\frac{dN}{dt} = \mathcal{L} \cdot \sigma \quad (2.1)$$

High energy particles, with enough energy for collisions, are accelerated in the electrical fields of several cavities. One advantage of ring accelerators, like the LHC, is that particles can be accelerated many times by the same cavities. The luminosity for the collision of two bunches containing n_1 and n_2 particles, depends on the frequency f with which these particles circulate inside the ring:

$$\mathcal{L} = f \frac{n_1 n_2}{4\pi\sigma_x\sigma_y}, \quad (2.2)$$

where a gaussian beam distribution has been assumed. The root-mean-square (r.m.s.) of this gaussian σ_x and σ_y are the transverse beam profiles in horizontal (x) and vertical (y) direction.

One advantage of the proton-proton collider LHC is the negligible energy loss ΔE by synchrotron radiation. This is due to the large radius r of the ring and the relatively high

proton mass m . The relation between the energy loss of a particle per orbit, its energy (E) and mass (m) and the radius (ρ) of the collider is:

$$\Delta E = 6.0 \cdot 10^{-21} \text{GeV} \cdot \left(\frac{E}{m}\right)^4 / \rho[\text{km}] \quad (2.3)$$

However, proton-proton colliders collide composite particles and only direct inelastic collisions of the partons lead to “interesting” processes, in which heavy particles are generated. Elastic collisions are not of interest for high energy particle physics analysis such as the one presented here and are therefore regarded as detector pollution.

The parton energy E_{parton} is only a fraction x of the proton energy E :

$$x = \frac{E_{parton}}{E} \quad (2.4)$$

In inelastic collisions the centre-of-mass energy of colliding partons s' can be calculated as:

$$\sqrt{s'} = \sqrt{x_a x_b s}, \quad (2.5)$$

where x_a and x_b are the energy fractions carried by the interacting partons and $\sqrt{s} = 2E$. Typically every inelastic collision is accompanied by several elastic collisions. To distinguish between the particles created in inelastic and elastic collisions the concept of the underlying event has been introduced. The underlying event in a hadron-hadron interaction consists of all particles from a single proton-proton collision except those from the process of interest.

The cross section σ for an elementary process at proton-proton colliders depends on the density f_i of the partons inside the proton.

$$\sigma = \int dx_1 \int dx_2 f_1(x_1, Q^2) f_2(x_2, Q^2) \hat{\sigma}, \quad (2.6)$$

where the partonic cross-section $\hat{\sigma}$ can be calculated for the different processes. The function $f_i(x_i, Q^2)$ is called parton density function (pdf). The parton density function can be regarded as the probability that parton i takes part in a hard scattering process with the total momentum transfer Q^2 and carries the momentum fraction x_i . The parton density functions used at the LHC are determined amongst others by experiments at the hadron-electron collider HERA [18, 19]. Their knowledge is crucial for physics at the LHC. The partonic density functions for the partons (quarks and gluons) in the proton are shown in Fig. 2.1. The protons consists of three valence quarks two up quarks and one down quark, gluons and several additional pairs of quarks and corresponding anti-quarks (sea-quarks).

With the high luminosity and centre-of-mass energy expected at the LHC, a range of processes with widely different cross-sections can be covered. Fig. 2.2 shows the cross-sections and event rates, at a luminosity of $\mathcal{L} = 10^{34} \text{ cm}^{-2} \text{ s}^{-1}$, for various processes as a function of the center-of-mass energy. The design energy at the LHC $\sqrt{s} = 14 \text{ TeV}$ is marked in this figure by the vertical dashed line. Drastic selection requirements have to be used to filter rare events, like the one studied in this thesis, from the large number of produced events. The detection of signatures corresponding to interesting events is further complicated by signals stemming from particles of previous bunch crossings which still linger inside the detector. These signals are commonly called pile-up events.

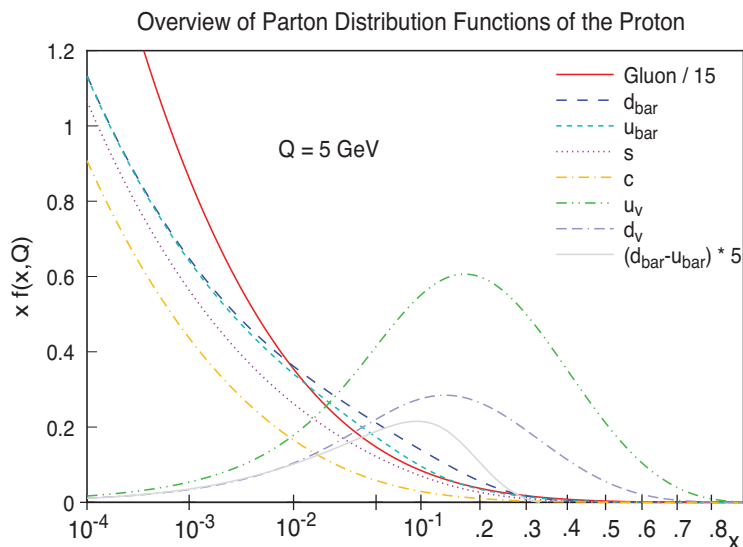


Figure 2.1: Parametrization of parton distribution functions inside the proton [20].

2.2 LHC Design

The LHC [1] is a ring accelerator buried 50 m to 175 m below surface, with a circumference of 27 km. Two beams of protons (or heavy ions) counter rotate in continuous vacuum inside the LHC. The two beams circle in two different rings with separate superconducting magnet dipole and quadrupole fields. The LHC has 1232 dipole magnets with a design operating magnetic field of 8.4 T at 14 TeV. To reach this magnetic field the magnets are cooled with superfluid helium to a temperature of 1.9 K. Proton-proton collisions take place at the four interaction points. The first collisions at the LHC have been observed 2009 with 0.9 and 2.36 TeV. In 2010 the collision energy of the LHC has been ramped up to 7 TeV. In the future collision energies of 10 – 14 TeV will be achieved. The plan is to run the LHC in 2010 and 2011 at 7 TeV until an integrated luminosity of 1 fb^{-1} is reached.

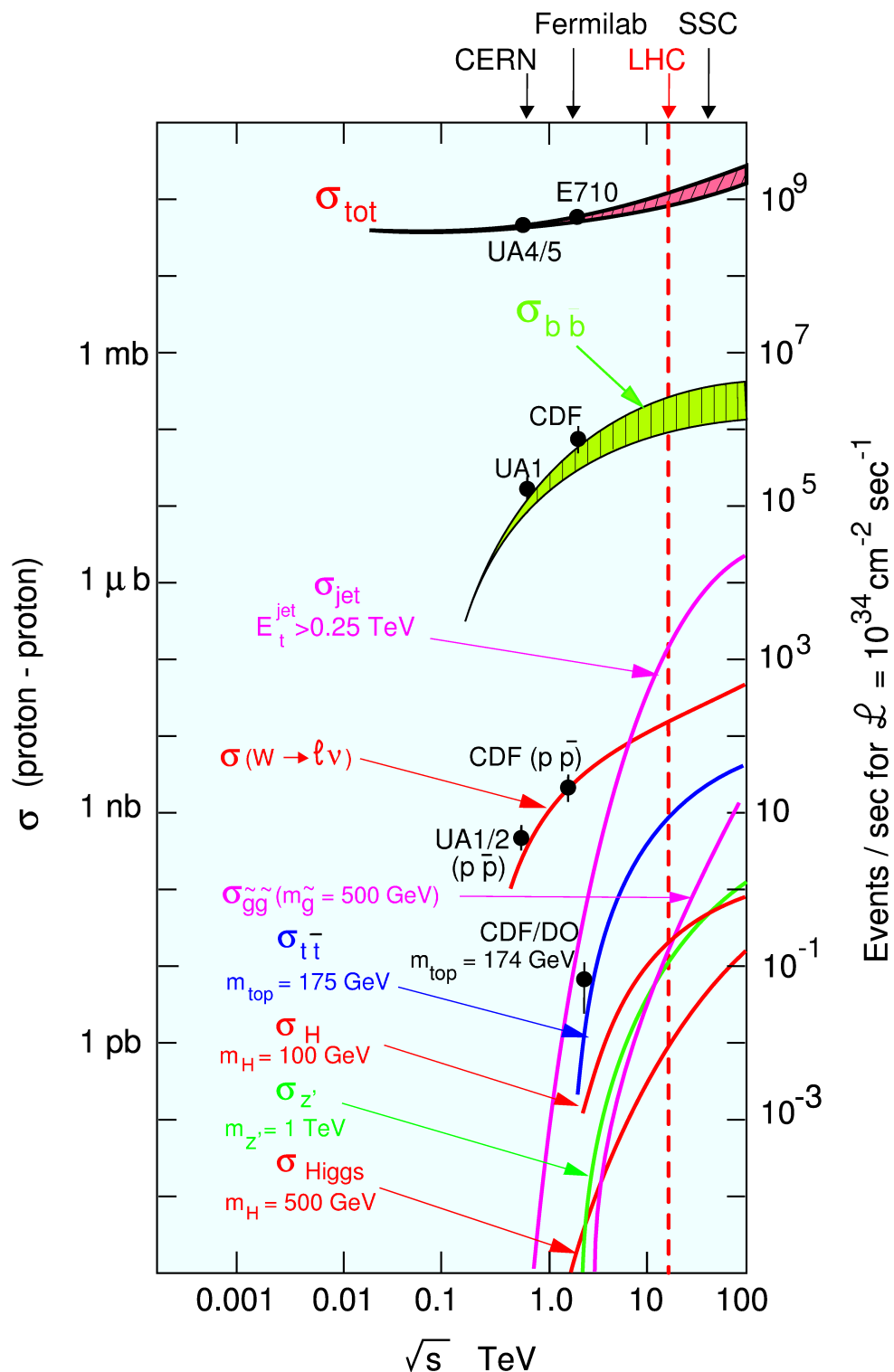


Figure 2.2: Cross sections and event rates of various processes as a function of center-of-mass energy at proton-proton colliders [21].

2.3 CMS Detector

The CMS detector (Fig. 2.3) [2, 22] is a multi-purpose detector. It detects particles generated in collisions and determines their properties. The name of the detector, Compact Muon Solenoid, phrases its basic properties: a compact design, an emphasis placed on a highly efficient muon detection and measurement, and the fact that the detector is built around a single superconducting solenoid.

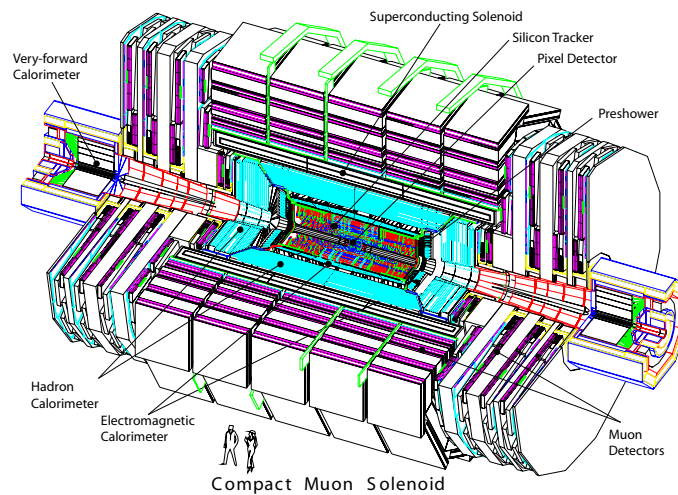


Figure 2.3: The CMS detector [22].

The compactness of the CMS design can be estimated by a comparison to the other multi-purpose detector at the LHC, ATLAS. The CMS detector weighs 12 500 tons, which is twice the weight of ATLAS, but with its length of 21 m and its diameter of 15 m it is eight times smaller than ATLAS.

The highly efficient muon system of CMS is crucial for discovering new physics, as muons provide clean signatures for a wide range of physics. The muon system measures the muon momentum precisely and provides fast information to decide if an event is "interesting" or not.

To measure the charge and momentum of charged particles, particle detectors need a magnetic field [22] which bends their tracks according to their momentum. The magnet used in the CMS detector is a superconducting solenoid with a field of 4 T. Its length is 13 m and its inner diameter is 5.9 m. The magnet is kept superconducting with liquid helium. The magnet stores an energy of 2.7 GJ. The magnetic induction is about 4 T in

the coil and in the innermost section of the endcap yoke, and about 1.7 T in the barrel part of the return yoke and in the outermost disk of the endcap yoke.

The detector is built in an onion-like structure surrounding the interaction point (Fig. 2.3) with the intention to discriminate between particles with different energy losses and different ranges in material. Electrons and photons shower mainly in the Electromagnetic Calorimeter, where their energy can be measured precisely. Hadrons which interact via the strong interaction deposit most of their energy in the Hadronic Calorimeter. Muons are the only charged particles which traverse the iron return yoke plates and reach the Muon System.

The cartesian coordinate system (x, y, z) of the CMS detector is right-handed, the nominal interaction point is the origin and the x -axis is pointing towards the center of the LHC ring. The polar coordinates are defined by:

$$\phi = \arctan\left(\frac{y}{x}\right), \quad (2.7)$$

$$\theta = \arccos\left(\frac{z}{\sqrt{x^2 + y^2}}\right). \quad (2.8)$$

The pseudorapidity η is often used instead of the angle θ . It is defined as:

$$\eta = -\ln\left[\tan\left(\frac{\theta}{2}\right)\right] \quad (2.9)$$

The different detector parts are described in the following sections.

2.3.1 Muon System

Three types of gaseous detectors are used in the muon system [23] (Fig. 2.4), Drift Tubes (DT), Cathode Strip Chambers (CSC) and Resistive Plate Chambers (RPC). These gaseous detectors are chosen to fit the requirements in the different environments of barrel and endcap. Drift Tubes (DT) are the ideal detectors for the large area of the barrel ($|\eta| < 1.2$) with its relatively low rate and low residual magnetic field (less than 1 T). They are designed to provide an excellent spatial resolution. CSCs provide a relatively precise spatial and time resolution even in the high magnetic field and high particle rate environment of the endcap region ($|\eta| < 2.4$). DTs and CSCs are supplemented in barrel and endcap by Resistive Plate Chambers (RPC), which have worse spatial resolution, but a much better time resolution.

2.3.2 Hadron Calorimeter

The main task of the hadron calorimeter is to stop strongly interacting particles and to measure their energies. When the transverse component of the energies is measured precisely, the missing transverse energy can be calculated. Thus non-interacting particles such as

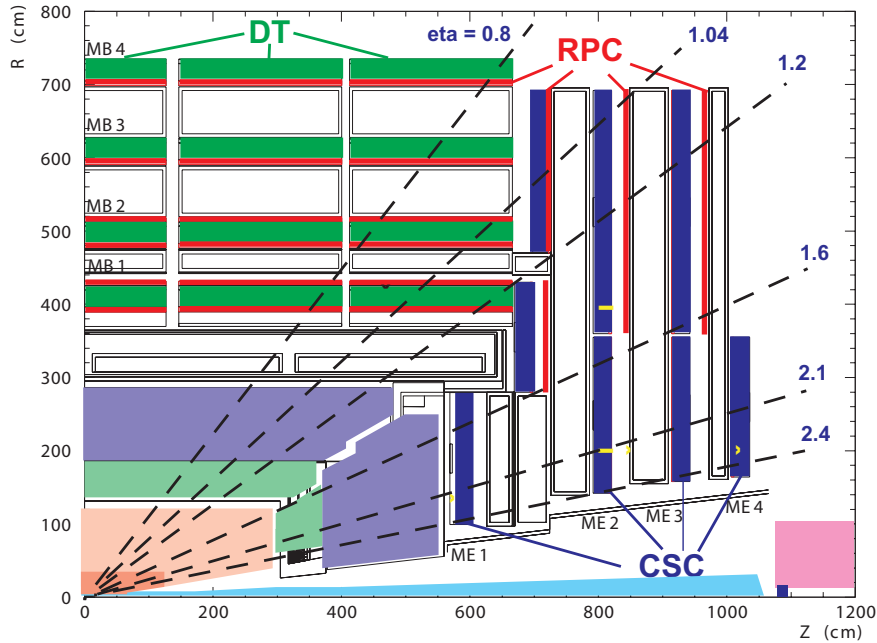


Figure 2.4: Longitudinal cut of the CMS Muon System, the dashed lines indicate different pseudo-rapidities $|\eta|$ [22].

neutrinos or supersymmetric lightest stable particles (LSP) can be seen indirectly. Therefore, the hadron calorimeter is built of absorber material with short interaction lengths (e.g. brass) and provides an almost full angular coverage $|\eta| < 5$.

The calorimeter is divided into four parts. Three parts lie inside the magnet coil, the barrel hadron calorimeter (HB), which covers the region $|\eta| < 1.3$, two endcap hadron calorimeters (HE), which cover $|\eta| < 3$, and the forward calorimeter (HF) covering $3.0 < |\eta| < 5.0$. The outer calorimeter (HO) is located outside of the magnet to improve the shower containment. Fig. 2.5 shows the η coverage of HB, HE, the barrel electromagnetic calorimeter (EB) and the endcap electromagnetic calorimeters (EE).

Barrel Hadron Calorimeter and Endcap Hadron Calorimeter:

The absorber material used inside the barrel and the endcap is brass, which has a reasonably short interaction length ($\lambda_I(\text{Cu}) = 15.06$ cm). Plastic scintillator tiles are the active medium which detects energy deposited inside the barrel and the endcap. The readout is done by wavelength shifting plastic fibers.

The Barrel Calorimeter is divided into two half barrels, which are structured into eighteen 20° wedges in ϕ [25]. Each wedge consists of alternating 17 layers of 50 mm thick brass plates and 4 mm thick readout scintillators. The total absorber thickness at 90° is 5.82 interaction lengths (λ_I), the effective thickness increases as $1/\sin\theta$ up to $10.6\lambda_I$ at $|\eta| = 1.3$.

The endcap hadronic calorimeters consists of eighteen 20° modules. These modules are made of 19 layers of brass and scintillator. The total length of the calorimeter including electromagnetic crystals, is about 10 interaction lengths (λ_I). The granularity of the

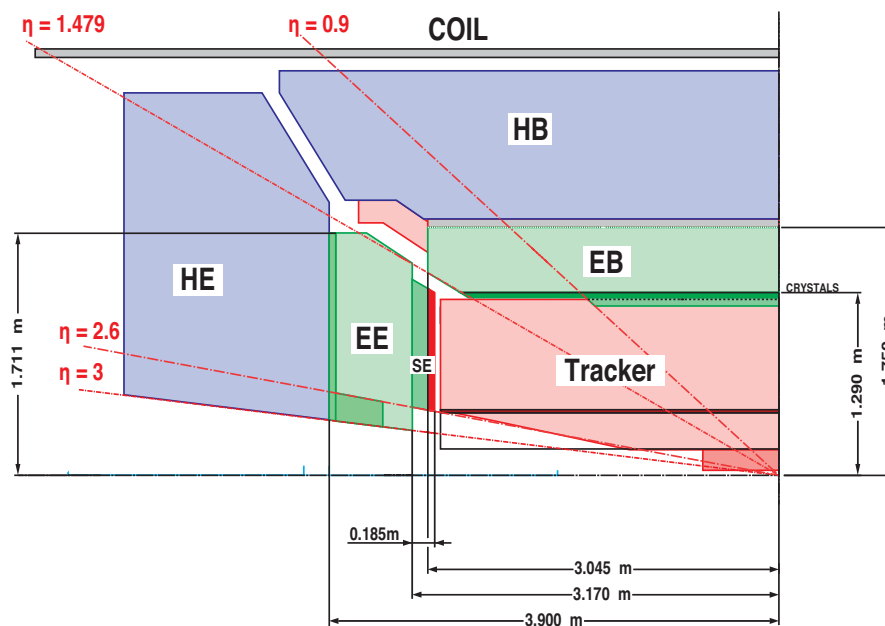


Figure 2.5: Schematic view of one quadrant of the CMS calorimetry and tracking system. The forward calorimeter HF covering $3.0 < |\eta| < 5.0$ is not shown [24].

calorimeters is $\Delta\eta \times \Delta\phi = 0.087 \times 0.087$ for $|\eta| < 1.6$ and $\Delta\eta \times \Delta\phi = 0.17 \times 0.17$ for $|\eta| \geq 1.6$.

Forward Hadronic Calorimeters:

The forward hadronic calorimeter improves the measurement of the missing transverse energy and enables the identification and reconstruction of very forward jets. The forward calorimeters are located 11.2 m from the interaction point and have a length of 1.65 m and a radius of 1.4 m. Each forward calorimeter is constructed of 18 wedges. The wedges are made of steel absorbers and embedded radiation hard quartz fibers running parallel to the beam axis. These fibers provide a fast collection of Cherenkov light [26].

Outer Hadronic Calorimeter:

The outer calorimeter absorbs the strong interacting particles which reach the region beyond the magnet. This calorimeter increases the effective thickness of the hadron calorimeter to over 10 interaction lengths. The outer calorimeter consists of two layers of scintillators on either side of an iron absorber. The outer calorimeter is located outside the solenoid but inside the barrel muon system. It is divided into five rings.

2.3.3 Electromagnetic Calorimeter

In the Electromagnetic Calorimeter (ECAL) [27] scintillating crystals absorb the radiation deposited by electromagnetically interacting particles, photons and the electromagnetic component of jets. To measure the energy of electromagnetically charged particles as precisely as possible the particles have to be stopped inside the Electromagnetic Calorimeter. To keep the Electromagnetic Calorimeter small the scintillating crystals in the CMS detec-

tor consist of lead tungstate (PbWO_4), which has a short radiation length ($X_0 = 0.89$ cm). The scintillating crystals are fast (80% of the light is emitted within 25 ns) and radiation hard (up to 10 MRad) which is important in the high radiation environment inside the CMS detector.

The photodetectors which detect the light emitted by the crystals are silicon avalanche photodiodes (APDs) in the barrel and vacuum phototriodes (VPTs) in the endcap. These photodiodes and phototriodes have a high intrinsic gain which amplifies the low light yield ($30\gamma/\text{MeV}$) of the scintillators.

The electromagnetic calorimeter is divided into a barrel section (EB) and endcaps (EE) (Fig. 2.5). The barrel has a length of ~ 6 m, an inner radius of 1.3 m and an outer radius of 1.8 m. It covers a pseudo-rapidity range up to 1.48. The front face of the crystals points towards the interaction region. The endcaps are located at $|z| = 314$ cm. The volume of the barrel crystals is $22 \times 22 \times 230$ mm³.

A preshower device in front of the endcaps consists of a lead absorber, which covers a range from $1.65 < |\eta| < 2.61$, and 2 planes of silicon strip detectors for readout, with a pitch of 1.9 mm. This device improves neutral pion and photon separation. The lead absorber initiates photon showers.

2.3.4 Inner Tracking System

The inner tracking system [2, 28] is the innermost part of the detector and is built close to the beam pipe. Its purpose is to measure particle trajectories with high precision to obtain good momentum resolution. The tracker reconstructs muons, isolated electrons and hadrons tracks with an efficiency of better than 98%. It has a high spatial resolution to identify tracks coming from detached vertices and is robust enough to sustain the strong radiation environment. Furthermore it is built as thin (small number of radiation lengths) as possible to prevent e.g. electrons from radiating before they reach the electromagnetic calorimeter.

The inner tracking system is based on silicon detector technology and is divided into two parts:

- The silicon microstrip detectors in the region of intermediate particle fluxes ($r > 20$ cm).
- The silicon pixel detectors, closest to the interaction vertex (at a radius $r > 4$ cm). This is the region of high particle fluxes, $\approx 2\text{MHz}/\text{mm}^2$ at a radius of $r \approx 4$ cm, falling to $60\text{kHz}/\text{mm}^2$.

Both detectors are semiconductor detectors. The readout of all tracker sub-detectors is analog using the information of the charge deposited on each strip or pixel. The charge-sharing among neighbouring pixels or strips in the barrel is mainly due to Lorentz drift in the 4 T magnetic field. However, in the forward detector the main source of charge-sharing is the average impact angle of 20° with respect to normal incidence. Analog pulse-height

readout improves the resolution compared to a digital readout, for which the resolution of the detector is determined by the pixel or strip size.

Silicon Strip Detector Fig. 2.6 shows the design of the silicon strip detector. It can be

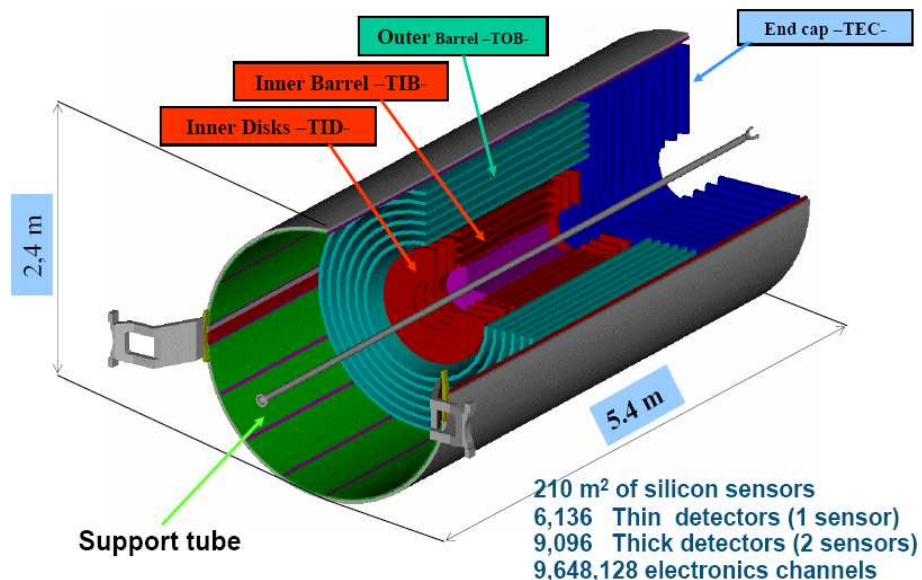


Figure 2.6: The CMS Silicon Strip detector, consisting of TID, TIB, TOB, TEC. The Silicon Pixel detector is indicated as pink tube in the center [28].

divided into four parts: Tracker Inner Barrel (TIB), Tracker Outer Barrel (TOB), Tracker Inner Disks (TID) and Tracker End Cap (TEC). Together, these parts cover a cylindrical volume with a length of 5.4 m, an inner radius of 0.2 m and an outer radius of 1.2 m.

Inner and outer barrel have a different design to accommodate the requirements given by the corresponding particle flux environments. The particle flux depends on the distance to the beam pipe. The TIB is close to the beam, its granularity has to be high to separate between neighbouring tracks. To achieve this resolution the distances between the single strips are very small (strip pitch $80\ \mu\text{m}$ to $120\ \mu\text{m}$) and the thickness of the sensors is $320\ \mu\text{m}$. A second micro-strip detector module is mounted back-to-back with a stereo angle of $100\ \text{mrad}$ with respect to the modules in the first two layers and rings, respectively of TIB, TID, and TOB, as well as rings 1, 2 and 5 of the TECs. With this second detector module the single point resolution is $230\ \mu\text{m}$ in z and $23 - 34\ \mu\text{m}$ in the $r - \phi$ direction in the TIB. For the larger pitches, the analog readout does not significantly improve the resolution, as most of the charge is deposited on a single strip. The occupancy in the TIB is $\sim 2 - 3\%$ per strip and LHC bunch crossing.

The TOB works in an environment with lower particle fluxes where the single point resolution can be reduced to keep under control the overall cost of the tracker. Wider pitches between the strips ($120\ \mu\text{m}$ to $180\ \mu\text{m}$), longer strips and thicker silicon sensors ($500\ \mu\text{m}$) are used in the outer barrel. The single point resolution of the Outer Barrel is $35\ \mu\text{m}$ in the $r - \phi$ directions and $530\ \mu\text{m}$ in z . The occupancy in the outer barrel is $\approx 1\%$ /LHC crossing.

The full silicon strip detector covers the region $|\eta| < 2.5$. The operating temperature is around -20°C to ensure that the silicon survives the high radiation environment.

Silicon Pixel Detector: The main tasks of the pixel detector are the reconstruction of primary and secondary vertices from b - and τ - decays, and the formation of seeds for track reconstruction and high level triggering.

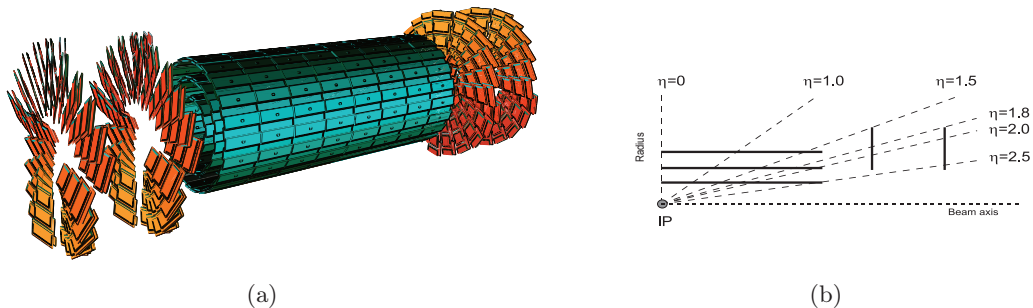


Figure 2.7: Sketch of the CMS pixel detector [29] (a) and its pseudorapidity coverage [2] (b).

The pixel detector, presented in Fig. 2.7(a), consists of three 53 cm long barrel layers at mean radii of 4.4, 7.3 and 10.2 cm and two endcap disks at each side of the barrel with an inner radius of 6 cm and an outer radius of 15 cm. The disks are placed at $|z| = 34.5$ cm and 46.5 cm. This arrangement of the barrel layers and endcap discs gives three tracking points over almost the full range of $-2.5 < \eta < 2.5$ as visible in Fig. 2.7(b). The sensitive area of the pixel detector is $\approx 1\text{m}^2$ for a total of 66 million pixels. The size of the pixel cell surface of $100 \times 150 \mu\text{m}^2$ has been chosen to achieve similar track resolution in both $r - \phi$ and z directions and to allow a 3D vertex reconstruction. The minimal pixel cell size is dictated by the readout circuit area required for each pixel. The necessity of a high radiation tolerance has led to the choice of the so called n -on- n concept. The pixel consists of high dose n -implants on a high resistance n -substrate. The sensors are bump-bonded to highly integrated readout chips (ROC). Each ROC is connected to 52×80 pixels.

In contrast to the strip detector the deposited charge in the pixel detector is often shared among several pixels. Using an analogue charge readout a spatial resolution of $15 - 20 \mu\text{m}$ is achieved. Each pixel sensor has an adjustable threshold and only signals above this threshold are accepted by the ROC. They are then marked with a time-stamp derived from the 40 MHz LHC bunch crossing clock, and stored for readout. In the ROC the signals from individual pixels are amplified and shaped. The analogue optical signals generated by the ROCs are received in the underground service cavern by 8-bit Front End Driver boards (FED). Each of the 40 pixel FED has analog optical receivers, flash ADCs (Analog-to-Digital Converters) and FPGAs (Field Programmable Gate Arrays) to decode the analogue signal into pixel addresses and digitized charge information.

In 2008 the mean readout thresholds were set to 3829 and 2941 electrons, with an r.m.s. of 417 and 236 electrons for the barrel and endcap, respectively [29]. The readout thresholds were lowered in 2009 to 2733 ± 196 electrons in the barrel detector and 2483 ± 163 electrons in the forward detectors. In addition to the readout threshold an in-time threshold is defined which requires the time-stamp of the recorded signal to match the trigger bunch crossing.

Due to the finite rise time of the shaped signal in the ROC the in-time threshold is in general higher than the absolute readout threshold. Small signals cross the absolute threshold later than large signals and can be time-stamped in the subsequent bunch crossing, this is called *time walk effect* [30]. The in-time thresholds for cosmic ray muons are even higher than those for collisions due to their random arrival in time [29].

Pixel clusters are formed from adjacent pixels with charge above the readout threshold. Both side and corner adjacent pixels are included in the cluster. The cluster charge is defined as the sum of the charges deposited in the corresponding pixels. The cluster position is interpolated using the charge information from all pixels in the cluster [31]. A sufficiently accurate conversion from the digitized signal to the charge in electrons is necessary for a precise reconstruction of the hit position.

This ADC to electron conversion is basically divided into two steps. First, the pixel response is calibrated by injecting a controlled amount of charge on each ROC and measuring the the pixel pulse height response in ADC units. The injected charge is controlled by a DAC (Digital-to-Analog Converter) and therefore measured in VCAL units. Secondly, a conversion from VCAL units into electrons is performed. The relation between the charge in electrons Q and in VCAL units is given by:

$$Q = x \cdot VCAL + y, \quad (2.10)$$

The values of x and y are obtained using one barrel pixel module and x-ray sources of known energy [32]:

$$x = 65.5 \pm 8.9 \quad , \quad y = -414 \pm 574 \quad (2.11)$$

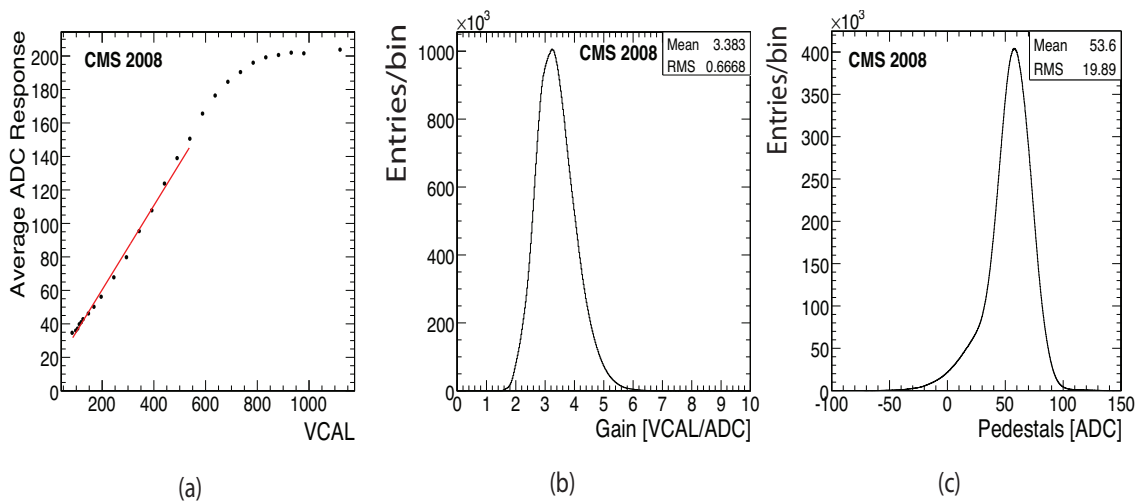


Figure 2.8: a) ADC response in 2008 data as a function of injected charge in VCAL units. b)-c) Distributions of gains and pedestals for all pixels [29].

The first calibration step of this conversion was repeated during data taking in 2008 and 2009. The ADC response as a function of the injected charge in VCAL units is shown in Fig. 2.8 (a). The response is approximately linear below saturation at about 45 000

electrons and the conversion factor is taken from a linear fit to this region. The inverse of the slope and the intercept from the fit are the gain and pedestal parameters. The pedestal and gain are determined for each pixel and are depicted in Fig. 2.8 (b-c).

2.4 Comparison of Cosmic Ray Data with Simulation

In October-November 2008, the CMS pixel detector took its first data with a magnetic field of 3.8 T (Cosmic Run At Four Tesla, CRAFT) [29]. The goal of these data taking exercises was to commission the CMS detector before the start of collisions. Of the 270 million cosmic-ray-triggered events, approximately 85 000 tracks traversed the pixel detector volume and about 257 000 clusters were reconstructed. In the year 2009 a second CRAFT exercise was performed and the very first collision data analyzed. The lessons learnt from CRAFT 2008 have helped to significantly improve the performance of the pixel detector and its simulation.

In this section the pixel cluster charge measured with data from cosmic muons in CRAFT 2008 is compared to simulation. The GEANT4 package [22, 33], which describes the distribution of deposited energy, is used for the simulation of the detector response. The drift of charge from each track subsegment and the mapping of the resulting 2-dimensional charge distribution to the pixel geometry is performed by the CMS software [22]. A noise contribution which follows a Gaussian distribution centered at zero is added to all hit channels. The resulting output is the deposited charge per pixel in electrons. However, to compare data and simulation the detector response is needed in ADC counts.

The following chain of calculation is used for the conversion:

$$VCAL = [Q - y]/x \quad (2.12)$$

$$Q(ADC) = p_3 + p_2 \cdot \tanh(p_0 \cdot VCAL - p_1), \quad (2.13)$$

where the charge Q in Eq. 2.12 is in electrons and p_0 , p_1 , p_2 and p_3 are fitting parameters. The uncertainty on the measured x and y is taken into account by spreading their values according to the measured r.m.s..

The ADC digitization is simulated by rounding the resulting charge value to the nearest integer. Signals exceeding the ADC range (8 bits) are assigned the maximum allowed ADC value. The simulated threshold has been set to 5200 electrons in the barrel and to 4500 electrons in the endcap. A smearing of 200 electrons in the barrel and 410 electrons in the endcap pixel detector has been applied. The thresholds are chosen to match the effective threshold in 2008. The effective threshold is higher than the absolute threshold due to the *time walk effect*. The simulated and the measured detector response are passed to the same reconstruction mechanism. The used track algorithm is the Combinatorial Track Finder (CTF) [34].

The cluster charge depends on the impact angle of the incoming tracks. The more shallow the angle between the track and the pixel module, the longer is the path of the track in the sensor and the more charge is deposited. The angular distribution of reconstructed

tracks has been compared to the prediction and found to be in good agreement [34]. To study the cluster charge independently of the impact angle the charge is normalized to that of a perpendicular track. The relation between the normalized charge $Q_{norm.}$ (or simply "cluster charge") and the total charge Q is:

$$Q_{norm.} = Q \frac{s_t}{s}, \quad (2.14)$$

where s is the length of the path of the track in the pixel module, as calculated from the impact angles, and s_t is the thickness ($285 \mu\text{m}$) of the pixel detector.

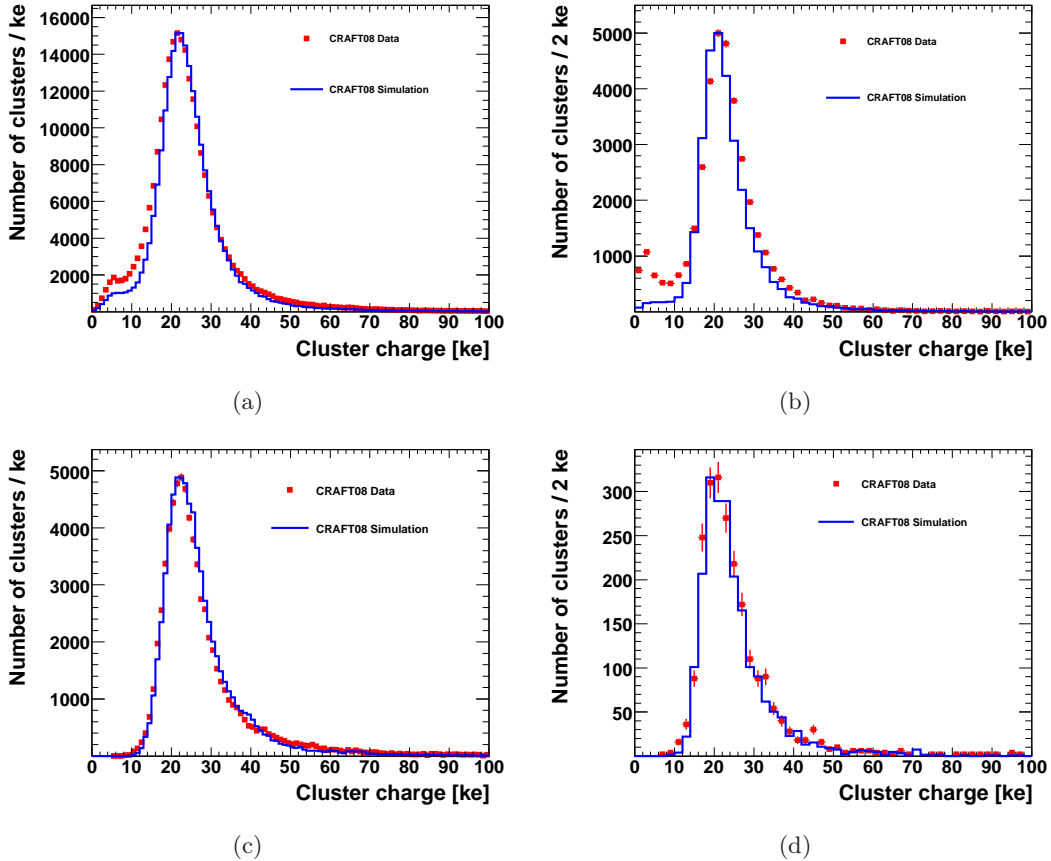


Figure 2.9: Distribution of the normalized cluster charge in 10^3 electrons (ke) measured with the barrel (left-hand side) and endcap (right-hand side) pixel detector after the cut on clusters on the edge of modules (upper row) and after all selection cuts (lower row). The data points show the measurement with cosmic ray muons and the solid line the simulation. The simulated distributions are scaled up so that the number of clusters at the peak position is the same for data and simulation.

To suppress detector noise only clusters associated to a track with a momentum larger than $4 \text{ GeV}/c$ are accepted. In addition, clusters are rejected if located at the edge of modules, as in this case part of the deposited charge might be lost. The charge distribution in data is broader than in simulation and a peak around $5\,000 \text{ e}$ is observed (Fig. 2.9). This peak is more pronounced in the endcap than in the barrel detector. Two main reasons have been identified for the low-charge peak.

High and varying readout thresholds: In a long cluster the charge deposited in some of the pixels might be below the pixel readout threshold, as this threshold varies from pixel to pixel. If the pixel is in the middle of a cluster the cluster is split into two parts. The charge deposited in one of the two fragments is lower than what is expected from the track impact angle. This effect is predicted by the simulation. In 2008 it was quite prominent as the readout thresholds were relatively high and had a large variation from pixel to pixel. The fractional contribution of low charge clusters from high and varying readout thresholds should be equal in data and in simulation, provided that the simulation uses the correct values of the effective thresholds, their r.m.s. and the variation of the pixel charge in electrons.

The *time walk effect* together with random arrival of cosmic ray muons: When a cosmic muon is detected by the CMS trigger system, signals in the associated clock cycle are read out. Signals in the previous and in the following clock cycles are lost. For a muon which hits the pixel detector at the end of the associated clock cycle, only the large amplitude signals might cross the readout threshold in time. In contrast, large amplitude signals might be lost if the muon hits the pixel detector before the associated clock cycle. In this case only signals with a small amplitude cross the readout threshold late enough to be in the right clock cycle. The signal of pixel hits in a long cluster are in general of different amplitude, some of these hits might therefore be lost due to the described effect. The cluster would be split. The charge deposited in one fragment of this clusters would again be lower than what is expected from the track impact angle. This effect is not described by the simulation. In the simulation, the signals which are read out in the pixel detector cannot originate from an earlier bunch crossing.

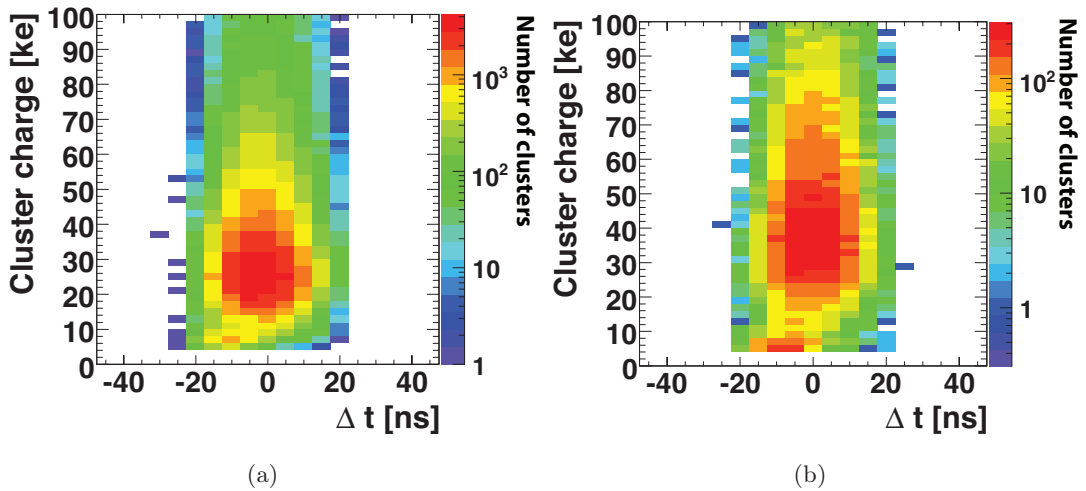


Figure 2.10: Distribution of the normalized cluster charge in 10^3 electrons (ke) vs. Δt as measured in 2008 with data from cosmic ray muons, for the barrel (a) and for the endcap (b) pixel detector.

To test the second hypothesis, the arrival time of cosmic muons relative to the middle of the clock cycle Δt (determined by using the CMS muon system [35–37]) was studied. Fig. 2.10 shows the deposited cluster charge $Q_{norm.}$ as a function of Δt for the barrel and

endcap pixel detectors. Whereas the main peak at 25 ke is centered around $\Delta t = 0$, the low cluster charge peak is shifted towards negative Δt values. A large fraction of the clusters contributing to the low charge peak are associated to cosmic ray muons with early arrival times with respect to the associated clock cycle. It was found that most of these clusters are single pixel clusters (Fig. 2.11) and are associated to tracks with a shallow impact angle, as is visible in Fig. 2.12 for the α angle in the barrel¹. These two observations indicate that the low charge clusters are indeed the remnants of long clusters.

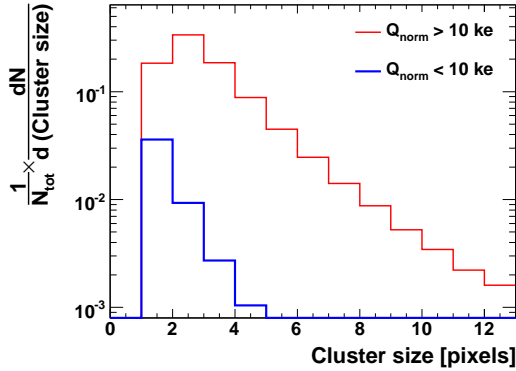


Figure 2.11: Distribution of the cluster size for clusters with $Q_{norm} < 10\text{ke}$ (blue line) and for clusters with $Q_{norm} > 10\text{ke}$ (red line) for data taken from cosmic ray muon showers in the year 2008. The total number of clusters N_{tot} associated to tracks with $p > 4 \text{ GeV}/c$ is normalized to unity.

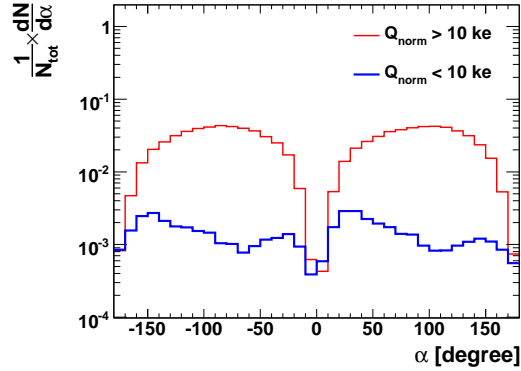


Figure 2.12: Distribution of the angle α for clusters with $Q_{norm} < 10\text{ke}$ (blue line) and for clusters with $Q_{norm} > 10\text{ke}$ (red line) for data taken from cosmic ray muon showers in the year 2008. The total number of clusters, N_{tot} , associated to tracks with $p > 4 \text{ GeV}/c$ is normalized to unity.

The two described effects are hard to distinguish, as the error on Δt is large ($\approx 5\text{ns}$) [36, 37]. To diminish the contribution of both effects further selection cuts are applied.

The relative contribution of the low charge clusters is largest for single pixel clusters (Fig. 2.11). This observation is consistent with the assumption that low charge clusters are the remnants of larger clusters, due to one of the two described effects. To reject this remnants, clusters are required to include at least two pixels. Hits are also excluded if more than one cluster is found within the same module or plaquette. Finally, to emulate the angle distribution expected for collisions, tracks with a transverse impact angle larger than 12° from the normal to the sensor surface are excluded from the study.

The number of remaining clusters after each selection step is presented in Table 2.1. Both the cluster size cut and the cut against clusters on the same modules remove a significant fraction of the low charge peak while keeping $\sim 80\%$ and $\sim 70\%$ of the clusters with $Q_{norm} > 10 \text{ ke}$ for the barrel and endcap pixel detectors respectively. The angle requirement removes most of the pixel hits, which is expected as the angle distribution in collisions is different from that in cosmic showers. Hits in the endcap detectors are more

¹Information about the local coordinate system of the pixel detector and the definition of the angles α and β can be found in Appendix A.1.2.

affected by this requirement as cosmic muons arrive at a very shallow impact angle while tracks from collision should be almost perpendicular.

Table 2.1: Number of remaining clusters after each selection step in the pixel barrel detector and in the pixel endcap detector for data taken from cosmic ray muon showers in 2008. The efficiency of each selection cut with respect to the number of clusters selected by the track momentum cut is given in parenthesis.

selection	detector	$Q_{norm} < 10 \text{ ke}$	$Q_{norm} > 10 \text{ ke}$
no selection	barrel	16 443	269 242
	endcap	5 092	38 819
track $p > 4 \text{ GeV}/c$	barrel	14 924 (91%)	242 622 (90%)
	endcap	4 633 (92%)	35 411 (94%)
clusters not on module edge	barrel	13 076 (80%)	234 778 (87%)
	endcap	3 485 (68%)	32 995 (85%)
cluster size > 1 pixel	barrel	3 718 (23%)	186 971 (69%)
	endcap	1 740 (34%)	32 027 (83%)
no neighboring clusters	barrel	1 301 (8%)	175 050 (65%)
	endcap	827 (16%)	29 709 (77%)
angle constraint	barrel	37 (0.2%)	35 162 (13%)
	endcap	6 (0.1%)	1 126 (3%)

In Fig. 2.9 the simulated charge has been shifted by the observed difference in peak positions. The shapes of both distributions agree reasonably well after the selection.

To derive the most probable cluster charge and the width of the cluster charge distribution, fits to a Vavilov function are performed. The Vavilov function can be used to describe the energy deposition in thicker absorbers. The fit results are summarized in Table 2.2. In addition to the cluster charge and most probable value, the width, the χ^2/ndof of the fit and the parameter κ are stated in Table 2.2. For very small κ values ($\kappa < 0.01$) the Vavilov function converges to a Landau function, while for large κ values ($\kappa > 10$) the function converges to a Gaussian. The width of the charge distribution agrees well with the simulation. The simulated charge peak is shifted by 1 300 and 1 000 electrons in the barrel and endcap respectively. The discrepancy is attributed to the uncertainty on the scale factors applied to the data when converting the injected charge units into electrons.

Table 2.2: Most probable value (MPV), width, κ and χ^2/ndof of the Vavilov function fitted to the measured and simulated cluster charge. Errors represent the uncertainties on the fit.

	data (10^3 electrons)				simulation (10^3 electrons)			
	MPV	width	κ	χ^2/ndof	MPV	width	κ	χ^2/ndof
Barrel	23.9±0.2	3.7±0.1	0.18±0.02	1.6	22.6±0.2	3.4±0.1	0.13±0.02	1.6
Endcap	21.5±1.0	3.3±0.8	0.1±0.1	0.9	20.5±0.4	2.7±0.3	0.06±0.05	0.7

The presented comparison of data and simulation has helped to gain valuable insight into the performance of the CMS pixel detector and the simulation. Differences between the two have been understood. Subsequent studies performed in 2009 and 2010 have profited from this very first comparison and both reconstruction software and simulation have been improved successively.

Chapter 3

From Event Generation to Reconstruction

In order to span the gap between intricate theoretical models and the actual expected output of a detector various tools have been developed. Together these tools help to understand the detector response expected for particles produced according to a given theoretical model.

- Event Generation:

Monte Carlo event generators like PYTHIA [38], MADGRAPH/MADEVENT [39], ALPGEN [40] and HERWIG [41] take theoretical models as input and simulate the generation of events, i.e. sets of outgoing particles produced in the interaction between two incoming particles. A detailed description of the techniques employed to simulate the generation of events is given in Sect. 3.1.

- Detector Simulation:

The event generator output is taken and the interaction of the produced particles with the detector is simulated. In combination with GEANT4 (Geometry and Tracking) [33], the whole detector including magnetic fields, material distribution and properties are simulated. The energy loss and scattering of particles and their decay products along with their path through the detector is calculated.

- Digitization:

The output from the previous step is taken and the response of the readout electronics due to the interaction of generated particles with the detector is simulated.

- Object Reconstruction:

High-level objects, such as particle tracks, jets, vertices and their parameters get reconstructed. This part of the reconstruction is the same for real and simulated events. Different reconstruction mechanisms optimized for special tasks, for example the reconstruction of jets with different jet reconstruction algorithms can be chosen at this stage. The reconstruction of objects relevant for this analysis is presented in detail in Sect. 3.2. The information about several trigger levels is also accessible at this stage, and can be used to select events which are interesting for a given analysis.

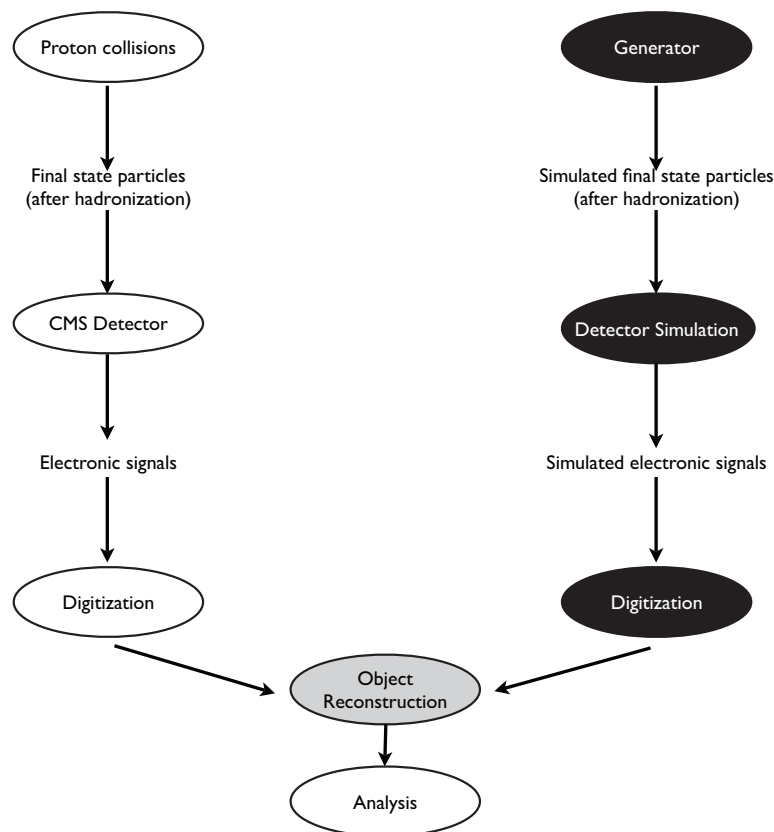


Figure 3.1: Steps towards comparing theoretical predictions and experimental data.

A comparison between the two chains leading to the reconstruction of high-level objects such as jets created in proton collisions and simulated events is shown in Fig. 3.1.

3.1 Event Generators

The evolution of an event, illustrated in the schematic cartoon in Fig. 3.2, can be divided into several steps. To summarize [38]:

1. During the collisions of two protons in the LHC the relevant substructure is characterized by a set of *parton distribution functions* (Sect. 2.1).
2. One parton from each proton initiates a sequence of *branchings*, e.g. $q \rightarrow qg$. These branchings build up an initial-state shower.
3. One parton from each of the initial state showers enters the *hard process*, in which a number of outgoing particles are produced. According to the number of ingoing and outgoing objects one speaks of $2 \rightarrow 2$, $2 \rightarrow 3$ processes, etc.
4. The partons coming from the hard process may *branch* like the incoming partons. Final-state showers are build.

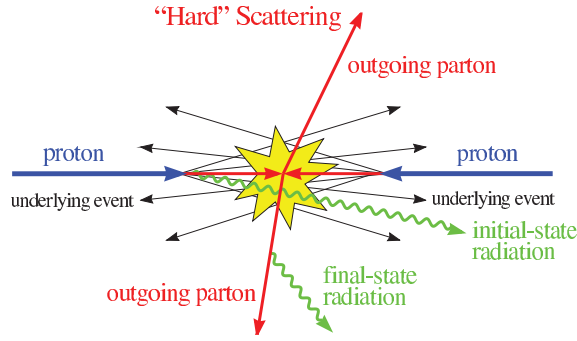


Figure 3.2: Schematic cartoon of a $2 \rightarrow 2$ hard scattering event [42].

5. Due to the strong force the outgoing partons hadronize [12, 38]. Most of the initially produced color neutral hadrons are unstable and decay.

In order to simulate the physics in hadronic collisions from the hard scattering scale (100 GeV) down to the hadronization scale (1 GeV) two kinds of Monte Carlo (MC) techniques exist, Matrix Element (ME) and Parton Shower generators.

- Matrix Element Calculation:

The ME technique is used for processes which correspond to leading or higher order Feynman diagrams plus possible initial and final state radiation. Feynman amplitudes are calculated to describe these processes. The integration over phase space allows then to estimate cross-sections and to generate events. The parton density functions (Sect. 2.1), determined by experiments, as well as model parameters of Beyond Standard Model processes, are input to this part of the event generation process.

- Parton showering and Hadronization:

Parton shower algorithms allow to simulate the successive parton splittings between a given, possibly hard, scattering scale and the scale at which hadronization occurs. Contributing terms of branching in QCD and QED are: $q \rightarrow qg$, $g \rightarrow q\bar{q}$, $g \rightarrow gg$, $q \rightarrow q\gamma$, $e \rightarrow e\gamma$, $\gamma \rightarrow e^+e^-$. For both initial and final state radiation, the algorithm creates a tree-structure of branching, controlled by the DGLAP evolution equation [43]. The branching probability of a parton can be set according to its virtuality. The Parton shower techniques have been found to deliver a good description for soft and collinear radiation.

Two event generators are considered in this analysis, PYTHIA and MADGRAPH/MADEVENT.

PYTHIA contains a library of hard processes, most of them $2 \rightarrow 2$ processes, but also some processes with a higher number of outgoing particles. Different models which describe the hadronization process are also included. The default model in PYTHIA is the Lund String Model [38].

MADGRAPH is a Matrix Element (ME) calculator, it calculates the amplitudes of leading order Feynman diagrams, plus additional initial and final state radiation. The integration over phase space is done in MADEVENT.

The combination of both event generators MADGRAPH/MADEVENT and PYTHIA allows to describe jet production from hard and widely separated QCD radiation (described well by ME) up to the limit of soft and collinear emission (using the Parton shower technique and subsequent hadronization in PYTHIA). The hard process is generated using MADGRAPH/MADEVENT and the resulting output is passed to the PYTHIA Parton shower generator.

Special care needs to be taken to avoid double counting of events between samples with different parton multiplicity at the ME level. For instance, two collinear partons at the ME level can yield the same topology as a single shower confined in a small region of the phase space. Also, a hard resolvable radiation emitted while showering cannot be distinguished from an additional jet due to an extra parton at ME level. To avoid this problem the phase space is divided into two regions, the region of soft and collinear radiation and the region of hard and isolated radiation. Soft/collinear radiation should always be produced by parton showering, hard and isolated radiation by the ME generator. The separation is made by using a cutoff Q_{cut} in the phase space. Two different classes of approaches to solve this problem exist: CKKW algorithms (originally developed by S. Catani, F. Krauss, R. Kuhn and B.R. Webber) [44, 45] and MLM algorithms (originally developed by M.L. Mangano) [46, 47]. It has been shown that the physical results are rather independent of the approach chosen [48].

The k_T MLM algorithm [49] (a particular MLM scheme) is used for the samples in this analysis.

3.2 Reconstruction

The present analysis concentrates on the search for SUSY events with multiple jets and no leptons in the final state. The main concern is therefore the jet reconstruction quality and especially the jet energy resolution. The following section deals with the different steps of the jet reconstruction process and the applied jet quality criteria. In order to separate the desired events from events containing leptons it is also necessary to efficiently identify electrons and muons. The reconstruction of electrons and muons is summarized in this section. No tau veto is applied in this analysis, due to the large uncertainties on tau reconstruction.

Several kinematic variables are used in this section, their definition is based on the global coordinate system of CMS (Appendix A). The most important variables are:

- The azimuth ϕ is defined in the plane transverse to the beam line:

$$\phi = \arctan\left(\frac{y}{x}\right) \quad (3.1)$$

- The pseudorapidity η :

$$\eta = -\ln\left(\tan\left(\frac{\theta}{2}\right)\right), \quad \text{where} \quad (3.2)$$

$$\theta = \arccos\left(\frac{z}{\sqrt{x^2 + y^2}}\right) \quad (3.3)$$

- The difference ΔR between two objects:

$$\Delta R = \sqrt{\Delta\phi^2 + \Delta\eta^2}. \quad (3.4)$$

- The transverse momentum p_T : the momentum emitted transverse to the beam line.
- The longitudinal momentum p_Z : the momentum emitted along the beam line.

3.2.1 Jet Reconstruction

Quarks and anti-quarks as produced in LHC collisions can only combine in color neutral objects [12], via the strong force. The strong force between quarks increases with the distance of the quarks. A new colour neutral pair of quarks is produced once the energy of the force field is sufficiently high. Together with the initial quarks the produced quarks can form new hadrons. After the hadronization process colorless hadrons are moving in the same direction and appear as jets. Almost all hadrons interact with the hadronic calorimeter material, charged hadrons also leave signals in the tracking system. Some hadrons (e.g. $\pi^0 \rightarrow \gamma\gamma$) have photons or electrons as decay products so a certain fraction of the jet energy is stored in the electromagnetic calorimeter.

The goal of jet reconstruction algorithms is to reconstruct their energy and direction by clustering,

either the energy deposits in the detector:

For the purpose of jet reconstruction towers are formed by adding signals in ECAL and HCAL in (η, ϕ) bins corresponding to individual HCAL cells. Energy deposited in towers by clusters of hadrons may be represented in an η - ϕ LEGO Plot as in Fig. 3.3. The reconstructed jets are referred to as calorimeter jets or simply jets in the further course of this analysis.

or directly the stable hadrons as produced in the hadronization process:

This is obviously only possible in simulation where the four vectors of all hadrons are known. These reconstructed jets are referred to as particle jets in the further course of this analysis.

All jets studied in this analysis are reconstructed with the Iterative Cone Algorithm [22]. Calorimeter towers or particles with $E_T > 1$ GeV are considered in decreasing order as starting points (seeds) in an iterative search for stable cones such that all inputs with $\sqrt{\Delta\eta^2 + \Delta\phi^2} \leq R$ from the cone axis are associated with the jet. In the chosen "Iterative Cone 5" algorithm the cone radius R is set to 0.5. A cone is considered stable if its geometric center agrees with the (η, ϕ) location of the sum of the constituent four vectors within a given tolerance. Once a stable cone is found, it is declared a jet and its constituents are removed from the remaining inputs.

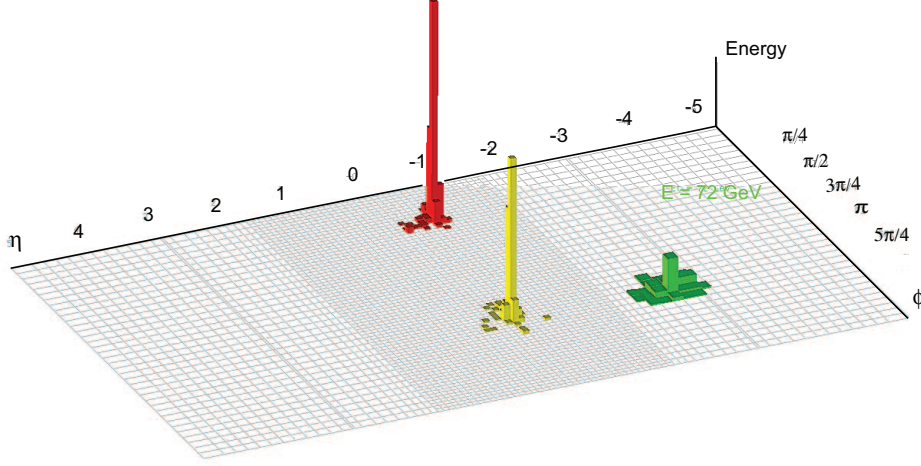


Figure 3.3: Lego plot of a multi-jet event showing the η - ϕ segmentation of the HCAL [22].

The jet transverse energy resolution for reconstructed jets with $|\eta| < 1.4$, as determined with MC simulation, is expected to follow [22]:

$$\frac{\sigma\left(\frac{E_T^{rec}}{E_T^{MC}}\right)}{\left\langle\frac{E_T^{rec}}{E_T^{MC}}\right\rangle} = \frac{5.6}{E_T^{MC}} \oplus \frac{1.25}{\sqrt{E_T^{MC}}} \oplus 0.033, \quad (3.5)$$

where E_T^{rec} is the energy of the reconstructed jet and E_T^{MC} the energy of the corresponding particle jet. The first term in the equation is due to fixed energy fluctuations in the cone from electronic noise, pile-up and underlying event energy, the second term comes from the stochastic response of the calorimeter measurements and the last term is the constant term from residual non-uniformities and non-linearities in the detector response.

3.2.2 Jet Energy Corrections

The goal of jet energy corrections is to correct the jet energy measured in the detector to obtain the energy of the corresponding particle jet [50]. The energy measured in the calorimeter deviates from the energy of this final state particle jet due to several reasons:

1. calorimeter noise;
2. energy depositions outside the jet-cone, the main source being the deflection of the final state particles in the magnetic field of the detector;
3. an inhomogenous response of the calorimeter in different regions of the detector and for particles of different momenta;

4. particle dependent response due to fluctuations in the hadronization process.

In the present analysis only corrections for the effects described in point 2 and 3 are applied. Due to the lack of data at this point the corrections are evaluated from MC simulations. Plans exist to derive the necessary corrections as soon as possible from collision measurements.

The particle jet energy E_C is related to the uncorrected jet energy E by the following formula:

$$E_C = E \times C(\eta) \times C(p_T) \quad (3.6)$$

where $C(\eta)$ is the correction for the η dependence of the calorimeter response and $C(p_T)$ is the correction for the transverse momentum (p_T) dependence of the calorimeter response.

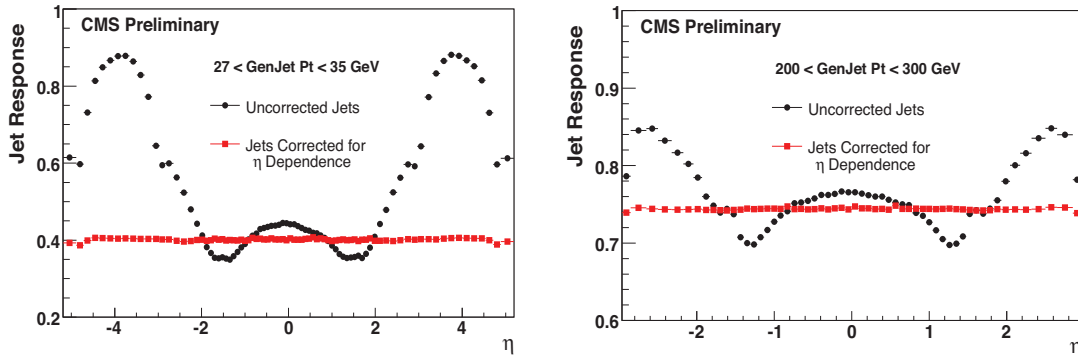


Figure 3.4: Left) Jet response (p_T^{jet}/p_T^{GenJet}) vs. η for particle jets $27 < p_T < 35$ GeV/c both before and after η dependent corrections. Right) Same for $200 < p_T < 300$ GeV/c[50].

The purpose of the correction $C(\eta)$ is to make the jet "response", i.e. the ratio in p_T between the the reconstructed jet and the corresponding particle jet (p_T^{jet}/p_T^{GenJet}), flat as a function of η . The reference value for this correction is the mean response in the $|\eta| < 1.3$ region, which is well covered by the barrel HCAL. The mean jet response in all η regions is corrected to this value. Fig. 3.4 shows the distribution of p_T^{jet}/p_T^{GenJet} as a function of η , before and after the correction in two different jet-energy ranges. The uncorrected jet response is lower than the reference value at the calorimeter edges and higher at high $|\eta|$ regions. The over-response for jets pointing into high $|\eta|$ regions is due their large spread in parallel momenta (p_z) along the beam-line.

The correction factor $C(p_T)$ is determined from jets in the central region of the calorimeter, $|\eta| < 1.3$. The correction factors are chosen such that they correct the most probable value of the reconstructed jet p_T to the most probable value of the corresponding particle jet p_T . The correction factor as a function of the uncorrected jet p_T is illustrated in Fig. 3.5.

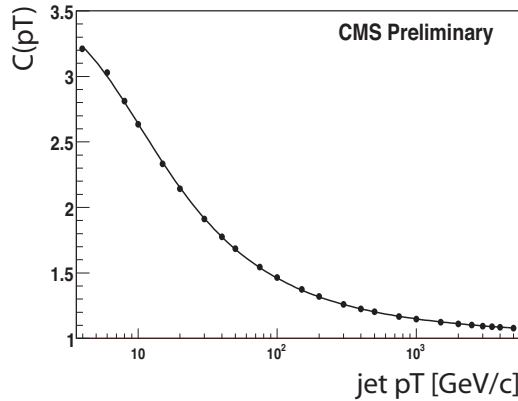


Figure 3.5: The correction factor $C(p_T)$ as a function of the uncorrected jet p_T [50].

3.2.3 Jet Quality Criteria

Only jets which fulfill quality criteria [24] on the jet p_T , η and f_{em} are used in this analysis. The electromagnetic fraction f_{em} is the fraction of the total jet energy ($E(\text{ECAL}) + E(\text{HCAL})$) contributed by energy deposits in the ECAL ($E(\text{ECAL})$)

$$f_{em} = \frac{E(\text{ECAL})}{E(\text{ECAL}) + E(\text{HCAL})}. \quad (3.7)$$

The jet energy resolution worsens with decreasing jet momentum (Eq. 3.5), therefore a minimal requirement on the energy-corrected transverse momentum of the jets is useful. The jet should also point into a detector region which is well covered by the HCAL detector (Fig. 2.5), which constrains the allowed pseudo-rapidity. In MC studies an upper limit of 0.9 on f_{em} has been found useful to reject electrons misidentified as jets. Furthermore in the CRAFT 2008 cosmic run we learned that jets reconstructed in absence of collisions, e.g. due to noisy towers in the HCAL, can be identified by their lack of energy in the electromagnetic calorimeter [24]. This justifies a lower limit on the electromagnetic fraction. The selection cuts are $p_T > 50 \text{ GeV}/c$, $|\eta| < 3$, $0.01 < f_{em} < 0.9$. Experience with collision data will help to retune this values.

3.2.4 Muon Reconstruction

A good muon and electron reconstruction is necessary to separate leptonic background from the desired full hadronic signal topology. The reconstruction algorithm used in this analysis is the so-called global muon reconstructor. The *global muon* reconstructor is based on the *standalone* and the *local muon* reconstructor [51].

The *local muon* reconstructor reconstructs muon track segments inside the muon system from hits measured with the different gaseous detectors in the muon system. The track segments are taken as seeds for the *standalone* muon reconstructor. The seed define a region of interest used for further reconstruction. The *standalone* muon reconstructor combines

the reconstructed track segments of the local muon reconstructor with information from the resistive plate chambers to form a complete track through the muon system, using the Kalman filter technique [52]. This track is then extrapolated towards the beamline.

The *global muon* reconstructor combines the reconstructed tracks of the *standalone* muon reconstructor with hits measured by the silicon tracker and the pixel detector. Muon energy loss in the material and effects of multiple scattering are taken into account. A refit is done to find the best track by matching the information from the muon and tracker systems [22].

3.2.5 Muon Isolation

Three isolation techniques can be distinguished: ECAL isolation, HCAL isolation and tracker isolation. The three techniques are based on the measurement of the momentum (track isolation) or energy (HCAL and ECAL isolation) deposited into two cones around the reconstructed muon track (Fig. 3.6). The cones are defined by the maximum value

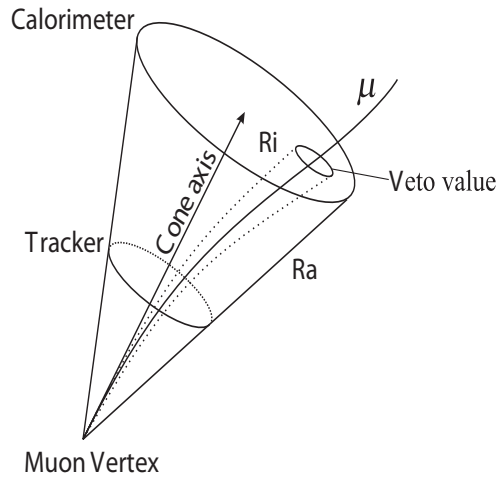


Figure 3.6: Schematic illustration of the isolation cones. The muon direction at the vertex defines the cone axes. The energy deposit ($\sum p_T, \sum E_T$) in the outer cone, with the radius ΔR_a , is computed, and the contribution of the muon itself is removed by excluding the veto cone, with the radius ΔR_i [22].

of $\Delta R = \sqrt{(\Delta\eta)^2 + (\Delta\phi)^2}$, where $\Delta\eta$ and $\Delta\phi$ are the difference in pseudorapidity and azimuthal angle between the deposit and the cone axis, respectively. The radius of the inner cone is ΔR_i , the radius of the outer cone is ΔR_a . The cone axes are defined by the muon direction at the vertex.

The inner cone, also called veto cone, should contain most of the energy deposited by the muon itself. The energy deposited in the veto cone, the veto value, is subtracted from

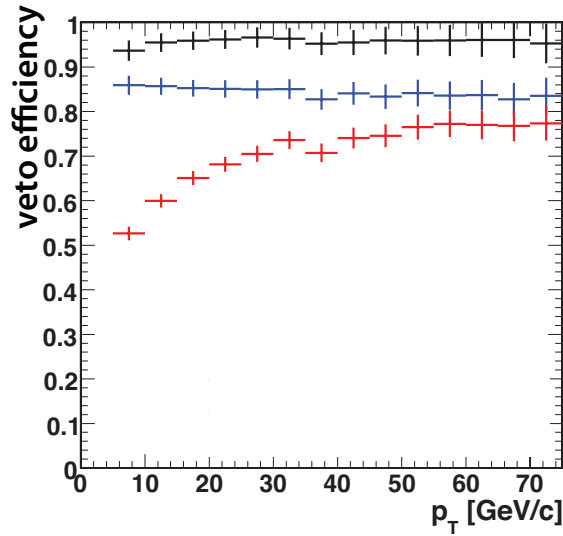


Figure 3.7: Muon reconstruction and veto efficiency for muons as determined in the LM0 SUSY sample. The efficiency is shown in black for the case that no isolation requirement is applied, in blue if tracker isolation is required and in red if the combined relative isolation is used.

the energy deposited in the outer cone. The remaining energy, $I(\text{tracker})$, $I(\text{ECAL})$ and $I(\text{HCAL})$ for tracker, ECAL and HCAL isolation respectively, should be close to zero if the muon is isolated. Further information on the isolation algorithm, such as energy thresholds of contributing tracks and calorimeter towers, can be found in Ref. [22].

The isolation criteria used in this analysis are a combination the three algorithms. They allow for a high muon veto efficiency even for low momentum muons [53].

A muon is defined as isolated if:

$$\begin{aligned} I(\text{tracker}) &< 5.0 && \text{for } p_T(\mu) < 30 \text{ GeV}/c \\ (I(\text{ECAL}) + I(\text{HCAL}) + I(\text{tracker}))/p_T(\mu) &< 0.1 && \text{for } p_T(\mu) > 30 \text{ GeV}/c, \end{aligned} \quad (3.8)$$

where A cut on the tracker isolation improves the muon veto efficiency for low momentum muons compared to a cut on the combined relative isolation $I(\text{comb})$:

$$I(\text{comb}) = [I(\text{ECAL}) + I(\text{HCAL}) + I(\text{tracker})]/p_T(\mu) \quad (3.9)$$

as illustrated in Fig. 3.7. The veto efficiency is defined as the ratio between the number of reconstructed and identified leptons and the number of all initial leptons generated in the hard scattering process which fulfill the requirement $p_T > 5 \text{ GeV}/c$ and $|\eta| < 2.4$.

3.2.6 Muon Quality Criteria

Certain quality criteria can be used to distinguish between muons created in the hard scattering process of an event, muons generated in Kaon or pion decays in-flight and Kaons or pions which reach the muon chamber and are therefore mis-identified as muons [54]. The most powerful quality criteria are the reduced χ^2 of the global muon fit, the minimal

distance between the reconstructed track and the beam spot measured transversally to the beam-line (d_0) and the number of hits in the silicon tracker associated to the muon track (N_{hits}). The chosen selection requirements are a reduced χ^2 smaller than 10, $d_0 < 2$ mm and $N_{hits} \geq 11$. These cuts are based on Monte Carlo studies and need to be refined with collision data.

3.2.7 Electron Reconstruction

Electron and photon showers deposit their energy in several crystals in the electromagnetic calorimeter (ECAL). Most of the energy ($\approx 94\%$) of a single electron is contained in a 3×3 matrix of crystals, 97% is contained in a 5×5 matrix. However the presence of material in front of the calorimeter results in bremsstrahlung and photon conversion. The strong magnetic field spreads the energy deposit in ϕ . Search algorithms have been developed to cluster those crystals in which the energy of one incident electron is deposited. The Hybrid Supercluster Algorithm is used in the ECAL barrel and the Island algorithm in the endcap [55].

The seed of the Hybrid supercluster algorithm is a collection of 3 to 5 contiguous crystals in η . If such a seed is found a dynamic search for other collections close in ϕ is triggered. The Island Algorithm builds clusters by connecting rows of crystals in η and in ϕ containing energies decreasing monotonically when moving away from a seed crystal. The seed is a crystal whose energy is a local energy maximum above a defined threshold. Superclusters are build starting from the most energetic cluster and then collecting all the other nearby clusters in a very narrow η -window and a much wider ϕ -window.

Electrons are reconstructed starting from superclusters in the electromagnetic calorimeter. Superclusters are used to select trajectory seeds built by the combination of tracker hits in the innermost tracker layers. The seeding algorithm makes use of pixel and TEC layers (Sec. 2.3.4) in order to cover the forward region where the pixel detector becomes inefficient. This seeding strategy is complemented by a tracker driven approach to cover cases of very low p_T electrons and non isolated electrons.

The seeds are then used to trigger the track finding. The track fit is performed using a Gaussian Sum Filter (GSF) [56], which allows the track to be extrapolated out to the ECAL surface, despite kinks due to radiated bremsstrahlung.

3.2.8 Electron Isolation

As for muons electron isolation is based on the momentum (tracker isolation) or energy (HCAL and ECAL isolation) deposited in an inner and outer cone around the electron track [55].

- tracker isolation:

The sum of p_T of tracks in the inner veto cone is subtracted from the sum of p_T of tracks in the outer cone. The inner veto cone radius is 0.015, the outer cone radius is 0.3. Only tracks with $p_T > 1$ GeV/c are taken into account.

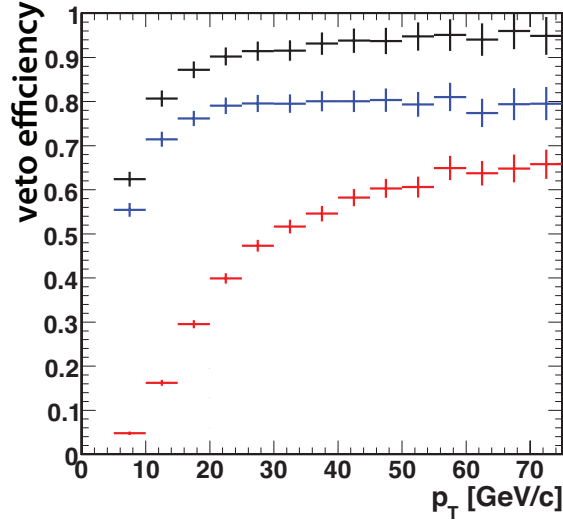


Figure 3.8: Electron reconstruction and veto efficiency for muons as determined in the LM0 SUSY sample. The efficiency is shown in black for the case that no isolation requirement is applied, in blue if tracker isolation is required and in red if the combined relative isolation is used.

- ECAL isolation:

The energy deposited inside the inner cone as well as the energy deposited inside strips of width $\eta = 0.02$ on both sides of the ECAL supercluster center are subtracted from the sum of the energy in the outer cone. The outer cone radius is set to 0.4, the veto cone radius to 0.045 in the barrel, and 0.07 in the endcap. To minimize the effect of calorimeter noise only crystals with energies above 0.08 GeV in the barrel and 0.3 GeV in the endcap are taken into account.

- HCAL isolation:

The HCAL isolation variable is based on the energy deposited in the layers of hadron calorimeter towers inside a cone centered on the electron supercluster position. The outer cone radius is 0.4.

The following isolation requirements are used in this analysis:

$$\begin{aligned} I(\text{tracker}) &< 3.0 && \text{for } p_T(\mu) < 30 \text{ GeV}/c \\ (I(\text{ECAL}) + I(\text{HCAL}) + I(\text{tracker}))/p_T(\mu) &< 0.1 && \text{for } p_T(\mu) > 30 \text{ GeV}/c, \end{aligned} \quad (3.10)$$

Like the muon isolation the electron isolation is studied in detail in Ref. [53]. The effect of using the tracker isolation for low momentum electrons is illustrated in Fig. 3.8.

3.2.9 Missing Transverse Energy (calorimeter based)

To reconstruct the missing transverse energy [57] the transverse vector sum over the energy deposits in calorimeter towers (ECAL plus HCAL) E_T^{miss} is calculated:

$$\vec{E}_T^{\text{miss}} = - \sum_n (E_n \sin \theta_n \cos \phi_n \vec{i} + E_n \sin \theta_n \sin \phi_n \vec{j}), \quad (3.11)$$

where the index n runs over the energy deposits in towers. Here \vec{i}, \vec{j} are the unit vectors in the direction of the x and y axis of the CMS right-handed coordinate system (Appendix A).

The resolution $\sigma(E_T^{miss})$ can be parametrized according to the following form:

$$\sigma(E_T^{miss}) = A \oplus B\sqrt{\sum E_T - D} \oplus C(\sum E_T - D). \quad (3.12)$$

Here $\sum E_T$ is the scalar sum over all energy deposits in individual calorimeter towers. The above parametrization factorizes A, B, C into a priori uncorrelated effects. The A ("noise") term represents electromagnetic noise, pile-up (PU), and underlying event (UE) (sec. 2.1); the B ("stochastic") term represents the statistical sampling nature of the energy deposits in individual calorimeter towers; the C ("constant") term represents residual systematic effects due to non-linearities, cracks and dead material; the D ("offset") term represents the effects of noise and pile-up on $\sum E_T$. The resolution of E_T^{miss} has been studied for simulated QCD dijet events. Figure 3.9 shows $\sigma(E_T^{miss})$ vs. the total transverse energy $\sum E_T$ and a fit to the resolution. The resulting values of A, B, C and D are shown in Table 3.1.

Table 3.1: Fit parameters of eq. 3.12 as estimated from MC simulation for QCD dijet events.

A	1.5 ± 0.3
B	1.03 ± 0.03
C	0.023 ± 0.002
D	82 ± 9

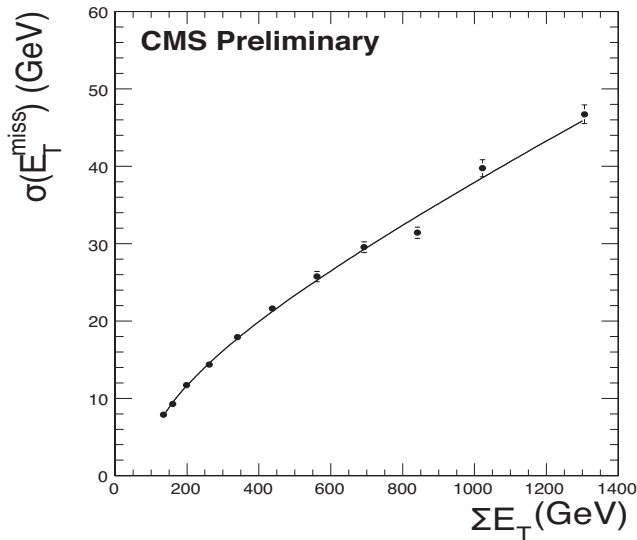


Figure 3.9: Resolution $\sigma(E_T^{miss})$ vs. $\sum E_T$ for simulated QCD events. The resolution fit is indicated by the black line [57].

3.2.10 Trigger and Data Acquisition

The planned maximum bunch crossing rate at the LHC is about 40 MHz. On average 20 interactions will take place at one bunch crossing in this high luminosity phase of the LHC ($L \approx 10^{34} \text{ cms}^{-2} \text{ s}^{-1}$). The corresponding data rate in the CMS detector will be of the order of 1 GHz. Today's storage devices are restricted to a storage capability of about 100 Hz at data rates of $\sim 100 \text{ MB/s}$.

However, only the interactions where partons collide inelastically are of interest at the CMS detector.

The task of the trigger system is to reduce the amount of data, by identifying and storing only "interesting" events. To fulfill this task, the trigger system rejects or accepts events by certain criteria. The trigger system provides different triggers which vary in the used criteria. The user can choose the trigger which fits best for his analysis in terms of signal efficiency and background rejection. Criteria might be for example the lepton momentum or the amount of energy stored inside the calorimeters.

The CMS trigger system works in two steps to suppress the storage of "uninteresting" events. The two steps are the Level-1 trigger and the High-Level trigger. The High-Level Trigger System can be roughly divided into Level-2 and Level-3 triggers. At each level the sorting criteria get stricter and the sorting more time consuming.

1. Level-1 Trigger [21]:

The Level-1 trigger uses coarsely segmented detector data from muon detectors and calorimeters. The information of different subsystems is not combined. The high-resolution data is held in pipeline memories. The Level-1 trigger is based on custom electronics. The decision has to be available only $3.2 \mu\text{s}$ after the corresponding bunch crossing, to limit the amount of data stored in the pipeline memories. The Level-1 trigger lowers the passed rate of events to 100 kHz. Different thresholds are used for low and high luminosity scenarios, due to the different amount of data. Once the Level 1 trigger accepts an event, the high-resolution data is readout of the front-end electronics and then piped to the High-Level trigger.

2. High-Level Trigger (HLT) [58]

The decision of this trigger system is based on PC farms running CMS software. A Level-2 trigger uses typically only the information from the calorimeter and the muon system. For the Level-3 triggers the information from distinct detector parts are combined and full tracks are reconstructed. The HLT system reduces the event rate to 100 Hz.

The special set of trigger chosen in this analysis is described in Sect. 4.4 .

Chapter 4

Supersymmetry in Multijet Events

The goal of the presented analysis is to compare several ways of searching for Supersymmetry (SUSY) in events with multiple high momentum jets and a large fraction of missing transverse energy. A common approach for such a SUSY search is to apply a strong cut on calorimeter based missing transverse energy (E_T^{miss}) (Sect. 3.2.9) in order to reject a large part of the QCD multijet background [16]. Different alternatives to this approach are studied and compared in terms of their performance in background rejection, signal efficiency and robustness against systematic uncertainties.

4.1 Monte Carlo Data Samples

4.1.1 Signal

The low mass mSuGra [10] test points (LM0 - LM5 of Table 1.4) are generated with PYTHIA6 [38]. The program SoftSUSY [59] is used to solve the renormalization group equations [15] and to calculate mass spectra of superparticles. The branching ratios are computed using SUSY-HIT [60]. The leading order cross-section and the number of generated events are shown in Table 4.1. A list of the mSuGra parameter-sets used to generate these samples has been given in Table 1.4 in Chapter 1. In the following events generated with a special parameter-set X ($X = 0, \dots, 5$) are called LMX SUSY events.

4.1.2 Background

Background events for this search are non-SUSY events which fulfill the requirement of having multiple hard jets, no reconstructed isolated leptons and containing missing transverse energy. Missing transverse energy originates either from neutrinos escaping the detector, from calorimeter noise, or from jets and leptons which have not been properly reconstructed. Events which contain τ -leptons are also a background as no τ -veto is applied. The following simulated data-sets have been investigated:

Table 4.1: Leading order (LO) cross-section, obtained from PYTHIA6 [38], and number of generated events for five different mSuGra parameter-sets. Further details about these parameter-sets have been given in Table 1.4.

Sample	σ LO (pb)	# generated events
LM0	110	202 686
LM1	16.1	104 800
LM2	2.4	130 400
LM3	11.8	153 000
LM4	6.7	110 400
LM5	1.9	171 600

- Multijet QCD events simulated with MADGRAPH/MADEVENT (MG/ME) [39] in combination with the parton shower algorithm provided by PYTHIA (Sect. 3.1). The MG/ME sample is produced in bins of H_T^{ME} , where H_T^{ME} is the total scalar momentum of the matrix element partons (u, d, s, c, b). QCD radiation is described for $2 \rightarrow 2, 3, 4$ parton processes. To decrease the statistical uncertainties in the $H_T^{ME} = 250\text{-}500$ GeV/c bin of the MADGRAPH sample, an additional 50 million MG/ME events are used, for which the detector response was modeled in a fast simulation [22] in contrast to the full GEANT4 [33] simulation used for all other samples.
- $t\bar{t}$ events simulated using MG/ME. Spin correlation in top decays is taken into account using the DECAY package [39]. QCD radiation is described for up to three extra ME partons beside the top-quark pair system. The top decays inclusively and without constraints on the momenta or direction of the decay products.
- $W \rightarrow \ell\nu$ events simulated with MG/ME. QCD radiation is described for up to four ME partons. The W bosons are forced to decay into electron, muon and tau pairs.
- $Z \rightarrow \ell\bar{\ell}$ events simulated with MG/ME. QCD radiation is described from one to up to four ME partons. The Z boson, which can be virtual, is generated with $m_Z > 50$ GeV. The Z boson is forced to decay into electrons, muons and taus.
- $Z \rightarrow \nu\bar{\nu}$, events simulated with MG/ME. QCD radiation is described for up to four ME partons. On generator level only events in which $p_T(Z) > 50$ GeV/c are selected.

All samples are generated at center of mass energy of 10 TeV, using CTEQL6 Parton Density Functions [61] and the underlying event tuning described in Ref. [62]. Table 4.2 states the cross-sections and the number of generated events for each of the various background samples.

4.2 Kinematic Quantities

Several kinematic quantities are used in this chapter. The most prominent one is the missing transverse energy. Three different incarnations of this variable are utilized throughout this text: \vec{E}_T , \vec{E}_T^{miss} and \vec{H}_T^{miss} .

Table 4.2: Leading order cross section and number of generated events for the Standard Model (SM) samples studied in this thesis.

Sample	σ LO (pb)	# generated events
QCD ($100 < H_T^{ME} < 250$ GeV/c)	15 000 000	12 662 923
QCD ($250 < H_T^{ME} < 500$ GeV/c)	400 000	4 874 539
QCD ($500 < H_T^{ME} < 1000$ GeV/c)	14 000	4 570 718
QCD ($1000 < H_T^{ME} < \infty$)	370	1 046 863
QCD ($250 < H_T^{ME} < 500$ GeV/c) fast simul.	400 000	35 900 000
$t\bar{t}$	317	946 644
$W \rightarrow \ell\nu$	40 000	9 745 661
$Z \rightarrow \ell\bar{\ell}$	3 700	1 262 816
$Z \rightarrow \nu\bar{\nu}$	2 000	1 018 866

- $\vec{\cancel{E}}_T$ is calculated on the level of generator truth before the detector simulation. It is the negative vector sum of the transverse momenta of all n particles in the final state of an event, except for neutrinos, muons or SUSY LSP (Sect. 1.3). Muons are excluded from the calculation since they also do not contribute to calorimeter based \vec{E}_T^{miss} (Sect. 3.2.9).

$$\vec{\cancel{E}}_T = - \sum_{j=1}^n \vec{p}_{T,j}. \quad (4.1)$$

- \vec{E}_T^{miss} is the calorimeter based missing transverse energy introduced in Sect. 3.2.9.
- \vec{H}_T^{miss} is calculated from n reconstructed (Sect. 3.2.1) and energy corrected (Sect. 3.2.2) jets which pass a set of quality criteria (Sect. 3.2.3).

$$\vec{H}_T^{miss} = - \sum_{j=1}^n \vec{p}_{T,j}. \quad (4.2)$$

Another important quantity is the total scalar momentum in an event H_T . This quantity is reconstructed by building the scalar sum of the transverse momenta of n jets:

$$H_T = \sum_{j=1}^n |\vec{p}_{T,j}| \quad (4.3)$$

For simplicity the absolute values of $\vec{\cancel{E}}_T$, \vec{E}_T^{miss} and \vec{H}_T^{miss} are denoted by: \cancel{E}_T , E_T^{miss} and H_T^{miss} .

4.3 Properties of mSuGra Points

This section discusses the properties of mSuGra events. Characteristic observables are compared on generator level. The event topology studied in this analysis has been introduced in Chapter 1. The goal is to be sensitive to mSuGra events with multiple high

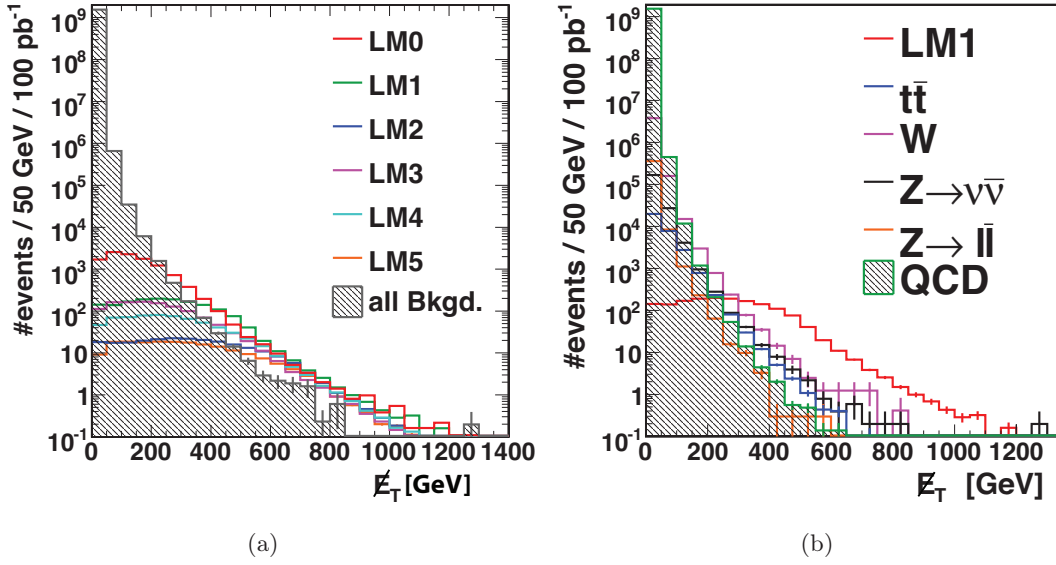


Figure 4.1: Distribution of \cancel{E}_T for a) events of the individual SM background processes and LM1 SUSY events and, b) SUSY events of the five different parameter-sets and a combination of all background events.

momentum jets, no leptons and large \cancel{E}_T . The missing transverse energy is due to the lightest stable particles¹ in the final states of the squark and gluino decays and is a basic property of R -parity conserving SUSY. Assuming that the Lorenz four-vectors of all visible particles in the final state of an event are known the missing transverse energy \cancel{E}_T due to escaping neutrinos and lightest stable particles can be calculated from energy and momentum conservation (Sect. 4.2). This generator level equivalent to \vec{E}_T^{miss} is presented in Fig. 4.1(a) for different SUSY signal samples and a combination of all backgrounds. The same quantity is shown for LM1 SUSY events and the standard model background processes in Fig. 4.1(b). The contribution from SUSY events exceeds the standard model expectations.

In this analysis events which contain isolated leptons are rejected (hadronic searches), in contrast to which specifically ask for leptons, thus reducing the SM background. Hadronic searches cover a wider part of the mSuGra parameter space but are more affected by QCD multijet background. By rejecting events with leptons backgrounds from $W \rightarrow \ell\nu$ and $t\bar{t}$ events can be reduced, as illustrated in Fig. 4.2(a). The number of expected electrons plus muons which fulfill the selection cuts ($|\eta| < 2.4$ and $p_T > 10$ GeV/c) is shown, once for LM1 SUSY events and events of the different SM background processes (Fig. 4.2(a)), and once for SUSY events generated with different parameter-sets and a combination of all backgrounds (Fig. 4.2(b)). The number of expected muons or electrons in SUSY events is directly related to the mass of sleptons and squarks. Should sleptons be lighter than squarks the decay of neutralino or chargino into lepton + slepton can be favored over the decay quark + squark [10], which would increase the total number of leptons in the event.

¹ $\tilde{\chi}_1^0$ for the parameter-sets studied in this analysis

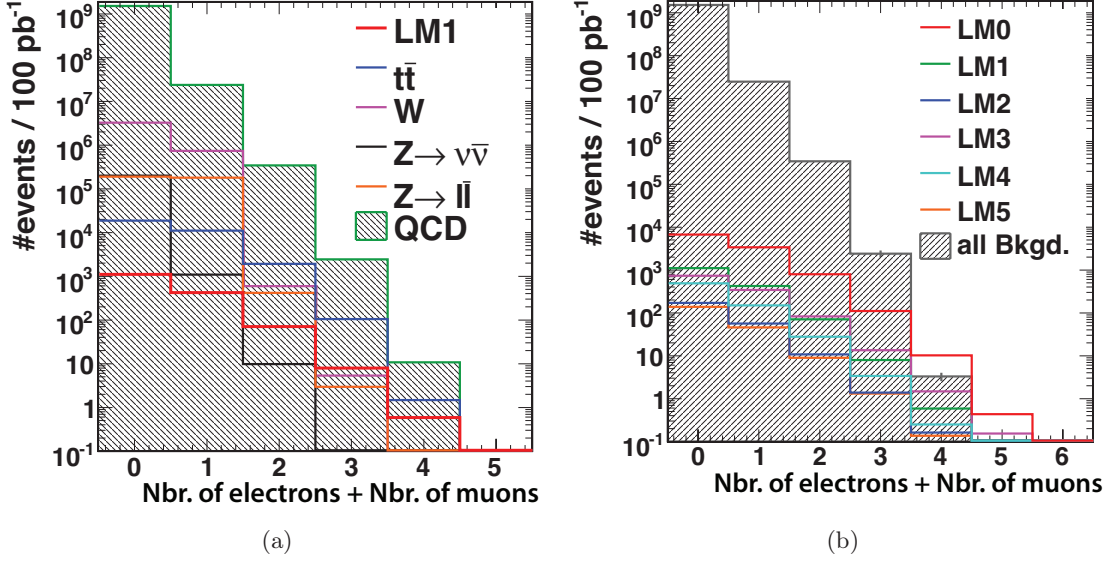


Figure 4.2: Number of generated electrons plus muons for SM background events and LM1 SUSY events (a) and for SUSY events of the five parameter-sets and a combination of all background events (b). Both electrons and muons are required to fulfill $p_T > 10$ GeV/c and $|\eta| > 2.4$.

A sizable amount of signal events remains even after the rejection of events containing muons or electrons.

In the MSSM (Sect. 1), the primary SUSY particles are heavy. Depending on the mass difference between them and their daughters the multiplicity (Fig. 4.3) and the momenta of particle jets (Sect. 3.2.1) can be high. The largest jet momentum in an event (leading jet p_T) is shown in Fig. 4.4, for SUSY events generated with different parameter-sets and a combination of all backgrounds. Cuts on the jet momenta and multiplicity reduce the contribution of SM background events while keeping a high signal efficiency for the SUSY parameter-sets. In particular, the contribution of SM background decreases with increasing jet multiplicity.

The distribution of the leading jet pseudo-rapidity (η) for SM background events and LM1 SUSY events is presented in Fig. 4.5(a). The distribution is similar for QCD, $W \rightarrow \ell\nu$, $Z \rightarrow \nu\bar{\nu}$ and $Z \rightarrow \ell\bar{\ell}$ events. In these events jets originate from initial state radiation or from the underlying event, or for QCD events also from final state radiation. For $t\bar{t}$ events the distribution is nearly as steep as for SUSY events. In $t\bar{t}$ events jets can originate from the hadronic decay of a W -boson or from a b -quark and are generally of higher momentum than jets from initial state radiation.

In Figure 4.5(b) the $|\eta|$ -distribution is shown for SUSY events generated with different parameter-sets. The higher the mean transverse momenta of the leading jets (Fig. 4.4) the more central is their distribution in the detector.

These features of SUSY events are used in my event selection to suppress SM background, while keeping a high signal efficiency.

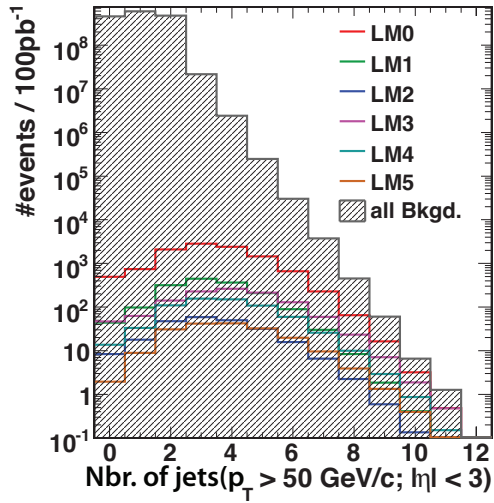


Figure 4.3: Multiplicity distribution of particle jets (Sect. 3.2.1) with jet $p_T > 50$ GeV/c in $|\eta| < 3$.

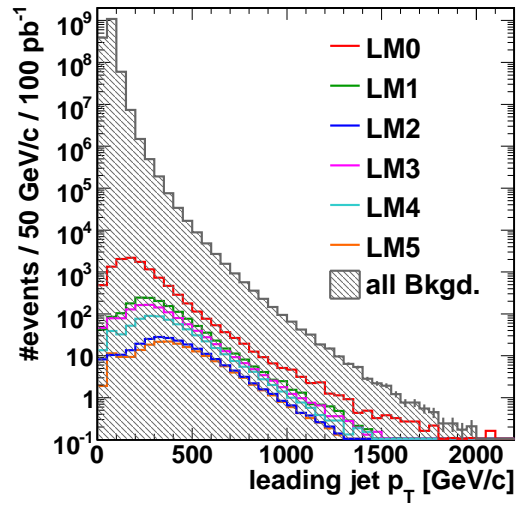
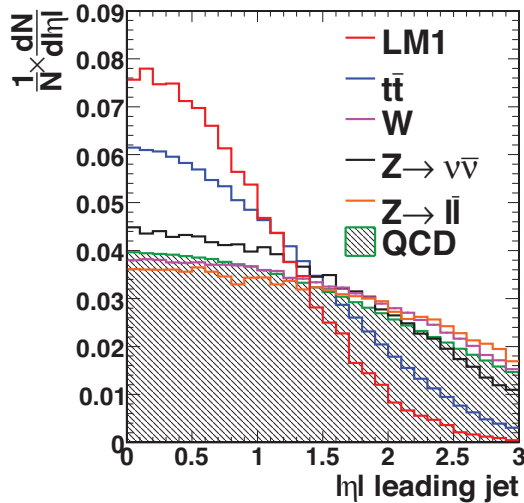
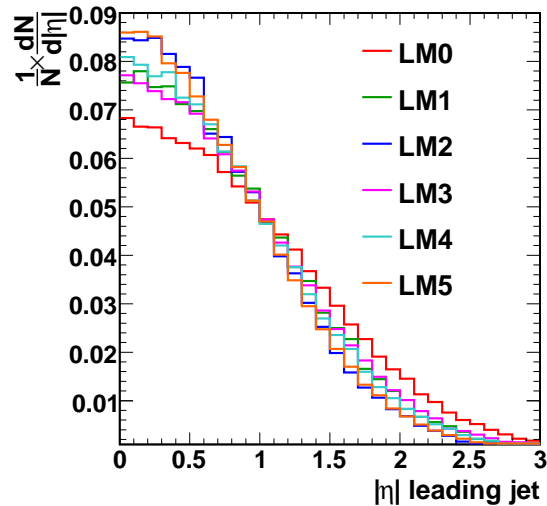


Figure 4.4: p_T distribution of the leading particle jet.



(a)



(b)

Figure 4.5: $|\eta|$ distribution of the leading particle jet ($p_T > 50$ GeV/c), for SM background events and LM1 SUSY events (a), and for SUSY events of the five parameter-sets (b). The individual contributions are normalized to unit area.

4.4 Online Selection

In this section the efficiencies of the various High-Level Trigger (HLT) paths (Sect. 3.2.10) are discussed. The trigger efficiency is determined using MC generated events which are passed through the detector simulation (Chapter 3). In particular, jet and missing energy triggers have been studied in detail. The jets and E_T^{miss} in the HLT selection are computed in the same way as the jets and E_T^{miss} in the offline selection (Sect. 3.2.1 and 3.2.9). SUSY events generated with parameter-sets LM0 and LM1 are used to estimate the trigger efficiency for signal events. The following jet triggers are found to be adequate for this analysis:

- single jet trigger which requires at least one jet with jet transverse momentum larger than 110 GeV/c (HLT 1 Jet),
- dijet trigger which requires at least two jets both with an average transverse momentum of more than 70 GeV/c (HLT Di-Jet).

As both triggers will be prescaled with higher luminosities, alternative trigger paths have been investigated. Two trigger paths could be used for the online selection, a missing energy trigger of at least 75 GeV/c (HLT E_T^{miss}) and a combination of (i) a single jet trigger with higher threshold of 180 GeV/c (ii) a three-jet trigger (three jets each with $p_T > 85$ GeV/c) and (iii) a four-jet trigger (four jets each with $p_T > 65$ GeV/c) (HLT Combi).

The trigger efficiencies for mSuGra events are shown by red bars in Fig. 4.6(a) and 4.6(b) for LM0 and LM1 SUSY events respectively. The trigger efficiency for LM0 mSuGra events varies between 80% (HLT 1 Jet) and 60% (HLT E_T^{miss} and HLT Combi). The trigger efficiency is higher for LM1 SUSY events than for LM0 SUSY events, in agreement with the properties of the different mSuGra points discussed in the previous section.

It is also important to verify whether the trigger rejects events which would otherwise pass the offline event selection. The offline selection in this analysis is divided into two parts, a common pre-selection and a final selection in which four different variables are compared. The ratio between the number of pre-selected events with and without the trigger requirement is indicated by the green bars in Fig. 4.6(a) and 4.6(b). The single and the dijet triggers do not reject SUSY events which would otherwise pass the preselection. The HLT E_T^{miss} and the HLT Combi trigger path would reject about 20% of SUSY LM0 events and 6% of SUSY LM1 events would pass the pre-selection.

The single-jet trigger is used for the results presented in this analysis. A detailed discussion of CMS High Level Triggers Algorithms and their efficiencies can be found in Ref. [63].

4.5 Object Definition

In this section the quality criteria for jets and leptons used throughout this analysis are summarized.

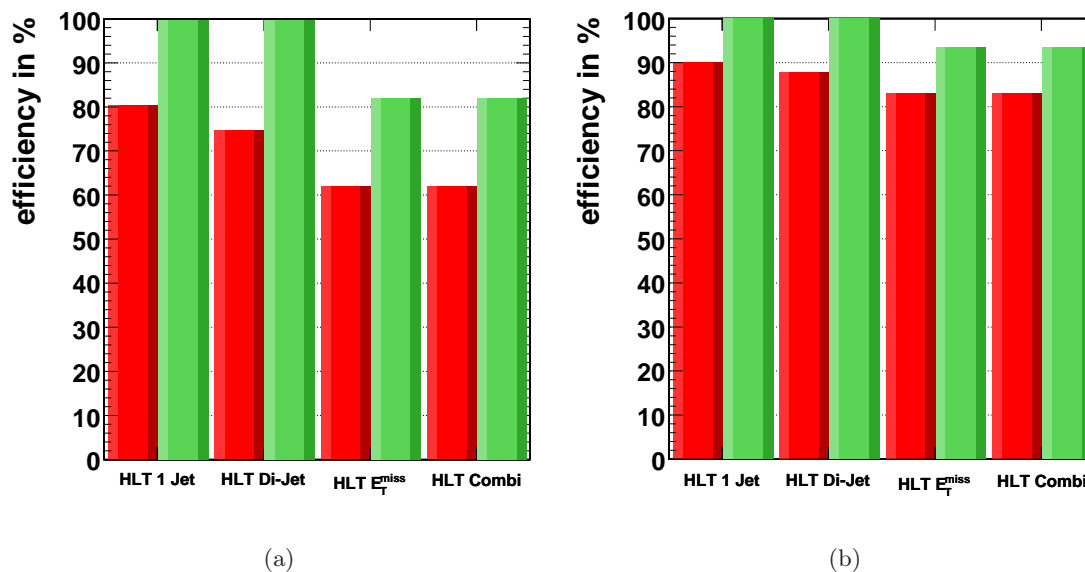


Figure 4.6: Trigger efficiencies for mSuGra events of parameter set LM0 (a) and parameter-set LM1 (b). The four different trigger paths described in the text are compared. The trigger efficiency (number of triggered events/total number of events) is shown in red. The bars in green indicate the ratio between the number of preselected events with and without the trigger requirement.

- Good Muon:

Isolated global Muons (Sect. 3.2.4 and Sect. 3.2.5) are counted as *good* muons if they pass the following requirements:

- $p_T > 10 \text{ GeV}/c$,
- $|\eta| < 2.4$.

- Good Electron:

Isolated electrons (Sect. 3.2.7 and Sect. 3.2.8) are counted as *good* electrons if they fulfill the following requirements:

- $p_T > 10 \text{ GeV}/c$,
- $|\eta| < 2.4$.

- Good Jet:

Calorimeter energy deposits are clustered in jets using an iterative cone algorithm (Sect. 3.2.1). The energies of these jets are corrected for detector effects (Sect. 3.2.2). The jets are required to fulfill (Sect. 3.2.3):

- $p_T > 50 \text{ GeV}/c$,
- $|\eta| < 3.0$,
- $0.01 < f_{em} < 0.9$, where f_{em} is the fraction of energy contributed by ECAL energy deposits.

Special care is taken of jets closer than $\Delta R = 0.2$ to a non-isolated global muon ($p_T > 10 \text{ GeV}/c$) which fulfills the additional quality criteria stated in Sect. 3.2.6. In this case the muon originates most probably from the jet and a fraction of the total particle jet energy is deposited in the muon chambers. A jet closer than $\Delta R = 0.2$ to such a muon is in 75% of times matched to a particle jet originating from a b or c decay compared to 25% for other jets. This numbers have been estimated for LM1 SUSY events before any event selection. To account for the energy deposited in the muon chamber the muon momentum is added vectorially to the jet momentum. A fraction of 7% of all *good* jets in triggered LM1 SUSY events have been corrected in this way. Fig. 4.7 shows the jet-momentum resolution of jets which are closer than $\Delta R = 0.2$ to a non-isolated global muon before and after this jet-energy correction. The momentum resolution is defined as the ratio of Δp_T , the difference in transverse momentum between a reconstructed jet $p_T(\text{rec.})$ and its matched particle jet p_T , to the transverse momentum of the particle jet.

$$[p_T(\text{rec.}) - p_T]/p_T = \Delta p_T/p_T. \quad (4.4)$$

A reconstructed jet is matched to the closest particle jet in ΔR when $\Delta R < 0.5$. The distribution is shifted to negative values of $\Delta p_T/p_T$. Before correction, the reconstructed momentum $p_T(\text{rec.})$ of jets close to non-isolated muons is in general smaller than the energy of the corresponding particle jet p_T . A fit of a gaussian distribution to $\Delta p_T/p_T$ yields a mean of -0.214 ± 0.003 and a σ of 0.162 ± 0.002 . After correction the distribution is centered closely around zero (mean = -0.062 ± 0.002 and sigma = 0.146 ± 0.002). The small remaining shift of the mean is due to the fact that not all of the muons which originate from jets fulfill the tight quality criteria of our selection. The quality criteria have been optimized for purity rather than efficiency, as wrongly corrected jets could introduce long positive tails to the $\Delta p_T/p_T$ distribution.

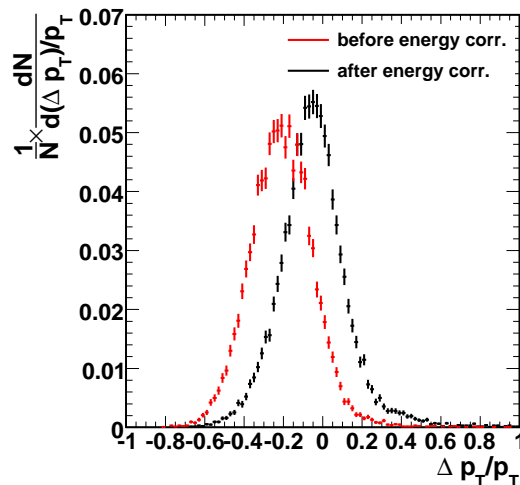


Figure 4.7: Jet momentum resolution before and after correction for non-isolated muons closer than $\Delta R = 0.2$ to the jet-axis, for LM1 SUSY events.

4.6 Offline Preselection

A common approach for a hadronic SUSY search is to apply strong cuts on E_T^{miss} . In this analysis the performance of alternative variables to E_T^{miss} are compared after a common preselection. This preselection defines the topology of the events. Events are selected which contain no *good* electrons or muons but multiple *good* jets, as defined in the previous section. The final selection variables studied in this analysis are based on *good* jets and allow to distinguish between events with missing transverse energy and events in which the transverse momenta of all jets are balanced. Special care is taken to reject events in which a badly measured jet takes away a large fraction of the total energy in the event. A final optimization is only possible using information from collision data. The events are selected as follows:

1. Lepton veto:
All events in which at least one *good* muon or one *good* electron has been identified are rejected.
2. Cut on jet multiplicity:
Only events with a minimum of two and a maximum of six *good* jets are selected. At least two of the *good* jets should have a transverse momentum larger than 100 GeV/c in accordance with the expected high p_T of SUSY jets discussed in Sect. 4.3.

A minimum number of two *good* jets is required as some of the quantities used in the final event selection (described later in the text) can only be calculated for at least two jets. A maximum number of six *good* jets is accepted, as the calculation of these quantities needs several iterations, the number of which depends on the number of jets. An upper limit of six jets reduces the time needed for the calculation while keeping a high signal efficiency.
3. Bad jet veto:
Jets which do not fulfill all quality criteria could still carry a sizable fraction of the total energy. If these jets are not accounted for, i.e. not included in the calculation of the energy balance, the event will look imbalanced and could therefore be misidentified as SUSY signal. The bad jet veto rejects therefore events in which jets with a transverse momentum larger than 50 GeV/c are not accepted as *good* jets.
4. H_T cut:
The total scalar momentum H_T (Sect. 4.2), shown in Fig. 4.8, is required to be larger than 350 GeV/c. The calculation is based on *good* jets. The H_T distribution before this cut is presented in Fig. 4.8.
5. Additional requirement on jet kinematics:
The required H_T is well above the minimum jet transverse momentum of 50 GeV/c. However several jets below threshold could lead to a considerable amount of neglected momentum in the event. For that reason the missing transverse energy calculated

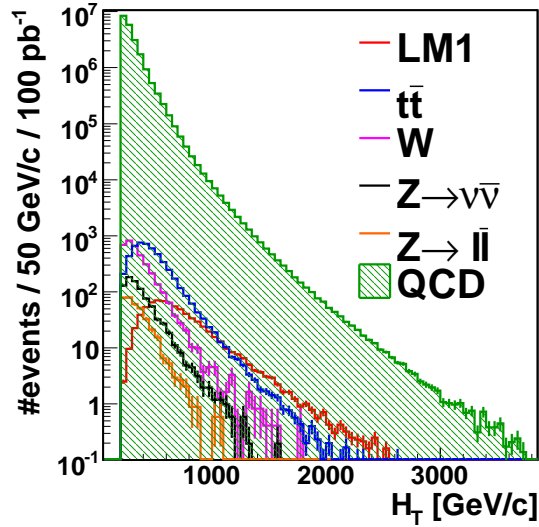


Figure 4.8: The H_T distribution after the cut on jet multiplicity for all Standard Model backgrounds and SUSY signal sample with parameter set LM1.

from all jets having a p_T larger than 30 GeV/c, $H_T^{\text{miss}}(> 30 \text{ GeV}/c)$ is compared to H_T^{miss} determined from the selected jets only. The ratio

$$R_{\text{miss}} = \frac{H_T^{\text{miss}}}{H_T^{\text{miss}}(> 30 \text{ GeV}/c)} \quad (4.5)$$

can be used to single out events where the inclusion of lower momentum jets does significantly improve the balance of the event. The ratio R_{miss} is required to be smaller than 1.25. Details about this cut can be found in Ref. [64].

The event yields after the different steps of the preselection are given in Table 4.3 for background events and in Table 4.4 for SUSY events of different parameter-sets. The preselection reduces significantly the number of events from W or Z decays. Only 80 $Z \rightarrow \ell\bar{\ell}$ events survive the preselection. In the histograms shown in the further course of this analysis $Z \rightarrow \ell\bar{\ell}$ and $Z \rightarrow \nu\bar{\nu}$ events are combined and denoted in the legend by a Z . The background from QCD multi-jet events is still three orders of magnitude larger than the number of signal events. The final event selection needs to be able to effectively suppress this background. SUSY events of the LM0 parameter-set have the highest event yields after the preselection. It will however be shown, in the further course of this analysis, that the event yields of LM1 events, after the final event selection, are comparable to those of LM0 events.

4.7 Final Variables

In this section the final selection variables are introduced. The precise cut values on these variables are determined and justified in the following sections.

Table 4.3: Number of events expected for an integrated luminosity of 100pb^{-1} after each selection cut, for background samples.

Selection cut	QCD	$W \rightarrow \nu\ell$	$t\bar{t}$	$Z \rightarrow \nu\bar{\nu}$	$Z \rightarrow \ell\bar{\ell}$	LM0
no selection	1.5×10^9	4×10^6	31.7×10^3	200×10^3	370×10^3	11 000
trigger	6.5×10^7	44.8×10^3	16.2×10^3	6 420	7 230	8 832
lepton veto	6.3×10^7	16.0×10^3	9 340	6 200	1 280	5 480
number of jets	2.1×10^7	3 200	4 690	820	330	3 770
bad jet veto	2.1×10^7	2 880	3 960	780	280	3 270
$H_T > 350 \text{ GeV}/c$	4.0×10^6	1 090	2 980	340	110	2 970
R_{miss}	3.0×10^6	880	1 800	290	80	2 530

Table 4.4: Number of SUSY events expected for an integrated luminosity of 100pb^{-1} after each selection cut, for SUSY signal samples.

Selection cut	LM0	LM1	LM2	LM3	LM4	LM5
no selection	11 000	1 610	240	1180	670	190
trigger	8 830	1 450	217	1 050	617	179
lepton veto	5 480	930	147	670	430	126
number of jets	3 770	750	123	530	360	104
bad jet veto	3 270	660	108	450	310	91
$H_T > 350 \text{ GeV}/c$	2 970	630	107	440	310	90
R_{miss}	2 530	610	103	400	290	86

A common approach to SUSY searches in events with no leptons and n jets is to apply harsh cuts on the missing transverse energy E_T^{miss} calculated from calorimeter towers [16]. For a perfectly measured QCD multijet event this quantity is expected to be zero, while escaping neutrinos or lightest stable particles lead to non-zero values. The power of E_T^{miss} to separate multijet events from SUSY events with LSP and SM background events with neutrinos is illustrated in Fig. 4.9. In this analysis an approach based on a direct cut on the missing transverse energy is compared to methods based on other selection variables, calculated from the four-vectors of *good* jets. To study the effect of systematic uncertainties due to jet energy and jet angle mismeasurements it is convenient to substitute the calorimeter based E_T^{miss} with the jet based H_T^{miss} (Sect. 4.2). Obviously E_T^{miss} and H_T^{miss} are highly correlated as visible in Fig. 4.10. However, E_T^{miss} is not always equal to H_T^{miss} . Some energy deposits in the calorimeters which are taken into account in the calculation of E_T^{miss} will not enter into H_T^{miss} , as the corresponding towers might not be picked up by the jet-reconstruction algorithm or the reconstructed jet might be rejected by the jet quality criteria (e.g. $p_T > 50 \text{ GeV}/c$).

The final selection variables are:

1. H_T^{miss} :

The variable H_T^{miss} is the reference one. In previous studies [16] it has been pointed out that a cut on the azimuthal angle between the direction of \vec{H}_T^{miss} and the three

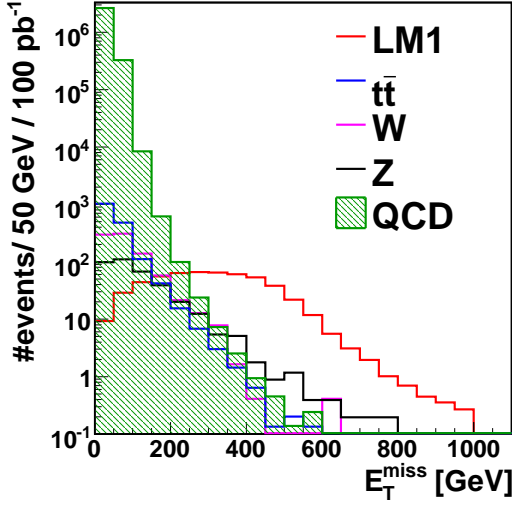


Figure 4.9: Distribution of E_T^{miss} after detector simulation and preselection.

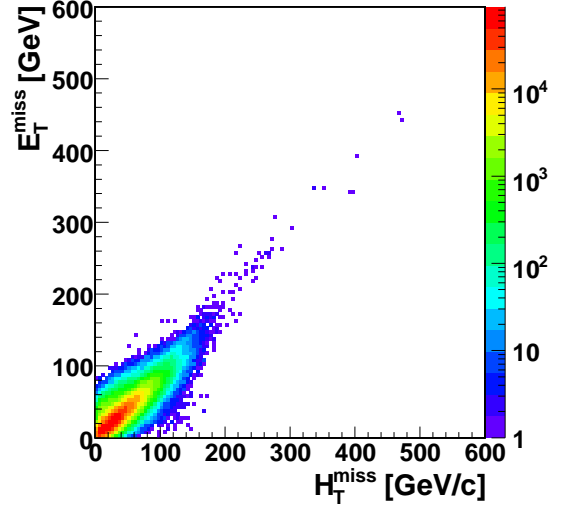


Figure 4.10: Distribution of H_T^{miss} vs. E_T^{miss} for QCD events. The distributions is shown after detector simulation and preselection.

leading jets ($\Delta\phi \geq 0.3$ rad) reduces the effect of jet energy mismeasurements on the event yields. In the course of this analysis H_T^{miss} is always used together with this $\Delta\phi$ requirement.

2. H_T^{miss}/H_T :

The variable H_T^{miss} is substituted by H_T^{miss}/H_T . Energy-scale uncertainties are expected to cancel out to a large extent in this ratio. Fig. 4.11 presents the H_T^{miss}/H_T distribution for various backgrounds and the LM1 signal sample.

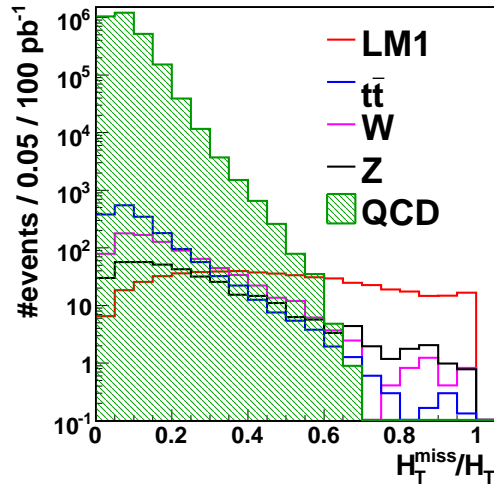


Figure 4.11: Distribution of H_T^{miss}/H_T after the detector simulation and preselection.

3. α_T :

The variable α was first suggested by L. Randall *et al.* [65] to exploit the typical

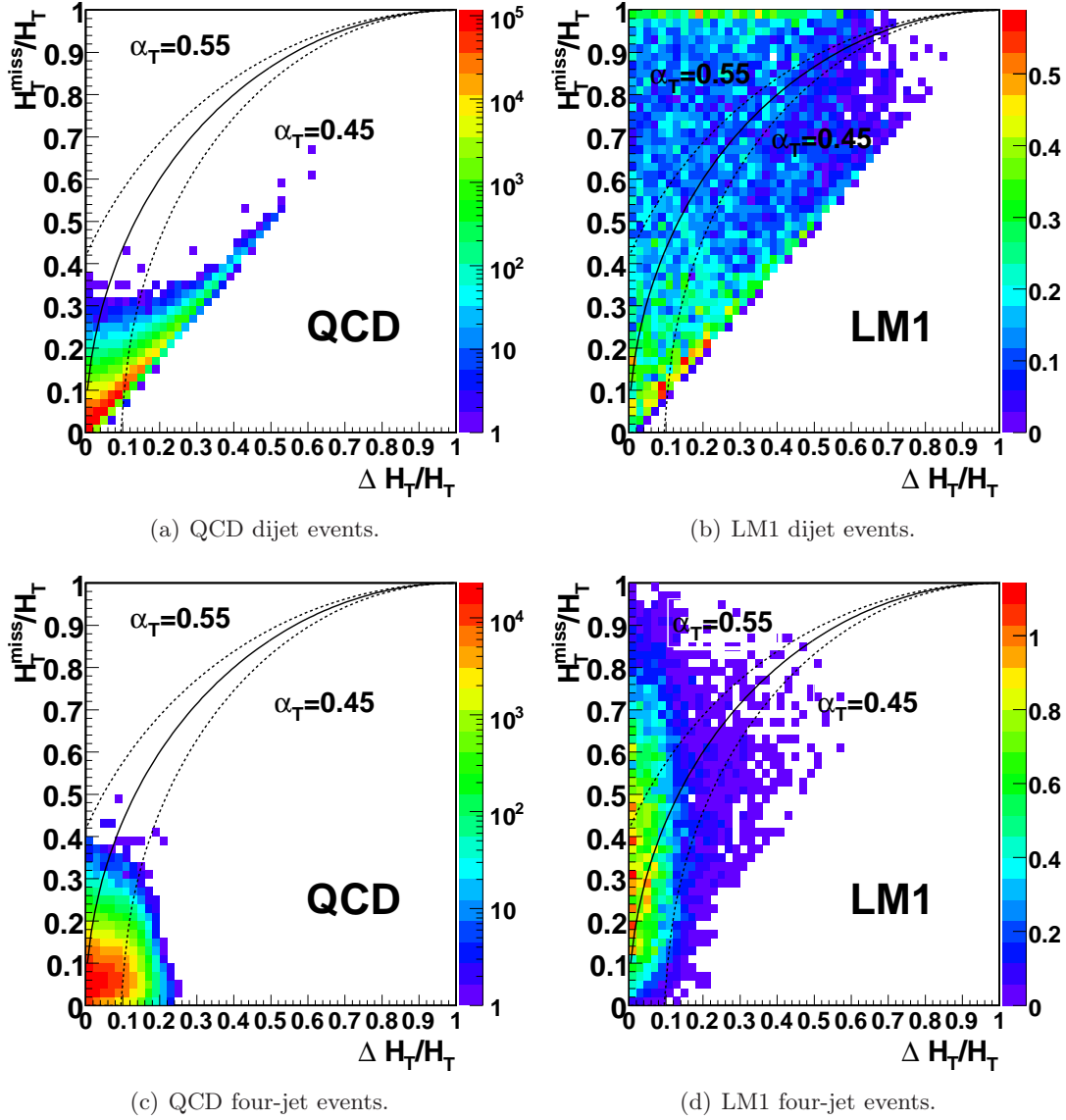


Figure 4.12: Correlation between H_T^{miss}/H_T and $\Delta H_T/H_T$ for QCD events (left) and for SUSY events at the LM1 parameter-set (right), for dijet events (top row) and for four-jet events (bottom row). The continuous line stands for $\alpha_T = 0.5$, the two dashed lines for $\alpha_T = 0.45$ and $\alpha_T = 0.55$. The number of events in the histograms correspond to the expected number of events after the preselection for an integrated luminosity of 100pb^{-1} .

topology of two back-to-back jets of equal magnitude in dijet QCD events. The definition of α in dijet events is:

$$\alpha = E_T(j_2)/M_{inv.}, \quad (4.6)$$

where $E_T(j_2)$ is the transverse energy of the jet with the lowest transverse momentum and M_{inv} is the invariant mass of the two jets. In Ref. [66] a modified version of α is explored (α_T) in which the transverse mass $M_{T,inv}$ of the two jets (j):

$$M_{T,inv} = \sqrt{\left[\sum_{i=1}^2 E_T(j_i) \right]^2 - \left(\sum_{i=1}^2 \vec{p}_t(j_i) \right)^2} \quad (4.7)$$

is used instead of the invariant mass.

The extension of α_T to searches with more than two jets is discussed in Ref. [64]. To define α_T in events with at least two jets a system of n -jets is reduced to a two-jet system by combining jets into two pseudo-jets. The transverse momentum of the pseudo-jets p_T^{pj} is calculated as the scalar sum of the contributing jets. All combinations of jets are computed and the one is chosen for which the difference $\Delta H_T = p_T^{pj1} - p_T^{pj2}$ is minimal. The variable α_T is then defined as:

$$\alpha_T = \frac{1}{2} \frac{H_T - \Delta H_T}{\sqrt{H_T^2 - (H_T^{miss})^2}} = \frac{1}{2} \frac{1 - \Delta H_T/H_T}{\sqrt{1 - (H_T^{miss}/H_T)^2}}. \quad (4.8)$$

For two jets this evaluates to:

$$\alpha_T = \frac{p_T(j_2)}{\sqrt{\left(\sum_{i=1}^2 p_T(j_i) \right)^2 - \left(\sum_{i=1}^2 \vec{p}_t(j_i) \right)^2}}, \quad (4.9)$$

which is equal to the α_T definition in Ref. [66] for massless jets.

The quantities H_T and H_T^{miss} can be unambiguously calculated for any number of jets n . It is important to note that H_T^{miss} and ΔH_T do not enter into α_T with their absolute values, but only relative to H_T and hence α_T is robust against energy scale uncertainties. Both ratios are generally small for QCD events.

For a perfectly measured QCD multijet event ($H_T^{miss} = 0$ and $\Delta H_T \approx 0$) α_T is approximately 0.5. A severe mismeasurement of jet energies will typically lead to an increase in H_T^{miss} and in ΔH_T . This is obvious in the dijet case, but less pronounced for events with more than two jets. The correlation of $\Delta H_T/H_T$ with H_T^{miss}/H_T is shown in Fig. 4.12 for QCD and SUSY LM1 events with two jets (upper row) and with four jets (lower row), respectively. The continuous black line indicates the prediction from Eq. for $\alpha_T = 0.5$, the two dashed lines for $\alpha_T = 0.45$ and $\alpha_T = 0.55$. For SUSY dijet events, there is no obvious correlation between $\Delta H_T/H_T$ and H_T^{miss}/H_T . For higher jet multiplicities, combinatorics bias ΔH_T towards smaller values. A cut on $\alpha_T < 0.55$ would reject almost all QCD background independent of the jet multiplicity. However, the SUSY signal efficiency worsens with increasing jet multiplicity. The α_T distribution is presented in Fig. 4.13. The QCD background peaks, as expected sharply at a value of 0.5.

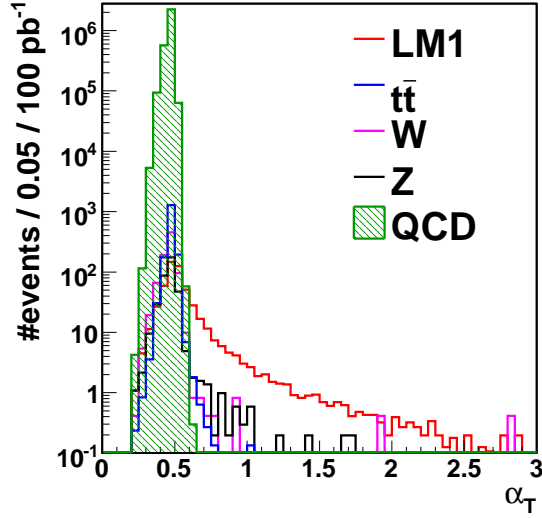


Figure 4.13: Distribution of α_T after the detector simulation and preselection.

4. $Th\Delta\Phi$:

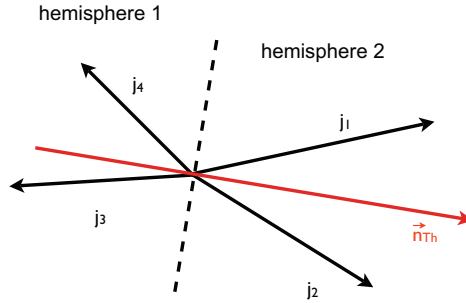


Figure 4.14: Cartoon illustrating the definition of the transverse thrust axis for a 4 jet j event. The dashed line indicates the plane which separates the two hemispheres.

The variable $Th\Delta\Phi$ is based on the global transverse thrust [67]:

$$T = \max_{\vec{n}} \frac{\sum_i |\vec{p}_{T,i} \cdot \vec{n}|}{\sum_i |\vec{p}_{T,i}|}, \quad (4.10)$$

where the numerator is maximized over the directions of the unit vector \vec{n} and the sum is taken over the \vec{p}_T of all *good* jets. The axis \vec{n} for which the maximum is obtained is called the thrust axis. Possible values of the transverse thrust are between 1 and $\geq 1/2$ in the limit of an isotropic distribution. The thrust axis is used to define two hemispheres. Jets are associated to one of the two hemispheres depending on their angles $\Delta\phi$ with respect to the thrust axis. Jets for which $\Delta\phi$ to the thrust axis is larger than 180° are attributed to hemisphere 1 jets with $\Delta\phi < 180^\circ$ to hemisphere 2. Fig. 4.14 shows a cartoon illustrating the definition of the transverse thrust axis and

the two hemispheres. The vector sum of jets can be computed for each hemisphere and therefore a value p_T and ϕ can be associated to each hemisphere. The variable $Th\Delta\Phi$ is defined as $\pi - \Delta\phi$ between the two hemispheres. For QCD events $Th\Delta\Phi$ is in average 0. For events in which neutrinos or neutralinos remove momentum the $Th\Delta\Phi$ distribution broadens as shown in Fig. 4.15. When the second hemisphere contains no jet $Th\Delta\Phi$ is set to 0. These event topologies are typical for SUSY events and background events with neutrinos in the decay chain.

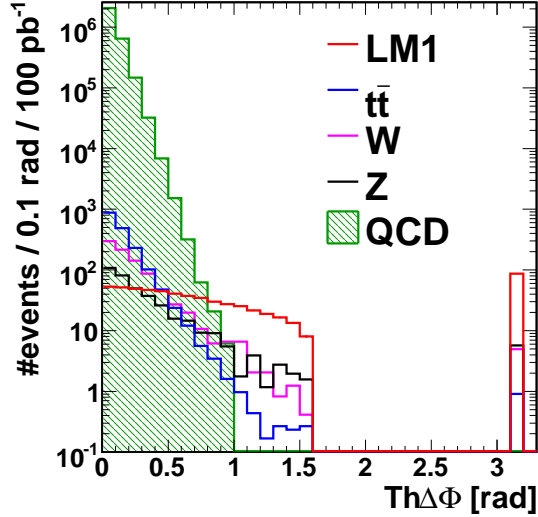
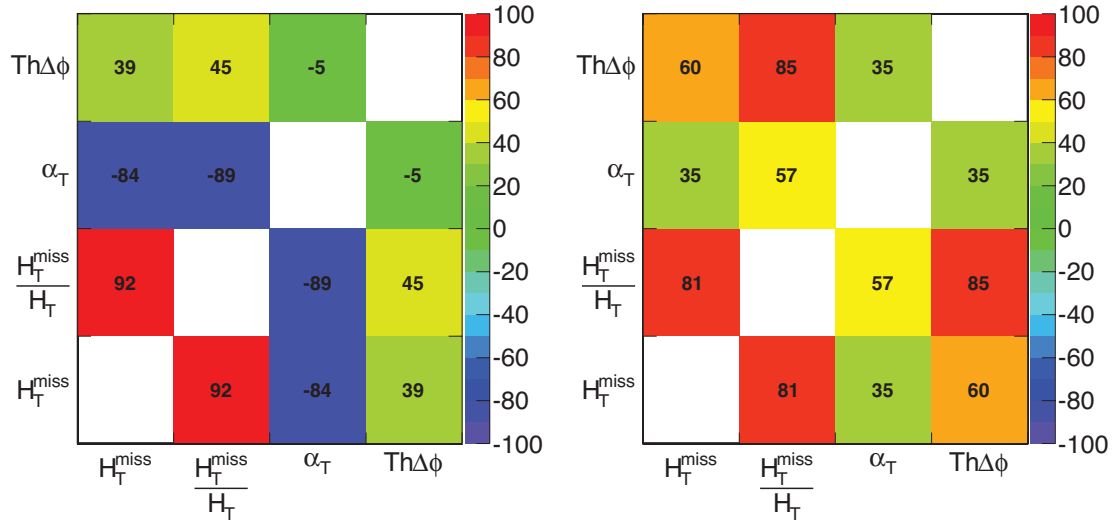


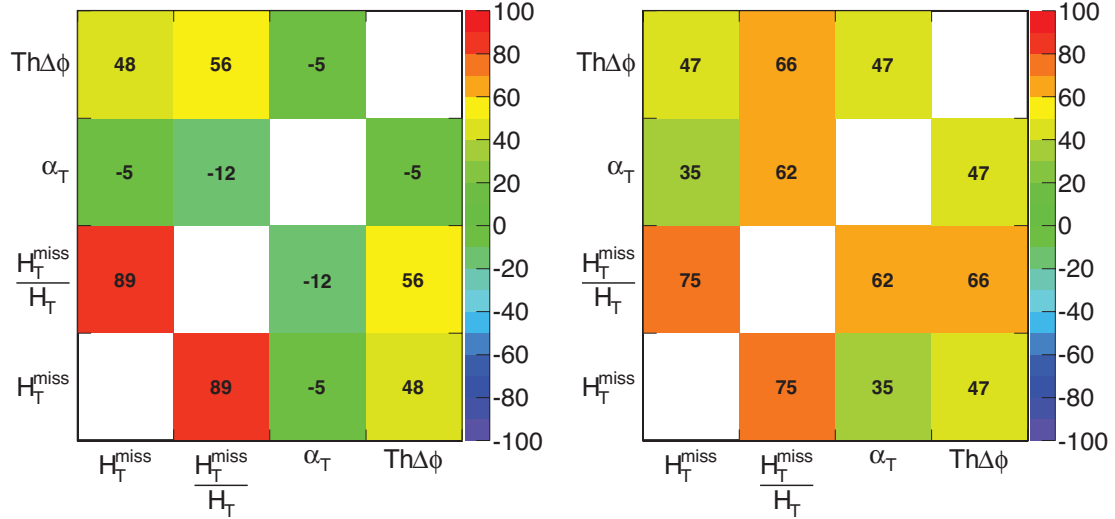
Figure 4.15: Distribution of $Th\Delta\Phi$ after detector simulation and preselection for the background processes and LM1 SUSY events.

It is interesting to study the correlation between the different variables to understand how redundant they are. The correlations are presented in Fig. 4.16, for QCD events (left) and for LM1 SUSY events (right). The upper row shows the correlation factors for dijet events, the lower row that for events with more than two jets. The variables which have the strongest correlations are H_T^{miss} , H_T^{miss}/H_T and α_T in QCD dijet events. The correlation factor between H_T^{miss} and H_T^{miss}/H_T is larger than 80% for QCD and SUSY events. The variable α_T , a function of $\Delta H_T/H_T$ and H_T^{miss}/H_T (eq. 3), is anti-correlated (correlation factor $< 80\%$) to H_T^{miss} and H_T^{miss}/H_T in QCD dijet events. The two jets ($j1$ and $j2$) in a QCD dijet event are in most cases back-to-back, this results in ΔH_T of Eq. 3 ($|p_T(j1) - p_T(j2)|$) being almost equal to H_T^{miss} ($|\vec{p}_T(j1) - \vec{p}_T(j2)|$). The anti-correlation is much weaker (an absolute correlation factor smaller than 15%) in events with more than two jets.

An important reason for the introduction of variables such as H_T^{miss}/H_T , is that energy scale uncertainties cancel out. This assumption can be verified by comparing the resolution of different variables as a function of H_T . The resolution of a variable is defined here as the RMS of the difference between the value of the variable before and after the simulation of detector effects. The variable values before detector simulation are extracted by using particle jets (Sect. 3.2.1) instead of calorimeter jets. The same requirements on jet p_T and η are applied.



(a) The correlation factors for QCD dijet events. (b) The correlation factors for LM1 SUSY dijet events.



(c) The correlation factors for QCD events with more than 2 jets. (d) The correlation factors for LM1 SUSY events with more than 2 jets.

Figure 4.16: Correlation between various selection variables.

It is well known from previous experiments like UA1 [16] that the E_T^{miss} and therefore also the H_T^{miss} resolution degrades in events with large H_T , this is visible in Fig. 4.17(a). The resolution shown in this figure is determined from QCD multijet events, all preselection cuts up to the bad jet veto have been applied. For variables which don't depend directly on the jet-energy scale the resolution improves with increasing H_T , examples are H_T^{miss}/H_T (Fig. 4.17(b)), α_T (Fig. 4.24(b)) and $Th\Delta\Phi$ (Fig. 4.24(c)).

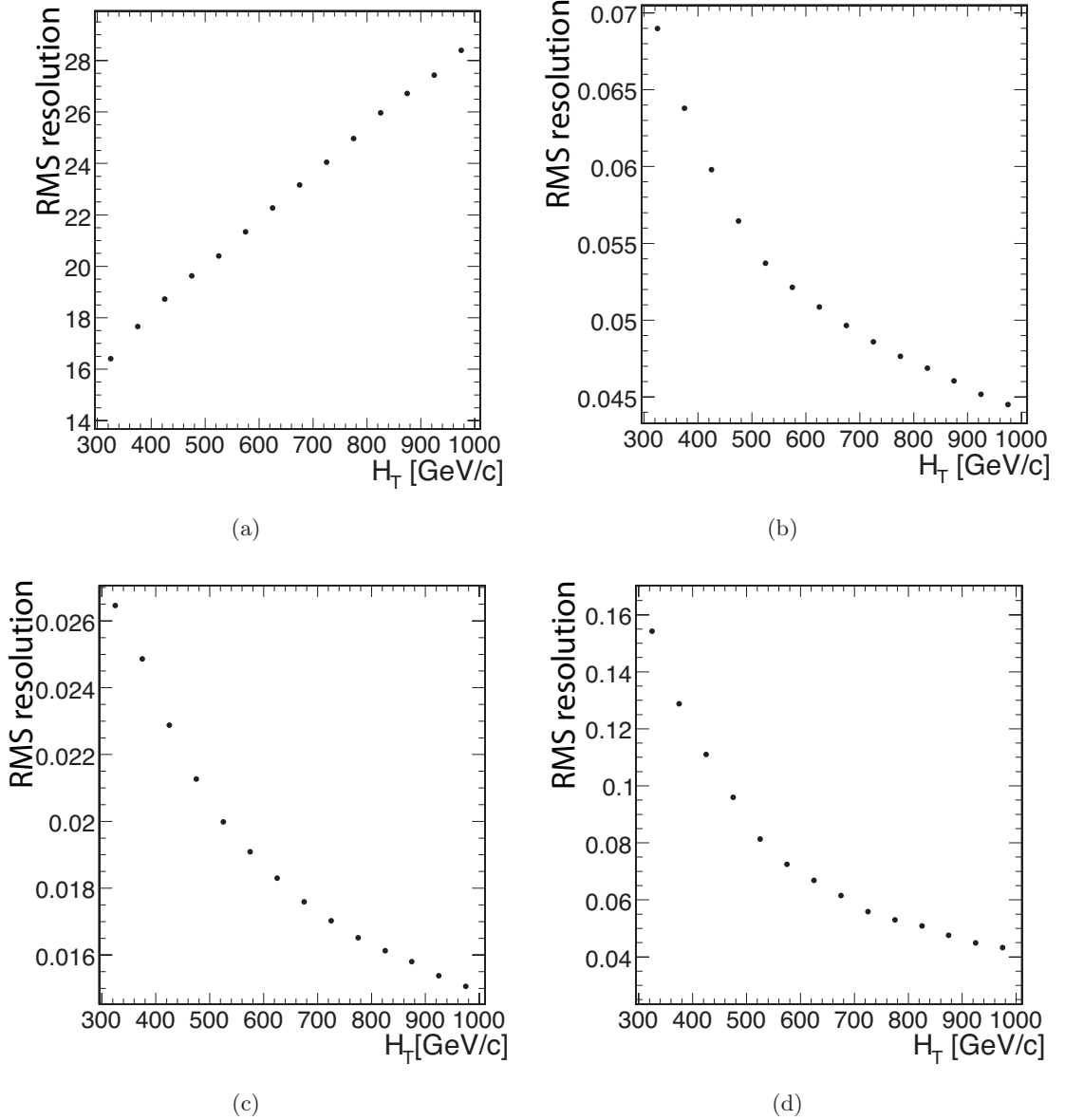


Figure 4.17: r.m.s. of the difference between H_T^{miss} (a), H_T^{miss}/H_T (b), α_T (c) and $Th\Delta\phi$ (d) before and after the simulation of detector effects as a function of H_T .

4.7.1 Dependence on Jet-Multiplicity

In this section it is pointed out how the distributions of the selection variables in SUSY events depend on the jet-multiplicity.

SUSY events can be sorted into five categories according to their production process and subsequent decay:

1. $\tilde{q}\tilde{q} \rightarrow qq + \text{invisible}$: Two squarks are pair-produced in a $2 \rightarrow 2$ process. Both decay directly into $\chi_1^0 q$. The χ_1^0 is the LSP for all SUSY parameter-sets studied here and escapes undetected.
2. $\tilde{q}\tilde{q} \rightarrow qq + \text{visible} + \text{invisible}$: The two squarks are pair-produced in a $2 \rightarrow 2$ process.
3. $\tilde{q}\tilde{g} \rightarrow qg + X$: A squark and a gluino are produced in a $2 \rightarrow 2$ process. The decays of squark and gluino are inclusive.
4. $\tilde{g}\tilde{g} \rightarrow gg + X$: Two gluinos are pair-produced in a $2 \rightarrow 2$ process. The decays of the two gluinos are inclusive.
5. other: All other production processes. These can be, e.g. processes in which two sleptons or two charginos are pair-produced in a $2 \rightarrow 2$ process.

The shape of the H_T^{miss} distribution is shown in Fig. 4.18 for the different categories. For $\tilde{q}\tilde{q} \rightarrow qq + \text{invisible}$ events the distribution exhibits a clear asymmetry. The mean is biased towards large H_T^{miss} values. The squarks in these $2 \rightarrow 2$ processes are produced almost at rest due to their large masses. Since they decay into a quark and a LSP the transverse momenta of the quark and the LSP are large and of similar magnitude. The transverse momentum of the LSP then contributes to the missing transverse energy.

The fraction of preselected events associated to each category is summarized in Table 4.5 for LM1 SUSY events. The table is split according to the number of *good* jets in the event. The relative contribution of events from $\tilde{q}\tilde{q} \rightarrow qq + \text{invisible}$ processes is largest if exactly two *good* jets are required and decreases with increasing jet-multiplicity.

Table 4.5: Relative contribution of the various processes listed in the text is shown for different jet-multiplicities, after the preselection for SUSY sample LM1.

jet-multiplicity	2	3	4	5	6
$\tilde{q}\tilde{q} \rightarrow qq + \text{invisible}$	36%	18%	10%	7%	4%
$\tilde{q}\tilde{q} \rightarrow qq + \text{visible} + \text{invisible}$	30%	22%	18%	13%	10%
$\tilde{q}\tilde{g} \rightarrow qg + X$	31%	53%	62%	62%	63%
$\tilde{g}\tilde{g} \rightarrow gg + X$	2%	5%	9%	16%	21%
other	1%	2%	1%	2%	2%

The distributions of the final selection variables are presented in Fig. 4.19 for different jet-multiplicities in LM1 SUSY events. The relative contribution of the production processes is reflected in these distributions.

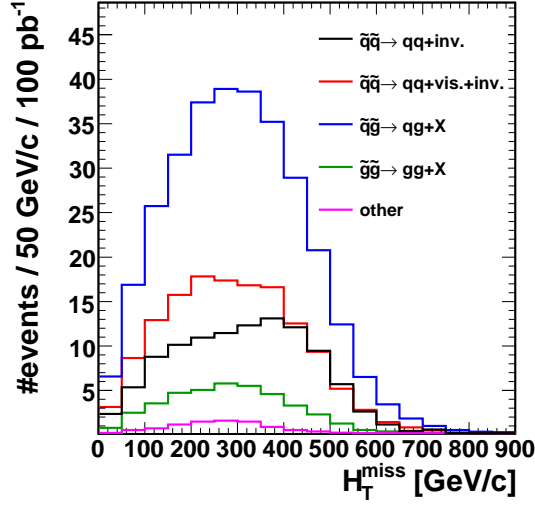


Figure 4.18: Distribution of H_T^{miss} for the different production processes in SUSY events of the LM1 sample.

- The H_T^{miss} distribution is shown in Fig. 4.19(a). In dijet events the distribution exhibits the asymmetric shape associated with $\tilde{q}\tilde{q} \rightarrow qq + \text{invisible}$ processes.
- The H_T^{miss}/H_T distribution is shown in Fig. 4.19(b). The most probable value (MPV) decreases with increasing jet-multiplicity: Every additional jet adds to the total transverse momentum and shifts the H_T^{miss}/H_T distribution to smaller values. For dijet events the distribution shows a clear peak at $H_T^{miss}/H_T = 1$. Here jets and LSP are of similar momenta and the two jets are close in ϕ .
- For α_T the situation is more complicated. The variable α_T is a function of $\Delta H_T/H_T$ and H_T^{miss}/H_T (Eq. 3) with increasing jet-multiplicity more balanced events (smaller ΔH_T) are produced, due to the larger number of combinatorial possibilities. For small values of $\Delta H_T/H_T$ the α_T distribution becomes very narrow as indicated by the dashed black lines in Figure 4.12. This narrowing of the α_T distribution with increasing jet-multiplicity is also visible in Figure 4.19(c).
- The spread of the $Th\Delta\Phi$ distribution increases with the number of jets, as more jets allow for a more randomly distributed thrust axis. In many SUSY dijet events the two jets are closer than $\pi/2$ and are therefore in the same hemisphere, $Th\Delta\Phi = \pi$. In dijet events with one jet per hemisphere the $\Delta\phi$ between the two thrust hemispheres is identical to the $\Delta\phi$ between the two jets. SUSY events in which two heavy squarks decay to two quarks and two lightest stable particle would appear as events with relatively large $Th\Delta\Phi$ due to the recoil of the lightest stable particles.

The differences between SUSY dijet events and events with more than two jets justify a separate analysis of these two cases. In the final results of this thesis dijet events and events with more than two jets are therefore treated separately.

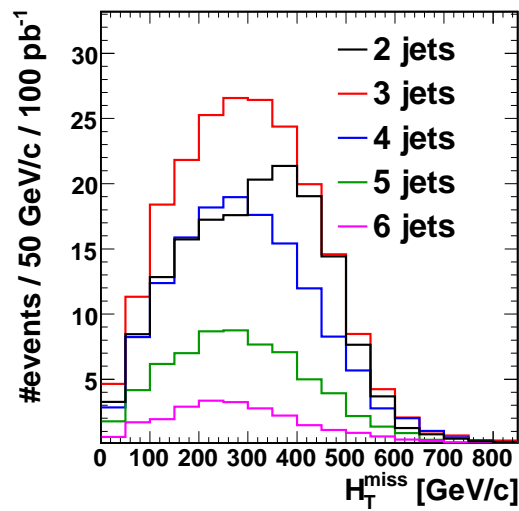
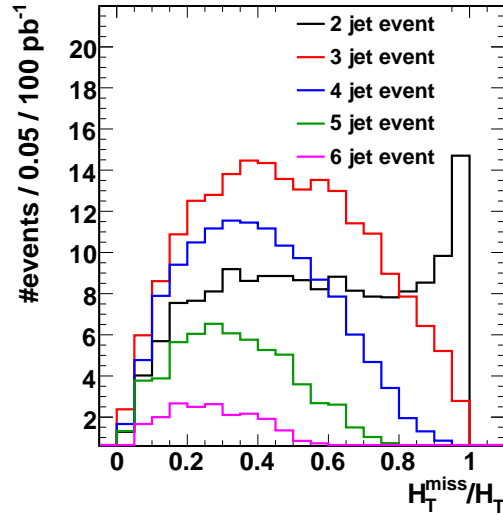
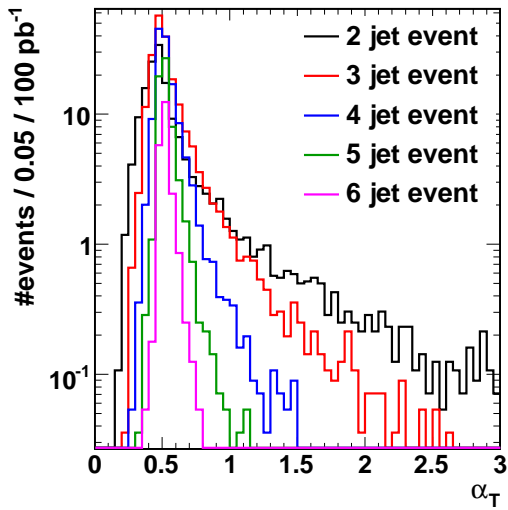
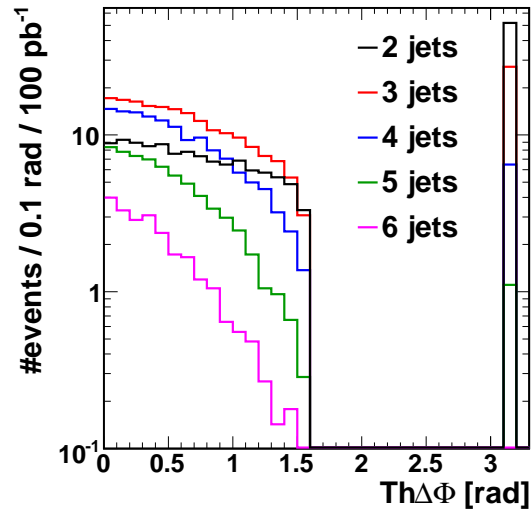

 (a) Distribution of H_T^{miss} .

 (b) Distribution of H_T^{miss}/H_T .

 (c) Distribution of α_T .

 (d) Distribution of $Th\Delta\Phi$

Figure 4.19: Dependency of the H_T^{miss} , H_T^{miss}/H_T , α_T and $Th\Delta\Phi$ distribution on the number of jets in LM1 SUSY events. The distributions are shown after the preselection.

4.8 First Method to Quantify the Statistical Significance of a Signal

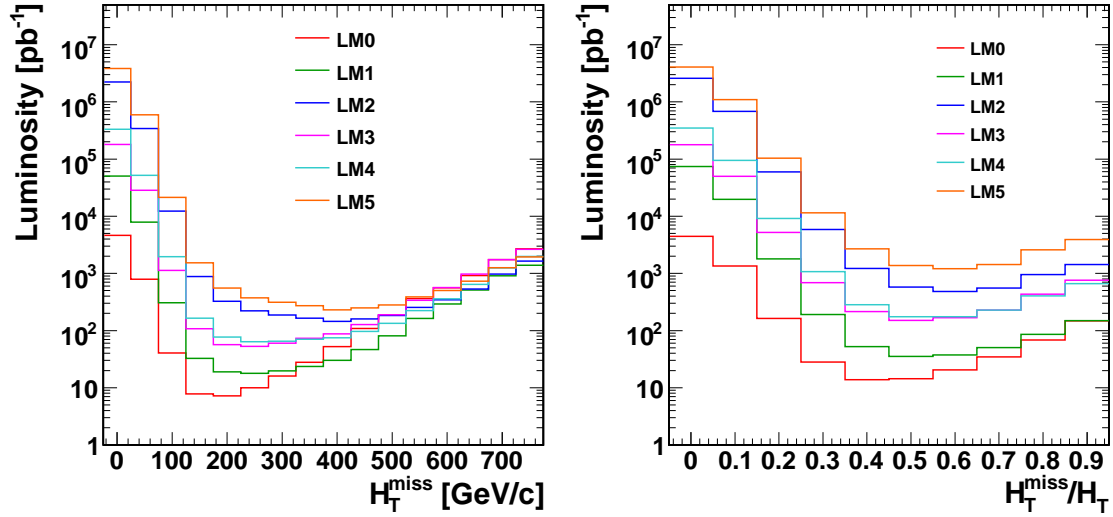
Different ways to quantify the sensitivity of a search for new phenomena are discussed in literature. In this section the minimal luminosity required for a potential 5σ discovery of SUSY events ($\mathcal{L}_{min}^{5\sigma}$) is compared for various cuts on the final selection variables. The formula for $\mathcal{L}_{min}^{5\sigma}$ as a function of the selection efficiency for signal and background events is derived in the Appendix B. The calculation is based on Ref. [68].

The luminosity $\mathcal{L}_{min}^{5\sigma}$ is presented in Fig. 4.20 as a function of the cut value for different SUSY parameter-sets. Systematic uncertainties are not included. The value of $\mathcal{L}_{min}^{5\sigma}$ depends on the SUSY parameter-set, as it determines the cross-section of the produced events and the hardness of the generated jets (Sect. 4.3). Events of the LM0 benchmark point have the largest cross-section and contain in average the softest jets compared to events of the LM1 - LM5 scenarios. The difference in mean jet momenta is reflected in the $\mathcal{L}_{min}^{5\sigma}$ distribution for the H_T^{miss} selection and different SUSY parameter-sets. The optimal cut value for events of the LM0 parameter-set is 200 GeV/c, increasing to 400 GeV/c for LM2 and LM5 events.

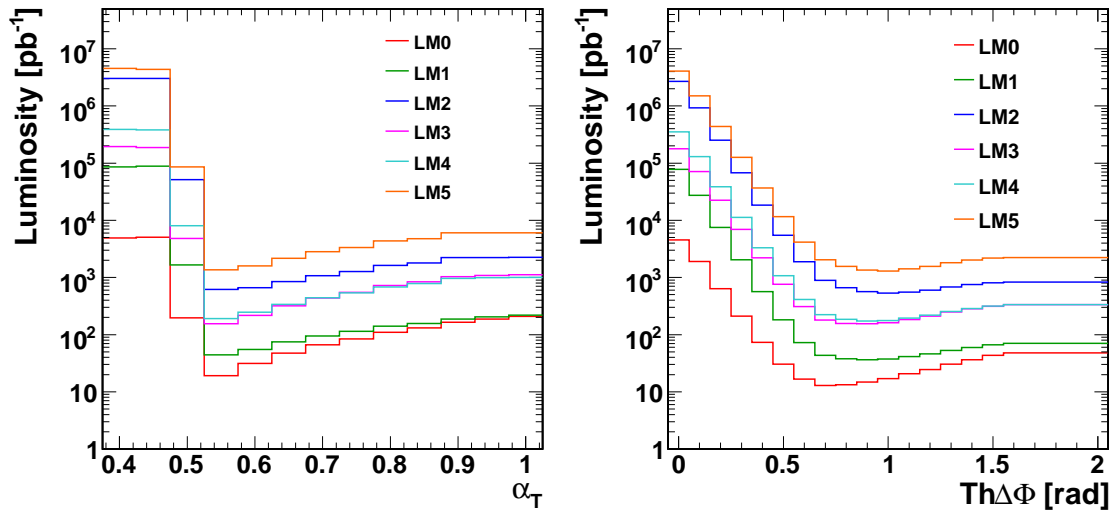
The dependence of the optimal cut value on the parameter-set is less pronounced for final selection variables which are normalized to the jet-energy scale:

- for H_T^{miss}/H_T the optimal cut value ranges from 0.4 (LM0) up to 0.6 (LM2, LM5).
- for α_T the optimal cut value is determined by the sharp edge in the α_T distribution for QCD events and the detector resolution of α_T . A dependence on the parameter-set is not observable. The luminosity $\mathcal{L}_{min}^{5\sigma}$ is smallest for a cut on $\alpha_T > 0.55$.
- for $Th\Delta\Phi$ the optimal cut value ranges from 0.7 rad (LM0) up to 1 rad (LM2, LM5).

A final decision on a set of cuts must be considered carefully, as systematic uncertainties have to be taken into account. This statement is especially true for a purely jet-based analysis such as the one presented here, due to the potentially large uncertainties on the jet reconstruction and on cross-section for QCD multi-jet events. A detailed discussion of systematic uncertainties is therefore given in the following section.



(a) Minimal required luminosity as a function of a sliding cut on H_T^{miss} . (b) Minimal required luminosity as a function of a sliding cut on H_T^{miss}/H_T .



(c) Minimal required luminosity as a function of a sliding cut on α_T . (d) Minimal required luminosity as a function of a sliding cut on $Th\Delta\Phi$.

Figure 4.20: Distribution of $\mathcal{L}_{min}^{5\sigma}$ as function of selection cuts on H_T^{miss} , H_T^{miss}/H_T , α_T and $Th\Delta\phi$. Systematic uncertainties are neglected in this histogram.

4.9 Systematic Uncertainties and Statistical Significance

Different systematic uncertainties and their effect on the statistical significance of a SUSY signal are compared in this section. The results of these studies are used to decide on a set of selection cuts.

Systematic uncertainties which might affect this search have to be analyzed in detail once the detector performance is well known with real data. Here I present estimates of possible systematic biases based on simulation.

Associated with the production rate are:

- uncertainties on the parton density functions and effects of higher order corrections on the cross-sections. These uncertainties affect the absolute cross-section of a process and its differential cross-section as a function of e.g. jet p_T .
- the uncertainty on the precise LHC luminosity

Associated with the CMS detector performance (hardware/software):

- uncertainties on trigger efficiencies,
- jet reconstruction uncertainties,
- lepton reconstruction uncertainties.

Cross-sections will be estimated from first data at the LHC. For a center-of-mass energy of 10 TeV the total cross-section of:

- QCD multijet events should be known with $\approx 100\%$ uncertainty once 10 pb^{-1} of integrated luminosity have been accumulated [69],
- $t\bar{t}$ events should be known with $\approx 30\%$ uncertainty at about $\mathcal{L} = 20 \text{ pb}^{-1}$ [70],
- W and γ/Z events should be known with $\approx 11\%$ uncertainty at $\mathcal{L} = 10 \text{ pb}^{-1}$ [71].

More luminosity might be needed to get the correct shape of distributions such as the jet p_T distribution. In Ref. [48, 72] the predicted jet E_T spectra in $W \rightarrow \ell\nu$ events have been compared for several event generators but no detector simulation was applied. The relative uncertainty $\Delta p_T/p_T$ on high momentum jets derived from this study is approximately 10% (Fig. 4.21). Likewise I will assume 10% uncertainty for all processes studied here.

A Matrix Element (Sect. 3.1) treatment of the initial state radiation on the differential SUSY cross-sections is discussed in Ref [49]. This treatment is in general more accurate and predictive than parton showers alone and can affect the tail of the jet p_T and the H_T distributions. To identify the nature of new physics these corrections will become important.

The uncertainty on the exact luminosity during the initial years of data taking is estimated to be 5% [16]. The systematic errors on the single jet trigger efficiency (Sect. 4.4) for events with two jets each with $p_T > 100 \text{ GeV}/c$ and $H_T > 350 \text{ GeV}/c$ are negligible.

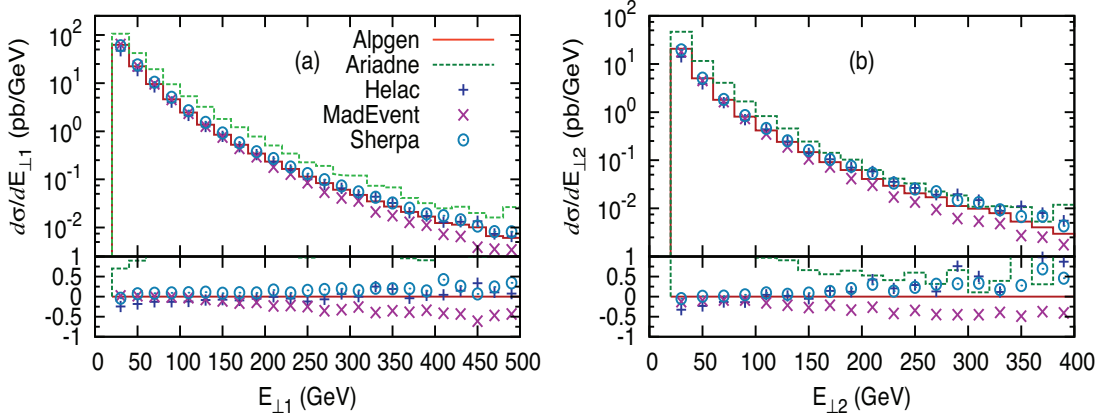


Figure 4.21: Inclusive E_T spectra of the two leading jets in $W \rightarrow \ell\nu$ events at generator level, as predicted by various event generators. The small plots on the bottom show the relative difference with respect to the ALPGEN result [48].

The uncertainties on electron [73] and muon inefficiencies [74] are expected to be small [22] and should be negligible compared to the jet-reconstruction and differential cross-section uncertainties.

The distribution of the relative error on the reconstructed jet momentum $\Delta p_T/p_T$ (Fig. 4.7) can be divided into two parts, a gaussian core and non-gaussian tails. Two different kinds of uncertainties are therefore considered in this thesis, an uncertainty on the mean and the width of this gaussian and an uncertainty on the tails.

The width of the gaussian core of the $\Delta p_T/p_T$ distribution can be estimated from data, using back-to-back dijet events [75]. Also the jet reconstruction efficiency can be extracted from data, using $Z \rightarrow \mu\mu$ events [75].

4.9.1 Choice of Final Selection Cuts

The final cuts are chosen to:

- yield a high signal significance for the two SUSY parameter-sets closest to the Tevatron exclusion limits (LM0 and LM1), thus allowing a rapid discovery or an extension of the present exclusion limits,
- but also to yield high signal significances for the other SUSY parameter-sets, and to
- be robust against systematic uncertainties.

The uncertainties taken into account are experimental ones that affect the jet ϕ distribution and the gaussian core of the $\Delta p_T/p_T$ distribution and theoretical ones on precise jet energies.

The experimental uncertainties due to mismeasurement of jet energies are estimated by applying the following performance degradations [64]:

- a gaussian smearing of the transverse jet momenta by 10%
- a gaussian smearing of the azimuthal angle ϕ by 0.1 rad
- +5% energy scaling.

A negative energy scaling has not been applied, as its effects have been found to be negligible compared to those of the gaussian smearing and the upward scaling. These variations reflect a possible imperfect simulation of the detector and uncertainties in the jet calibrations.

Each variation increases the total number of background events. The study presented in Sect. 4.8 is repeated. The number of background events after final event selection (B) in Eq. B.5 is replaced by $B + \Delta B$. The total uncertainty on the background ΔB is calculated as:

$$\Delta B = \sqrt{\sum_{i=1}^3 (\Delta B_i)^2}, \quad (4.11)$$

assuming that the systematic uncertainties are uncorrelated. ΔB_i is the change in the number of background events for each of the systematic variations. The degradations increase the optimal cut-values, as visible in Fig. 4.22. The optimal cut-values for SUSY LM0 events increase from 200 GeV/c to 250 GeV/c for an H_T^{miss} selection, from 0.4 to 0.5 for a selection on H_T^{miss}/H_T , and from 0.7 to 0.9 rad for a selection on $Th\Delta\Phi$. The values have been increased for all variables except of α_T .

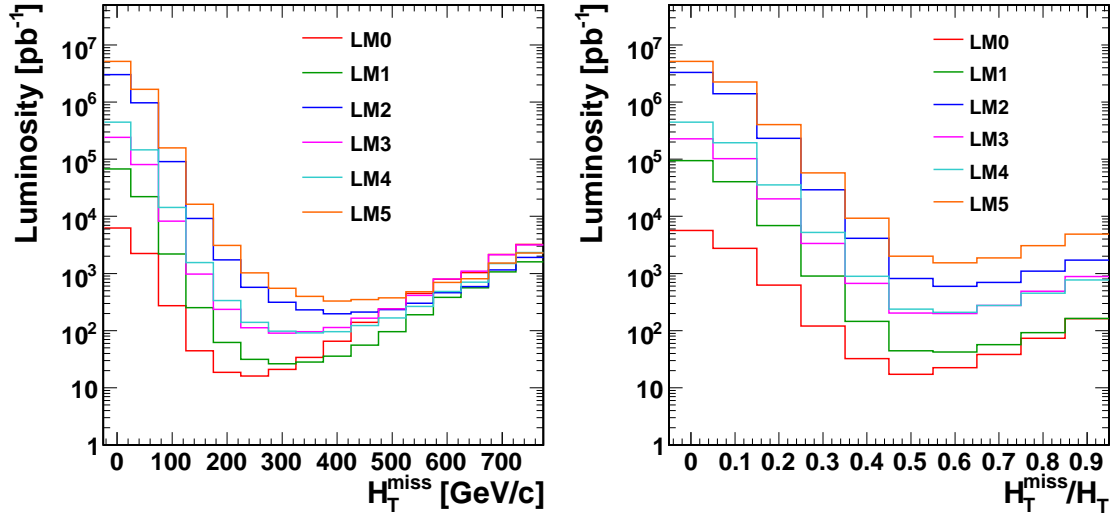
In addition to the experimental uncertainties the theoretical uncertainties on the jet-kinematics have been taken into account. It has been found that the effect of a decrease in jet energy on B is negligible compared to that of an increase. For a conservative estimate of the jet p_T is increased by 10% for all background processes. The resulting $\mathcal{L}_{min}^{5\sigma}$ are shown in Fig. 4.23. In contrast to the other variables α_T is more affected by the theoretical uncertainty rather than by the experimental performance degradations. The optimal cut-value on α_T increases from 0.55 to 0.6.

In the further course of this analysis four different event selection paths are compared. Each of these paths consists of the preselection discussed in Sect. 4.6 and one of the following selections:

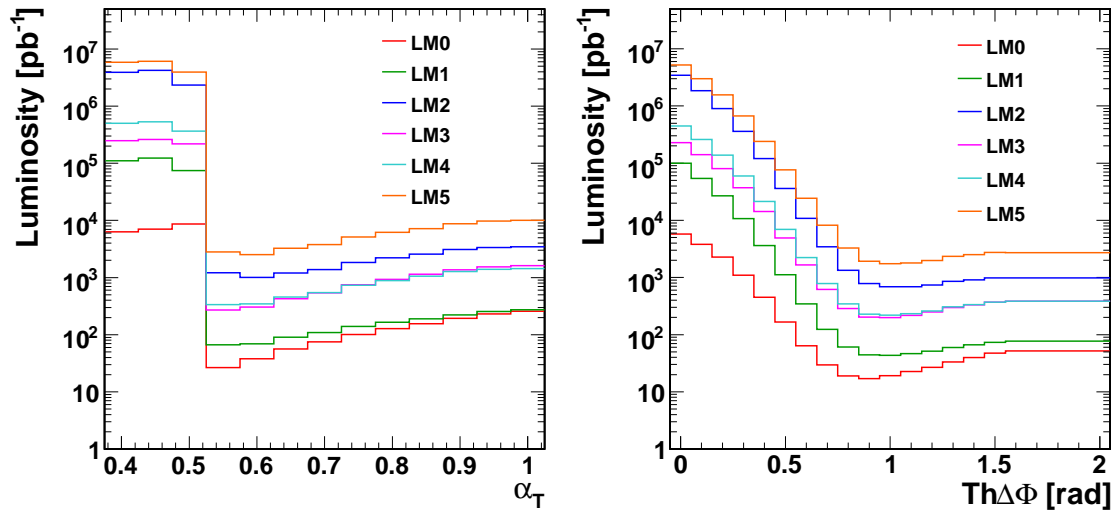
- $H_T^{miss} > 250$ GeV/c and $\Delta\phi(j_{1,2,3}, H_T^{miss}) > 0.3$ rad ²
- $H_T^{miss}/H_T > 0.5$
- $\alpha_T > 0.6$
- $Th\Delta\Phi > 1$ rad

The cuts will be optimized with collision data.

²The azimuthal angle $\Delta\phi$ between \vec{H}_T^{miss} and each of the three leading jets should be larger than 0.3 rad (Sect. 4.7).

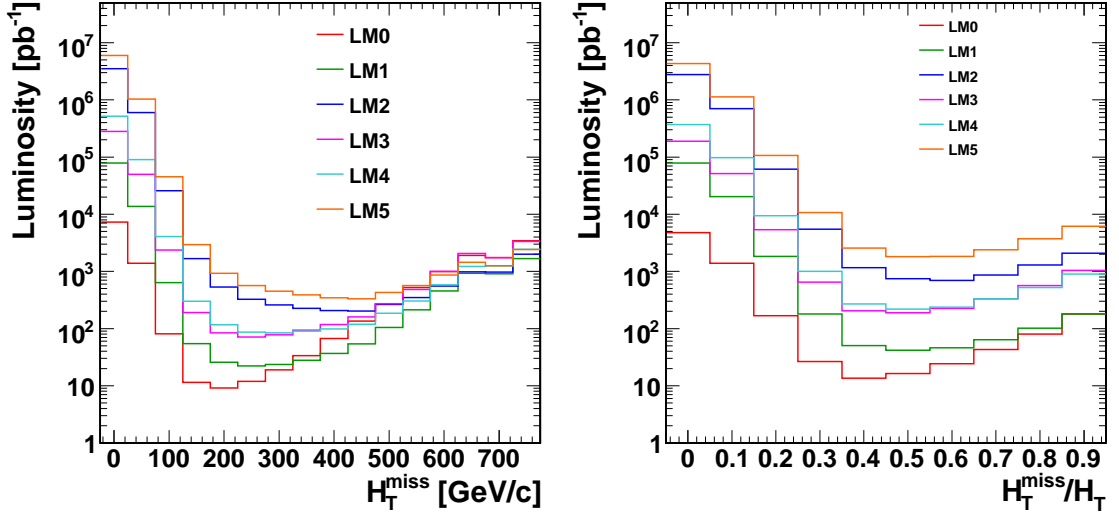


(a) Minimal required luminosity as a function of a sliding cut on H_T^{miss} . (b) Minimal required luminosity as a function of a sliding cut on H_T^{miss}/H_T .

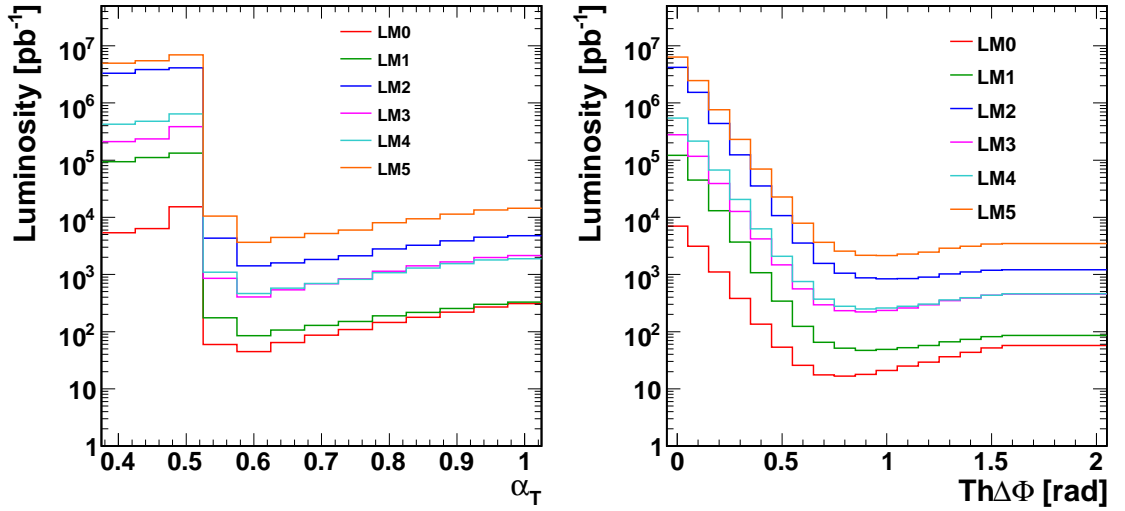


(c) Minimal required luminosity as a function of a sliding cut on α_T . (d) Minimal required luminosity as a function of a sliding cut on $Th\Delta\Phi$.

Figure 4.22: Distribution of $\mathcal{L}_{min}^{5\sigma}$ as function of selection cuts on H_T^{miss} , H_T^{miss}/H_T , α_T and $Th\Delta\Phi$ including systematic uncertainties due to detector imperfections as described in the text.



(a) Minimal required luminosity as a function of a sliding cut on H_T^{miss} . (b) Minimal required luminosity as a function of a sliding cut on H_T^{miss}/H_T .



(c) Minimal required luminosity as a function of a sliding cut on α_T . (d) Minimal required luminosity as a function of a sliding cut on $Th\Delta\Phi$.

Figure 4.23: Distribution of $\mathcal{L}_{min}^{5\sigma}$ as function of selection cuts on H_T^{miss} , H_T^{miss}/H_T , α_T and $Th\Delta\Phi$ including 10% theoretical uncertainty on the jet energy scale.

4.9.2 Uncertainties on Event Yields

In this section the effect of jet reconstruction uncertainties on the event yields is discussed in detail. The uncertainties are those of the jet p_T and ϕ resolution, introduced in the previous section. In addition possible uncertainties on the tails of the $\Delta p_T/p_T$ distribution have been studied. The tails of this distribution correspond to drastic jet momentum mis-measurements which occur only with a very small frequency.

The QCD multijet background is most affected by jet reconstruction uncertainties. The number of selected QCD events are listed in Table 4.6 for the initial case, for smeared jet p_T and ϕ , and for $\pm 5\%$ of jet-energy scaling. For the H_T^{miss} selection two numbers are stated, first the event yields of a combined selection on $H_T^{miss} > 250$ GeV/c and $\Delta\phi(j_{1,2,3}, H_T^{miss}) > 0.3$ rad, second the number of selected events without the $\Delta\phi$ requirement in parenthesis. The statistical errors correspond to the number of events in the simulated samples. When at most one event survives the selection the error is the upper limit for the mean of a Poisson variable for confidence levels of 68%. A full list of the event yields for all background processes and each of the variations can be found in the Appendix Table B.1.

Table 4.6: Remaining number of QCD events for an integrated luminosity of 100 pb^{-1} after the four different selection paths. The numbers in parenthesis are the event yields of the H_T^{miss} selection without the $\Delta\phi(j_{1,2,3}, H_T^{miss}) > 0.3$ rad requirement.

systematic variation	$H_T^{miss} > 250 \text{ GeV}/c$	$H_T^{miss}/H_T > 0.5$	$\alpha_T > 0.6$	$Th\Delta\Phi > 1 \text{ rad}$
no variation	12 ± 3 (71)	28 ± 5	1 ± 1	$0 + 1$
10 % gaussian p_T smearing	67 ± 5 (485)	61 ± 7	$0 + 1$	3 ± 2
0.1 rad gaussian ϕ smearing	174 ± 6 (228)	37 ± 6	$0 + 1$	5 ± 2
+5 % energy scale	19 ± 4 (100)	43 ± 6	2 ± 1	1_{-1}^{+2}
-5 % energy scale	11 ± 3 (57)	30 ± 5	$0 + 1$	$0 + 1$

The number of remaining QCD events increases in the worst case by more than a factor of 10 (final selection variable H_T^{miss} and a variation of ϕ). The sensitivity of the event yields to systematic variations depends on the selection path:

- Combined selection on $H_T^{miss} > 250 \text{ GeV}/c$ and $\Delta\phi(j_{1,2,3}, H_T^{miss}) > 0.3$ rad:
The largest background increase for a combined selection on H_T^{miss} and $\Delta\phi$ is observed if the jet p_T or ϕ are smeared. Without $\Delta\phi$ requirement the effect is even more drastic, in this case a 10% p_T smearing increases the number of selected QCD events by a factor of 6. A smearing of the jet direction decreases the efficiency of the $\Delta\phi$ cut and leads to the observed change in the QCD multijet event yield.
- H_T^{miss}/H_T selection:
The largest increase in QCD background is found if the p_T of the jets is smeared. The effect of a ϕ smearing is less drastic than for the H_T^{miss} selection path.
- α_T selection:
No large effect on the QCD event yield (always below 5 events) is found. The largest

impact is observed when the energy scale is increased by 5%, which effectively lowers the H_T cut.

- $Th\Delta\Phi$ selection:

As for the α_T selection no large effect on the QCD event number is found.

The robustness of the different event selections against mis-measurements of the jet energy by more than a factor of two has been tested by applying scaling factors with a given probability per jet in random sequence. This allows multiple mis-measurements to occur in a single event. Table 4.7 shows the number of selected QCD events for different scaling factors and a mis-measurement probability of 10^{-3} per jet.

Table 4.7: Number of surviving QCD events as a function of the jet energy scaling factor for different selection paths and an integrated luminosity of 100 pb^{-1} . For the H_T^{miss} selection the number of selected events without the $\Delta\phi(j_{1,2,3}, H_T^{miss}) > 0.3$ rad requirement are written in parenthesis. The assumed mis-measurement probability is 10^{-3} per jet. The statistical uncertainties correspond to the number of events in the simulated samples.

scaling factor	$H_T^{miss} > 250 \text{ GeV}/c$	$H_T^{miss}/H_T > 0.5$	$\alpha_T > 0.6$	$Th\Delta\Phi > 1 \text{ rad}$
no scaling	12±3 (71)	28±5	1±1	0+1
0.3	23±4 (228)	188±9	3+2	6±2
0.5	14±4 (110)	35±6	1±1	0+1
2	457±17 (1 845)	522±24	1±1	2±2
3	5 794±73 (22 186)	18 287±115	4+2	51+8

Whereas the event yields of the α_T , H_T^{miss} and $Th\Delta\Phi$ selection are all relatively stable against downward scaling, the effect of upward scaling is dramatic when H_T^{miss} or H_T^{miss}/H_T are used as selection variables. A scaling factor of 3 would e.g. increase the number of QCD events which pass the H_T^{miss}/H_T selection by three orders of magnitude.

A mis-measurement rate of 10^{-3} per jet could be detected with a modest amount of data, e.g. by analyzing the relative jet p_T in back-to-back dijet events [75]. The variation of the QCD event yields for different scaling factors are indicative of the tolerable mis-measurement frequency.

In Appendix B an outline is given how additional control variables, such as the cut on $\Delta\phi(j_{1,2,3}, H_T^{miss}) > 0.3$ rad, can be used for further background rejection.

4.9.3 Conclusion

Of the four different selection paths the one using α_T is the most robust against systematic variations of the jet p_T and ϕ spectrum. The H_T^{miss} selection is robust against downward scaling of the jet-energy but is heavily affected by upward scaling or by the uncertainty on the ϕ direction.

The minimal luminosity required for a potential 5σ discovery of SUSY events $\mathcal{L}_{min}^{5\sigma}$ (Sect. 4.8) is presented in Table 4.8 for different SUSY parameter-sets. The first error corresponds

to the increase in $\mathcal{L}_{min}^{5\sigma}$ due to experimental uncertainties on the jet reconstruction (Sect. 4.9.1). These uncertainties have again been estimated by a gaussian smearing of the jet p_T by 10% and of the jet ϕ direction by 0.1 rad and an increase of the jet energy by 5%. Like in Sect. 4.9.1 these performance degradations have been applied separately and Eq. 4.11 has been used to calculate the total uncertainty on the number of background events. The second error corresponds to the variation in $\mathcal{L}_{min}^{5\sigma}$ due to the MC uncertainty on the jet p_T spectrum. This uncertainty is estimated by increasing the jet p_T by 10% for all background processes (Sect. 4.9.1).

Assuming that systematic errors can be neglected the smallest $\mathcal{L}_{min}^{5\sigma}$ is achieved when H_T^{miss} is used as final selection variable. On the other hand, if systematic variations are taken into account other variables show, at least for dijet events, similar or better performances. A cut on $Th\Delta\Phi > 1$ rad yields the smallest $\mathcal{L}_{min}^{5\sigma}$ for dijet events.

For events with more than two jets the smallest $\mathcal{L}_{min}^{5\sigma}$ is achieved when H_T^{miss} is used as final event selection variable. However, the variables H_T^{miss} and H_T^{miss}/H_T are far more affected by an over-estimation of the jet-energy, even if this happens only with a very small probability. The variable $Th\Delta\Phi$ or again α_T might be the more trustworthy choice for early data analysis.

Table 4.8: Minimal luminosity required for a potential 5σ discovery of SUSY events $\mathcal{L}_{min}^{5\sigma}$ [pb $^{-1}$] in dijet events and in events with more than two jets for different SUSY parameter-sets. The luminosity is given for the four different event selections. The first error corresponds to experimental uncertainties on the mean jet p_T and ϕ resolution, the second to uncertainties on the theoretical prediction of the jet energy (Sect. 4.9.1).

SUSY	#jets	$H_T^{miss} > 250$ GeV/c	$H_T^{miss}/H_T > 0.5$	$\alpha_T > 0.6$	$Th\Delta\Phi > 1$
LM0	2	$50 + 37_{-10}^{+13}$	$61 + 20_{-11}^{+22}$	$120 + 10_{-31}^{+31}$	$54 + 7_{-8}^{+15}$
	>2	$12 + 7_{-1}^{+2}$	$19 + 2_{-3}^{+4}$	$44 + 9_{-8}^{+24}$	$25 + 3_{-2}^{+5}$
LM1	2	$71 + 61_{-17}^{+20}$	$112 + 43_{-23}^{+49}$	$153 + 14_{-42}^{+44}$	$86 + 13_{-15}^{+28}$
	>2	$25 + 19_{-4}^{+6}$	$54 + 9_{-10}^{+17}$	$89 + 24_{-21}^{+65}$	$67 + 11_{-9}^{+18}$
LM2	2	$996 + 1646_{-403}^{+526}$	$2313 + 1440_{-736}^{+1636}$	$2056 + 385_{-1022}^{+1239}$	$1360 + 404_{-434}^{+877}$
	>2	$289 + 461_{-88}^{+131}$	$760 + 219_{-238}^{+403}$	$1027 + 568_{-426}^{+1577}$	$882 + 268_{-205}^{+456}$
LM3	2	$459 + 658_{-165}^{+211}$	$897 + 506_{-260}^{+574}$	$885 + 138_{-378}^{+440}$	$587 + 150_{-164}^{+325}$
	>2	$57 + 59_{-12}^{+17}$	$168 + 38_{-42}^{+69}$	$292 + 119_{-94}^{+323}$	$218 + 49_{-39}^{+84}$
LM4	2	$404 + 564_{-142}^{+182}$	$784 + 434_{-224}^{+493}$	$815 + 125_{-343}^{+397}$	$506 + 126_{-138}^{+271}$
	>2	$73 + 82_{-17}^{+24}$	$213 + 50_{-56}^{+92}$	$359 + 155_{-121}^{+423}$	$273 + 65_{-51}^{+111}$
LM5	2	$3171 + 6071_{-1454}^{+1928}$	$7927 + 5356_{-2724}^{+6085}$	$6078 + 1355_{-3485}^{+4385}$	$4339 + 1489_{-1579}^{+3239}$
	>2	$391 + 661_{-124}^{+187}$	$1484 + 460_{-498}^{+849}$	$2148 + 1354_{-993}^{+3785}$	$1836 + 621_{-471}^{+1066}$

4.10 Background and Signal Composition after the Event Selection

In the previous section sets of cuts have been chosen based on the signal sensitivity. Systematic uncertainties have been taken into account. In this section the composition of the SM background after the selection and the event yields for different SUSY parameter-sets are studied in greater detail.

In particular, for the $W + \text{jet}$ and $t\bar{t}$ background, it is interesting to take a closer look at the final states. Table 4.9 shows the decomposition of the $t\bar{t}$ and $W \rightarrow \nu\ell$ events after the selection cuts discussed in Sect. 4.9.1 into different final states.

Table 4.9: Decomposition of $t\bar{t}$ events (a) and $W \rightarrow \ell\nu$ events (b) into various final states, for each of the four different event selections. The fraction of remaining events is given in percent.

(a)					
Selection Path	semi-leptonic			leptonic	hadronic
	μ	e	τ		
$H_T^{miss} > 250 \text{ GeV}/c$	(19±2)%	(7±1)%	(61±4)%	(9±2)%	(4±1)%
$H_T^{miss}/H_T > 0.5$	(16±2)%	(8±1)%	(65±4)%	(7±1)%	(4±1)%
$\alpha_T > 0.6$	(15±4)%	(6±2)%	(67±8)%	(7±3)%	(6±2)%
$Th\Delta\Phi > 1 \text{ rad}$	(13±4)%	(9±3)%	(59±8)%	(14±4)%	(4±2)%
(b)					
Selection Path ($t\bar{t}$)	$W \rightarrow \mu\nu$	$W \rightarrow e\nu$	$W \rightarrow \tau\nu$	$W \rightarrow \tau\nu$ hadronic τ decays	
$H_T^{miss} > 250 \text{ GeV}/c$	(22±6)%	(7±4)%	(69±11)%	(69±6)%	
$H_T^{miss}/H_T > 0.5$	(18±5)%	(6±3)%	(68±9)%	(69±5)%	
$\alpha_T > 0.6$	(27±13)%	(7 $^{+9}_{-7}$)%	(67±21)%	(71±10)%	
$Th\Delta\phi > 1 \text{ rad}$	(23±7)%	(3±3)%	(66±12)%	(72±11)%	

The background composition is similar for the various selection paths. For the $t\bar{t}$ background $\sim 90\%$ of the contribution consists of semi-leptonic t -decays of which $\sim 65\%$ stem from $W \rightarrow \tau\nu$ decays. In other words, the vast majority of the top background stems from τ 's identified as jets, or from electrons and muons which are not identified (mainly out of acceptance) or have such low- p_T that they are not rejected by the lepton veto of 10 GeV/c. Similar considerations are valid for the $W + \text{jets}$ background. Here $\sim 70\%$ of the selected events stem from $W \rightarrow \tau\nu$ decays for which the τ decays mainly hadronically.

The expected event yields for SM background and LM0 SUSY signals are summarized in Table 4.10. All yields correspond to an integrated luminosity of 100 pb $^{-1}$. Three different types of errors are given in this table. The first is the statistical uncertainty which corresponds to the number of events in the simulated samples. As before, in case that at most one event is selected the error corresponds to the upper limit for the mean of a Poisson variable for confidence levels of 68%. The second error is due to the experimental uncertainties on the mean p_T and ϕ resolutions. The third error is due to the theoretical

uncertainty on the jet energy. The estimation of these last two errors has been discussed in Sect. 4.9.1. The number of $Z \rightarrow \ell\bar{\ell}$ events is negligible for every selection path.

Some features are common to all selection paths and jet-multiplicities:

- The contribution of $Z \rightarrow \ell\bar{\ell}$ events after the selection is negligible.
- A similar amount of $Z \rightarrow \nu\bar{\nu}$ and $W \rightarrow \nu\ell$ events survive the selection.

The contribution of $t\bar{t}$ events is strongly dependent on the number of jets in the events. For dijet events this contribution is always negligible while becoming dominant with increasing jet-multiplicity. The H_T^{miss}/H_T path is the only selection for which the QCD event yields are larger in dijet events than in events with more than two jets. The effect of a single jet energy mis-measurement on H_T^{miss}/H_T becomes smaller with increasing jet multiplicity.

The knowledge on background composition can be used, either to further diminish the background e.g. by applying a τ -veto, or to estimate its contribution from data. An example of how background containing τ -leptons could be estimated from data is explained in Ref. [76]. The $Z \rightarrow \nu\bar{\nu}$ background could be estimated either by using $Z \rightarrow \mu\bar{\mu}$ or $W \rightarrow \mu\nu$ or γ +jet events [77].

The events yields for the SUSY parameter-sets LM0 - LM5 can be found in Table 4.11. Only the statistical uncertainties are given in this case. Events of the LM0 parameter-set have the largest and LM1 SUSY events the second-largest event yields, independent of the selection paths. The difference between the event yields of the LM0 and the LM1 parameter-set is approximately 3/2 for dijet events about a factor of two for events with more than two jets.

Table 4.10: Numbers of events after preselection and after the final selection for the four variables, for background samples (QCD, $Z \rightarrow \nu\nu$, $W \rightarrow \ell\nu$ and $t\bar{t}$). The first error is statistical, the second is due to the systematic uncertainty on the jet energy and the jet direction, the third is due to the theoretical uncertainty on the jet energy.

Selection	#jets	QCD	$W \rightarrow \nu\ell$	$t\bar{t}$	$Z \rightarrow \nu\nu$
Preselection	2	1.2×10^6	273	42	114
	> 2	1.8×10^6	605	1752	180
$H_T^{miss} + \Delta\phi$	2	$6 \pm 3 + 61 \begin{smallmatrix} +6 \\ -3 \end{smallmatrix}$	$10 \pm 2 + 1 \begin{smallmatrix} +5 \\ -6 \end{smallmatrix}$	$1 \pm 0 + 1 \begin{smallmatrix} +1 \\ -0 \end{smallmatrix}$	$10 \pm 1 + 4 \begin{smallmatrix} +9 \\ -5 \end{smallmatrix}$
	> 2	$7 \pm 2 + 110 \begin{smallmatrix} +8 \\ -5 \end{smallmatrix}$	$13 \pm 2 + 4 \begin{smallmatrix} +9 \\ -6 \end{smallmatrix}$	$10 \pm 1 + 4 \begin{smallmatrix} +7 \\ -4 \end{smallmatrix}$	$15 \pm 2 + 5 \begin{smallmatrix} +8 \\ -5 \end{smallmatrix}$
H_T^{miss}/H_T	2	$19 \pm 4 + 25 \begin{smallmatrix} +0 \\ -13 \end{smallmatrix}$	$13 \pm 2 + 6 \begin{smallmatrix} +10 \\ -8 \end{smallmatrix}$	$1 \pm 0 + 1 \begin{smallmatrix} +0 \\ -1 \end{smallmatrix}$	$13 \pm 2 + 7 \begin{smallmatrix} +11 \\ -6 \end{smallmatrix}$
	> 2	$9 \pm 3 + 12 \begin{smallmatrix} +4 \\ -5 \end{smallmatrix}$	$19 \pm 3 + 4 \begin{smallmatrix} +5 \\ -12 \end{smallmatrix}$	$13 \pm 1 + 3 \begin{smallmatrix} +5 \\ -7 \end{smallmatrix}$	$15 \pm 2 + 5 \begin{smallmatrix} +6 \\ -5 \end{smallmatrix}$
α_T	2	$0 + 1 + 0 \begin{smallmatrix} +0 \\ -0 \end{smallmatrix}$	$3 \pm 1 + 1 \begin{smallmatrix} +1 \\ -3 \end{smallmatrix}$	$0.3 \pm 0.1 + 0.1 \begin{smallmatrix} +0.2 \\ -0.2 \end{smallmatrix}$	$2 \pm 1 + 2 \begin{smallmatrix} +5 \\ -1 \end{smallmatrix}$
	> 2	$1 \pm 1 + 1 \begin{smallmatrix} +1 \\ -1 \end{smallmatrix}$	$3 \pm 1 + 5 \begin{smallmatrix} +12 \\ -2 \end{smallmatrix}$	$3 \pm 0 + 3 \begin{smallmatrix} +9 \\ -2 \end{smallmatrix}$	$6 \pm 1 + 4 \begin{smallmatrix} +7 \\ -3 \end{smallmatrix}$
$Th\Delta\Phi$	2	$0 + 1 + 2 \begin{smallmatrix} +1 \\ -0 \end{smallmatrix}$	$9 \pm 2 + 2 \begin{smallmatrix} +5 \\ -5 \end{smallmatrix}$	$0.4 \pm 0.1 + 0.3 \begin{smallmatrix} +0.4 \\ -0.2 \end{smallmatrix}$	$8 \pm 1 + 4 \begin{smallmatrix} +10 \\ -3 \end{smallmatrix}$
	> 2	$0 + 1 + 4 \begin{smallmatrix} +3 \\ -0 \end{smallmatrix}$	$9 \pm 2 + 3 \begin{smallmatrix} +6 \\ -4 \end{smallmatrix}$	$3 \pm 0 + 2 \begin{smallmatrix} +3 \\ -1 \end{smallmatrix}$	$10 \pm 1 + 4 \begin{smallmatrix} +5 \\ -4 \end{smallmatrix}$

Table 4.11: Numbers of events after preselection and after final selection for the four variables, for signal benchmark-points LM0 - LM5 for dijet events (a) and for events with more than two jets (b). The statistical uncertainties given in this table correspond to the number of events in the simulated samples.

Selection cut	#jets	LM0	LM1	LM2	LM3	LM4	LM5
Preselection	2	338	161	26	46	47	13
	> 2	2 187	442	77	354	239	72
$H_T^{miss} + \Delta\phi$	2	139±3	105±1	19.6±0.2	31.1±0.5	33.7±0.5	10.4±0.1
	> 2	452±5	236±2	50.3±0.3	146±1	122±1	42.8±0.2
$H_T^{miss}/H_T > 0.5$	2	142±3	94±1	15.7±0.2	26.5±0.5	28.7±0.4	8.3±0.1
	> 2	350±4	161±2	31.4±0.2	77.1±0.8	66.5±0.6	22.0±0.2
$\alpha_T > 0.6$	2	50±2	41±1	7.0±0.1	12.0±0.3	12.7±0.3	3.8±0.1
	> 2	131±3	73±1	14.3±0.2	32.2±0.5	28.2±0.4	9.4±0.1
$Th\Delta\Phi > 1$ rad	2	120±3	84±1	14.0±0.2	23.2±0.4	25.5±0.4	7.4±0.1
	> 2	227±4	107±1	19.7±0.2	47.1±0.6	40.8±0.5	13.1±0.1

4.11 A Second Method for Evaluating the Signal Significance

4.11.1 Introduction

The large cross-section of QCD multijet events and the systematic uncertainty of the calorimeter response (Sect. 4.9.2) could lead to a contribution of QCD events surpassing by far the expectations given in Table 4.10. These events could be mis-identified as SUSY signal events (Sect. 4.8), should systematic uncertainties be underestimated. Therefore, a method has been developed to clearly distinguish between unexpected QCD multijet background and SUSY signal events.

A version of this method, using α_T as final selection variable, has been introduced in Ref. [64]. The method is based on a combination of three different variables, $|\eta|$ of the leading jet, H_T and the ratio R :

$$R = \frac{\# \text{ events which pass the final event selection}}{\# \text{ events which are rejected by the final event selection}}. \quad (4.12)$$

SUSY signal events are produced more centrally in pseudo-rapidity compared to the SM backgrounds, in particular QCD events (Sect. 4.3). The total transverse momentum H_T is used to suppress SM background in the preselection. Its distribution is presented in Fig. 4.24 for QCD events after the preselection, and for all other processes after the selection on $H_T^{miss}/H_T > 0.5$ (a), $\alpha_T > 0.6$ (b) and $Th\Delta\phi > 1$ rad (c). Low H_T regions, e.g. $300 < H_T < 350$ GeV/c, are background dominated while SUSY events are expected to become more prominent at large H_T . Requiring $H_T > 350$ GeV/c as done in the preselection or cutting even tighter at e.g. $H_T > 450$ GeV/c increases the relative contribution of signal events.

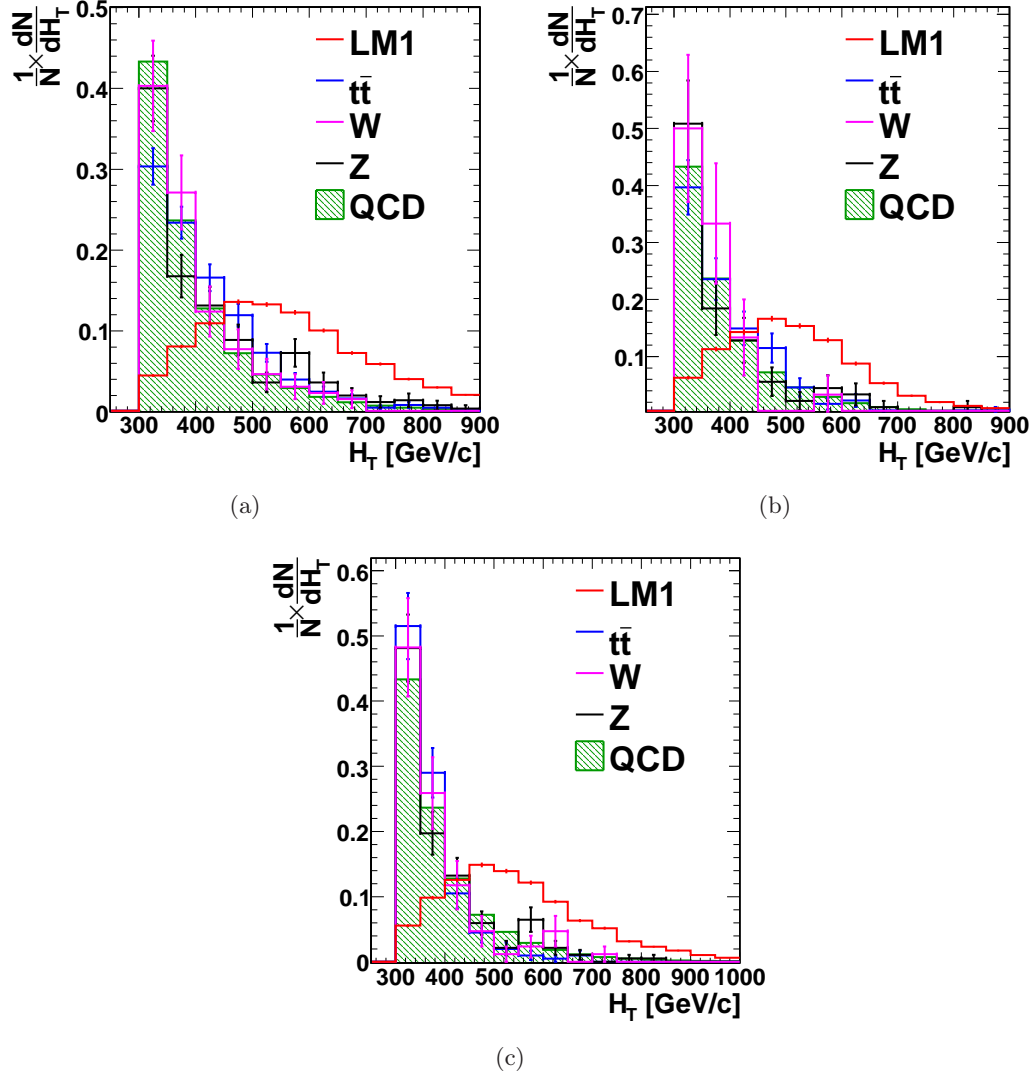


Figure 4.24: H_T distribution for the SM background and for SUSY events at the LM1 point. The distributions are normalized for each component to unit area. The distribution for QCD multijet events is shown after the preselection, with the cut on H_T lowered to 300 GeV/c. The distribution of all other events is shown after the selection on $H_T^{miss}/H_T > 0.5$ (a), $\alpha_T > 0.6$ (b) and $Th\Delta\Phi > 1$ rad (c). The error bars indicate the statistical uncertainty on the number of events in the MC generated samples.

The presence of a SUSY signal would manifest itself therefore with two distinctive features as exemplary illustrated in the right-hand side of Fig. 4.25 for events of the LM1 parameter-set plus background events:

- tighter requirements on H_T increase R ,
- the increase in R is largest at small values of $|\eta|$.

The ratio R has been determined for the H_T^{miss}/H_T , the α_T , and the $\text{Th}\Delta\Phi$ selection ($R(H_T^{miss}/H_T)$, $R(\alpha_T)$ and $R(\text{Th}\Delta\Phi)$). For comparison, the distributions of R are presented for SM background only on the left-hand side of Fig. 4.25. If no SUSY signal is present R is approximately constant as a function of pseudo-rapidity and within errors independent of H_T . The discussed method is based on this difference between the two scenarios, SM background only and SM background plus a SUSY signal. The method is only viable for variables whose resolution remains constant or improves with increasing H_T . In case that the resolution worsens with H_T , R increases with H_T , as visible in Fig. 4.26 for the H_T^{miss} selection. This mimics the expected behavior in the presence of a SUSY signal. SM background could therefore be mis-interpreted as signal. The discussed method is hence not used with H_T^{miss} as final selection variable.

4.11.2 The Profile-Likelihood Method

To establish an excess of events over SM expectations the procedure is as follows:

1. measure R in the range $|\eta| < 1$ for events with $300 < H_T < 350$ GeV/c and compare it to prediction from simulation;
2. measure R in the range $|\eta| < 1$ for events with $300 < H_T < 350$ GeV/c and compare to R for events with $350 < H_T < 450$ GeV/c and $H_T > 450$ GeV/c.

The compatibility between values of R can be tested with the Profile Likelihood Method for ratios of Poisson means [78] which is widely used in γ -Ray Astronomy [79] to estimate the significance of the observation of n_{on} events, if the expected number of background events is extracted from a subsidiary measurement n_{off} (*on/off problem*).

The compatibility issue can be reformulated in this context with:

- n_{on} : Number of events in $|\eta| < 1$ which pass the selection and have $H_T > 450$ GeV/c.
- n_{off} : Number of events in $|\eta| < 1$ which pass the selection and are in the background dominated H_T region $300 < H_T < 350$ GeV/c.

In addition I define:

- b_{on} : Number of events in $|\eta| < 1$ which do not pass the selection and have $H_T > 450$ GeV/c.
- b_{off} : Number of events in $|\eta| < 1$ which do not pass the selection and are in the background dominated H_T region $300 < H_T < 350$ GeV/c.

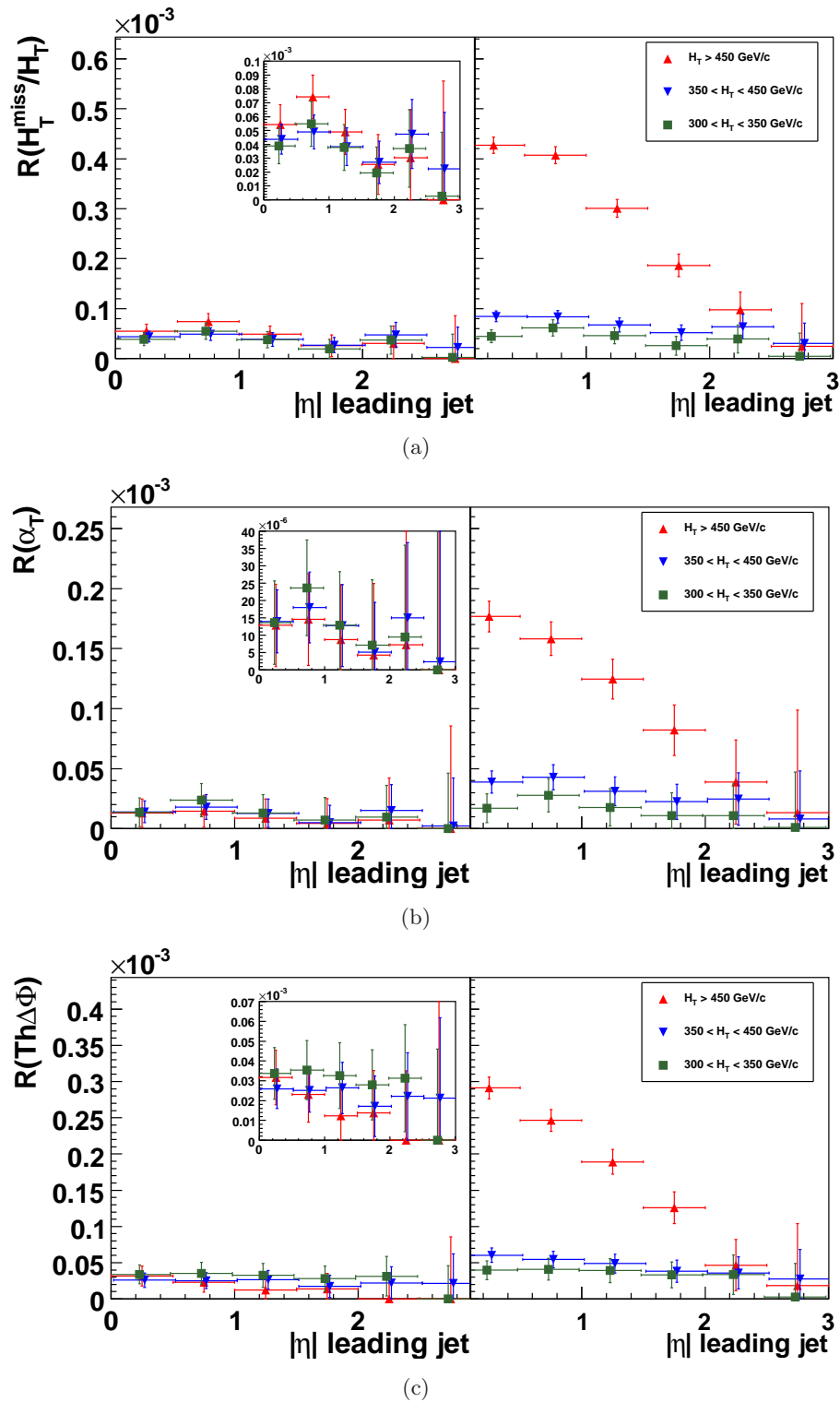


Figure 4.25: Ratios $R(H_T^{miss}/H_T)$ (a), $R(\alpha_T)$ (b) and $R(Th\Delta\Phi)$ (c) as a function of $|\eta|$ of the leading jet in events with more than two jets, for different H_T ranges. The plots on the left-hand side show R for SM background only (expanded in the insets), the plots on the right-hand side show R in the presence of LM1 SUSY events. The error bars are statistical.

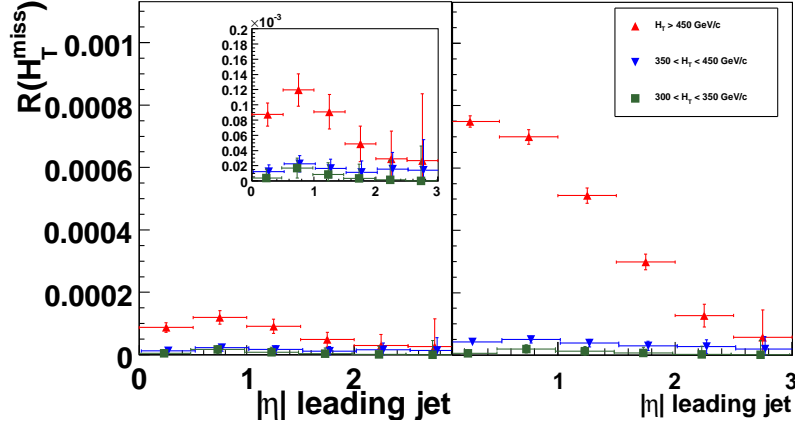


Figure 4.26: Ratios $R(H_T^{miss})$ as a function of $|\eta|$ of the leading jet in events with more than two jets, for different H_T ranges. The plot on the left-hand side shows R for SM background only (expanded in the inset), the plot on the right-hand side shows R in the presence of LM1 SUSY events. The error bars are statistical.

The ratio R can then be rewritten as:

$$R(H_T > 450 \text{ GeV}/c) = \frac{n_{on}}{b_{on}}, \quad (4.13)$$

for events with $H_T > 450 \text{ GeV}/c$ and:

$$R(300 < H_T < 350 \text{ GeV}/c) = \frac{n_{off}}{b_{off}}, \quad (4.14)$$

for events with $300 < H_T < 350 \text{ GeV}/c$. The statistical errors on b_{off} and b_{on} are negligible as both are approximately five orders of magnitude larger than n_{on} and n_{off} . MC simulation is used to determine the factor x_{SM} which relates the ratios $R(H_T > 450 \text{ GeV}/c)$ and $R(300 < H_T < 350 \text{ GeV}/c)$ in the absence of SUSY signal:

$$x_{SM} = \frac{R(300 < H_T < 350 \text{ GeV}/c)}{R(H_T > 450 \text{ GeV}/c)}, \quad (4.15)$$

This can be reformulated in the notation of the *on/off problem*:

$$n_{on} = n_{off} \cdot \frac{b_{on}}{x_{SM} \cdot b_{off}} = n_{off} \cdot \frac{1}{\tau}, \quad (4.16)$$

with $\tau = x_{SM} \cdot \frac{b_{off}}{b_{on}}$.

Once the number of n_{on} , n_{off} , b_{on} and b_{off} events have been measured, the probability of this observation, assuming the SM, can be expressed as significance Z in units of standard deviations σ [78]:

$$Z = \sqrt{2} \left[n_{on} \ln \frac{n_{on}(1 + \tau)}{n_{on} + n_{off}} + n_{off} \ln \frac{n_{off}(1 + \tau)}{(n_{on} + n_{off})\tau} \right]^{1/2}. \quad (4.17)$$

4.11.3 Systematic Uncertainties

The value of x_{SM} is the only parameter in Eq. 4.17 derived from MC simulations. A systematic error of x_{SM} could lead to deviations of the calculated Z from the true significance of an observation. Possible uncertainties on x_{SM} have therefore been studied in detail. The values of x_{SM} for events with two and more jets are given in Table 4.12, once for the standard cuts and once for loosened cuts. The cuts have been lowered to study the dependence of x_{SM} on the number of selected QCD events. The H_T^{miss}/H_T cut is lowered to 0.4, the α_T cut to 0.52 and the cut on $Th\Delta\phi$ to 0.8 rad. Loosening the cuts leads to larger values of x_{SM} , which corresponds to a decrease of R for tighter H_T cuts. This reduction in R with increasing H_T is due to the reduced importance of neglected jets with $p_T < 50$ GeV/c. For unexpected QCD background the values of x_{SM} used in Eq. 4.17 would be smaller than their true values and hence the calculated significance Z would also be smaller than the true significance. Unexpected QCD background can therefore not be mistaken as SUSY signal.

Table 4.12: Value of x_{SM} for SM background dijet events and events with more than two jets, for the standard selection cuts and for loosened selection cuts. The stated errors corresponds to the statistical uncertainties on x_{SM} .

variable	cut	$x_{SM}(2 \text{ jet})$	$x_{SM>(>2 \text{ jets})$
H_T^{miss}/H_T	> 0.5	0.6 ± 0.2	0.7 ± 0.2
	> 0.4	1.2 ± 0.3	1.2 ± 0.2
α_T	> 0.6	$1.8_{-1.3}^{+1.9}$	$1.4_{-0.6}^{+0.8}$
	> 0.52	$5.7_{-4.0}^{+3.5}$	$2.7_{-0.4}^{+0.5}$
$Th\Delta\Phi$	> 1.0 rad	$1.1_{-0.4}^{+0.5}$	$1.3_{-0.4}^{+0.5}$
	> 0.8 rad	$1.6_{-0.5}^{+0.6}$	2.2 ± 0.5

The value of x_{SM} is determined by the ratio R as a function of H_T . A change in the H_T dependence of R would also affect x_{SM} . To understand the systematic uncertainties on this dependence the relative contributions of the different processes in the numerator and in the denominator have been studied. The denominator of R (Eq. 4.12) is dominated by QCD multijet events, whereas $t\bar{t}$, W and Z events dominate in the numerator in the absence of SUSY signal. The dependence of R on H_T is determined by the difference between the shape of the H_T distribution for the QCD multijet background and for the other processes. The H_T distribution of selected W and Z events is similar to that of the rejected QCD multijet events, as illustrated for the H_T^{miss}/H_T selection in Fig. 4.24(a). Fig. 4.24(a) also shows that the slope of the H_T distribution for $t\bar{t}$ events is slightly less steep than for QCD events. Similar distributions for the α_T and $Th\Delta\phi$ selection are shown in Fig. 4.24 (b-c). The number of selected events is much smaller here and the distributions are compatible within statistical uncertainties. The H_T distributions of the different processes

are affected by theoretical uncertainties (Fig. 4.21). A change in the shape of the H_T distributions and a different background composition would influence the H_T dependence of R . The relative contribution of the different processes can either be estimated from MC simulations as done in this analysis or by using data-driven background estimations like those discussed in Ref. [76]. The systematic uncertainties associated to the shape and the different background contributions is taken into account by varying the total cross-section and the differential cross-section ($\frac{d\sigma}{dE_T}$ of Fig. 4.21) of each process. The total cross-section of QCD events has been varied by $\pm 100\%$, that of $t\bar{t}$ by $\pm 30\%$ and the cross-sections of W and Z events have each been varied by 11% . These numbers correspond to those discussed in Sect. 4.9. The differential cross-sections have been varied by $\pm 10\%$ (Sect. 4.9). In addition it has been studied how x_{SM} is affected by the jet reconstruction uncertainties of Sect. 4.9: a gaussian smearing of the jet p_T and ϕ and a jet energy scaling of $\pm 5\%$.

The variations to which x_{SM} is most sensitive are:

- a gaussian smearing of the jet p_T distribution by 10% which decreases x_{SM} in events with more than two jets for the α_T selection from 1.4 (Table 4.12) to 0.7 ± 0.3 .
- a gaussian smearing of the jet ϕ direction by 0.1 rad which
 - increases x_{SM} in dijet events for the H_T^{miss}/H_T selection from 0.6 to 1.2 ± 0.3 .
 - increases x_{SM} in dijet events for the $Th\Delta\Phi$ selection from 1.1 to $2.0_{-0.7}^{+0.9}$.
 - increases x_{SM} in events with more than two jets for the $Th\Delta\Phi$ selection from 1.3 to 2.6 ± 0.8 .
- an increase by 10% in the jet energy scale of QCD events
 - increases x_{SM} from 1.3 to $2.3_{-0.7}^{+0.8}$ in events with more than two jets for the $Th\Delta\Phi$ selection.
 - increases x_{SM} from 0.7 to 0.9 ± 0.2 in events with more than two jets for the H_T^{miss}/H_T selection.
- an increase by 10% in the jet energy scale of $Z \rightarrow \nu\bar{\nu}$ events
 - decreases x_{SM} from 1.4 to 0.7 ± 0.3 in events with more than two jets for the α_T selection.

The statistical uncertainties on the value of x_{SM} after the variation are not taken into account in the calculation of the systematic uncertainties. Further studies with large MC samples could reduce this statistic uncertainty and yield more precise knowledge about the real systematic uncertainties on x_{SM} . The systematic uncertainties are combined by quadratically adding all the positive and the negative variations, thus assuming that they are uncorrelated. The values of x_{SM} including statistic and systematic uncertainties are given in Table 4.13. Note that the combined systematic uncertainty for the α_T selection and events with more than two jets is in fact as large as x_{SM} , hence the method fails in this case.

Table 4.13: Values of x for SM background dijet events (right-hand side) and events with more than two jets (left-hand side). The first error corresponds to the statistical uncertainties on x the second to the systematic uncertainties.

	$x_{SM}(2 \text{ jet})$	$x_{SM>(>2 \text{ jets})}$
$H_T^{miss}/H_T > 0.5$	$0.6 \pm 0.2 \begin{smallmatrix} +0.1 \\ -0.2 \end{smallmatrix}$	$0.7 \pm 0.2 \begin{smallmatrix} +0.5 \\ -0.1 \end{smallmatrix}$
$\alpha_T > 0.6$	$1.8 \begin{smallmatrix} +1.9 & +0.9 \\ -1.3 & -1.0 \end{smallmatrix}$	$1.4 \begin{smallmatrix} +0.8 & +0.3 \\ -0.6 & -1.4 \end{smallmatrix}$
$Th\Delta\Phi > 1$	$1.1 \begin{smallmatrix} +0.5 & +1.0 \\ -0.4 & -0.3 \end{smallmatrix}$	$1.3 \begin{smallmatrix} +0.5 & +1.7 \\ -0.4 & -0.5 \end{smallmatrix}$

4.11.4 Calculating a Statistical Significance

Using Eq. 4.17 and the discussed values of x_{SM} the minimal required integrated luminosities for 5σ evidences of LM0 -LM5 SUSY signals $\mathcal{L}_{min}^{5\sigma}$ can be calculated. These luminosities are given in Table 4.14 for dijet events and events with more than two jets respectively. The propagated systematic uncertainty on Z due to the systematic error on x_{SM} and therefore on τ is also listed in this table.

The required luminosity $\mathcal{L}_{min}^{5\sigma}$ is smallest when $Th\Delta\Phi$ is used as final selection variable. In this case $\leq 100 \text{ pb}^{-1}$ would be sufficient to discover a LM1 SUSY signal both in dijet events and in events with more than two jets. The somewhat large luminosity necessary to detect a LM0 SUSY signal is due to the relative softness of jets in these events (Sect. 4.3). A 5σ discovery of LM3 or LM4 dijet events and events with more than two jets should be possible with less than 1 fb^{-1} of integrated luminosity.

4.11.5 Conclusion and Prospects

These results of the ratio-based method can be compared to the $\mathcal{L}_{min}^{5\sigma}$ values of Table 4.8 obtained with the analysis method presented in Sect. 4.8:

- **Dijet events:**
Taking into account the uncertainties of both methods, the ratio-based method together with the $Th\Delta\phi$ path yields the smallest $\mathcal{L}_{min}^{5\sigma}$, except for LM0 SUSY events. The softness of jets in LM0 SUSY events and the large statistical uncertainties on the ratio-based method make the first method more favorable for these events.
- **Events with more than two jets:**
A selection on H_T^{miss} together with the first analysis method allows for a 5σ discovery with the least integrated luminosity. However, the variable H_T^{miss} is strongly affected by upward scaling of the jet energy, even if this mis-measurement occurs only with a very small frequency (Sect. 4.9.2). A selection on $Th\Delta\Phi$ might be a more robust choice also with more than two jets. For a selection on $Th\Delta\Phi$ and SUSY signals of parameter-sets LM1-LM5, the ratio-based method yields smaller $\mathcal{L}_{min}^{5\sigma}$ than the first analysis method.

Table 4.14: Minimum required integrated luminosity for a 5σ discovery of SUSY signals $\mathcal{L}_{min}^{5\sigma}$ for dijet events and for events with more than two jets. Two errors are stated for every luminosity. The first error is due to the statistical uncertainties on x , the second is due to the systematic uncertainties on x .

SUSY	#jets	$H_T^{miss}/H_T > 0.5$	$\alpha_T > 0.6$	$\text{Th}\Delta\Phi > 1 \text{ rad}$
LM0	2	118 $^{+223}_{-46}$ $^{+223}_{-29}$	509 $^{+4116}_{-313}$ $^{+13253}_{-232}$	88 $^{+110}_{-32}$ $^{+61}_{-45}$
	>2	54 $^{+55}_{-18}$ $^{+19}_{-30}$	90 $^{+153}_{-38}$ $^{+\infty}_{-21}$	40 $^{+28}_{-13}$ $^{+44}_{-23}$
LM1	2	49 $^{+36}_{-13}$ $^{+36}_{-8}$	55 $^{+131}_{-18}$ $^{+52}_{-11}$	34 $^{+19}_{-8}$ $^{+12}_{-12}$
	> 2	48 $^{+32}_{-13}$ $^{+12}_{-22}$	55 $^{+48}_{-18}$ $^{+\infty}_{-9}$	39 $^{+21}_{-10}$ $^{+31}_{-20}$
LM2	2	388 $^{+1034}_{-168}$ $^{+1034}_{-108}$	260 $^{+1508}_{-105}$ $^{+412}_{-70}$	238 $^{+312}_{-89}$ $^{+172}_{-124}$
	>2	415 $^{+940}_{-185}$ $^{+245}_{-278}$	353 $^{+737}_{-159}$ $^{+\infty}_{-86}$	291 $^{+368}_{-118}$ $^{+644}_{-196}$
LM3	2	234 $^{+405}_{-89}$ $^{+405}_{-56}$	179 $^{+762}_{-68}$ $^{+240}_{-45}$	154 $^{+156}_{-52}$ $^{+90}_{-74}$
	>2	124 $^{+122}_{-41}$ $^{+41}_{-68}$	137 $^{+164}_{-51}$ $^{+\infty}_{-27}$	100 $^{+72}_{-32}$ $^{+111}_{-58}$
LM4	2	184 $^{+266}_{-65}$ $^{+266}_{-41}$	144 $^{+496}_{-52}$ $^{+171}_{-34}$	119 $^{+104}_{-38}$ $^{+62}_{-54}$
	>2	137 $^{+141}_{-46}$ $^{+47}_{-76}$	149 $^{+186}_{-57}$ $^{+\infty}_{-29}$	109 $^{+82}_{-35}$ $^{+127}_{-64}$
LM5	2	1095 $^{+15178}_{-611}$ $^{+15178}_{-419}$	593 $^{+15804}_{-283}$ $^{+1724}_{-196}$	635 $^{+1931}_{-305}$ $^{+869}_{-402}$
	>2	742 $^{+3183}_{-381}$ $^{+618}_{-544}$	632 $^{+2218}_{-321}$ $^{+\infty}_{-181}$	524 $^{+1027}_{-244}$ $^{+2087}_{-384}$

The novel analysis method presented here extracts the statistical significance from histograms such as those shown in Fig. 4.25. It provides an interesting cross-check to the more common "cut and count" approach presented in Sect. 4.8. Whereas the method of Sect. 4.8 is more affected by systematic uncertainties on the number of selected QCD events the uncertainty of the ratio-based method is related to our knowledge about the H_T dependence of the ratios R .

The ratio-based method does not yet exploit the full information given in the histograms in Fig. 4.25, as it only takes into account events in which $|\eta| < 1$ for the leading jet. In the future the probabilities of observing the measured number of n_{off} , n_{on} events could be combined for all bins of $|\eta|$. However, this requires a detailed knowledge of the systematic uncertainties of the η shape of the different processes and the correlation of this shape with H_T .

Chapter 5

Conclusions and Prospects

In 2010 the LHC has started to collide particles with center-of-mass energies of 7 TeV and 10 TeV will be reached in the coming years. At these high energies we will be able to search for new phenomena beyond the current experimental limits. A favored theory for physics beyond the Standard Model (SM) is Supersymmetry (SUSY). This thesis presents an experimental strategy for SUSY searches with multijet events at CMS. The high cross-section associated to the production of heavy colored particles makes this analysis suitable for early data. However, searches at hadron colliders are quite challenging due to systematic uncertainties on jet reconstruction and the large jet multiplicity. A well understood detector is therefore crucial for this analysis.

In the future tagging b -quarks with the CMS pixel detector will become important for SUSY and other searches. Part of this thesis is therefore dedicated to a study of the charge deposited by cosmic ray muons in adjacent pixels (cluster) of the CMS pixel detector. The study is based on data taken with a magnetic field of 3.8 T in 2008. The agreement between data and simulation is reasonable, except for a peak at low cluster charges which is not described by the simulation. Two main reasons for this low charge peak have been identified. One is related to the relatively high readout thresholds in the 2008 data. These thresholds have been lowered in 2009. The second is connected to the random arrival of cosmic muons in time and does therefore not affect collision data. After the application of appropriate selection cuts the two cluster charge distributions have been found to agree quite well, and a fit has been applied to both distributions to extract the peak positions and widths.

The main focus of this thesis is on missing energy signatures at 10 TeV, investigating event topologies with 2 to 6 hadronic jets. The study is based on kinematic variables such as H_T^{miss} , H_T^{miss}/H_T , α_T and $Th\Delta\Phi$, their performance and robustness against mismeasurements of jets has been compared. The analysis is carried out in the context of SUSY for several sets of mSuGra parameters assuming an integrated luminosity of 100 pb^{-1} at a center-of-mass energy of 10 TeV. The distributions of the kinematic variables in dijet events are distinctively different from those in events with more than two jets. Hence, dijet events and events with more than two jets are treated separately. The effect of experimental and theoretical uncertainties of the jet energy scale and experimental uncertainties of the jet

direction have been investigated. The distribution of the variables H_T^{miss} and H_T^{miss}/H_T are more affected by systematic uncertainties than those of α_T or $Th\Delta\Phi$. The minimum required integrated luminosity for a 5σ discovery $\mathcal{L}_{min}^{5\sigma}$ has been compared for varying cuts on the kinematic variables. The cut values have been optimized to yield the smallest possible $\mathcal{L}_{min}^{5\sigma}$, taking into account the effect of systematic uncertainties. The optimum cut values are $H_T^{miss} > 250$ GeV/c $H_T^{miss}/H_T > 0.5$, $\alpha_T > 0.6$ and $Th\Delta\Phi > 1.0$ rad.

In dijet events $\mathcal{L}_{min}^{5\sigma}$ is smallest when the cut on $Th\Delta\phi$ is applied. The required $\mathcal{L}_{min}^{5\sigma}$ is:

- $54 + 7_{-8}^{+15}$ pb⁻¹ for the most favorable LM0 parameter-set,
- $86 + 13_{-15}^{+28}$ pb⁻¹ for the LM1 parameter-set.

For events with more than two jets $\mathcal{L}_{min}^{5\sigma}$ is in general smaller than for dijet events. In events with more than two jets a selection on H_T^{miss} is the most favorable for an early discovery of SUSY, for any of the mSuGra parameter-sets studied. The required $\mathcal{L}_{min}^{5\sigma}$ is then:

- $12 + 7_{-1}^{+2}$ pb⁻¹ for LM0 SUSY events,
- $25 + 19_{-4}^{+6}$ pb⁻¹ for LM1 events.

Furthermore, an additional robust analysis strategy has been described. Since SUSY particles are expected to be heavy and therefore preferably produced centrally, the distributions of the pseudo-rapidity η of the leading jet and the total transverse momentum H_T are sensitive to SUSY signals. A statistical interpretation of the correlation between H_T and the number of events has been presented. For SUSY dijet events and parameter-sets which yield jets at high momenta, such as LM1-LM5, this analysis method is more favorable, provided that the same event selection is applied. The luminosity $\mathcal{L}_{min}^{5\sigma}$ is smallest for a $Th\Delta\Phi$ selection:

- $\mathcal{L}_{min}^{5\sigma} = 34_{-8}^{+19+12}$ pb⁻¹ for LM1 SUSY dijet events,
- $\mathcal{L}_{min}^{5\sigma} = 39_{-10}^{+21+31}$ pb⁻¹ for LM1 SUSY events with more than two jets.

The combination of both methods should provide a robust search with early physics data.

Several interesting extensions to this study should be performed, eg. repeating the analysis with a centre-of-mass energy of 7 TeV and applying it to 2010 data. The study of systematic uncertainties should be updated with uncertainties extracted from collision data. Another very interesting task is to extend this analysis using b-tagging information and to gain insight in the nature of SUSY in case of a discovery. Additional information such as the number of b -jets in SUSY events constrain the number of SUSY parameter-sets compatible with data.

Appendix A

A.1 Coordinate System

A.1.1 Global Coordinate System

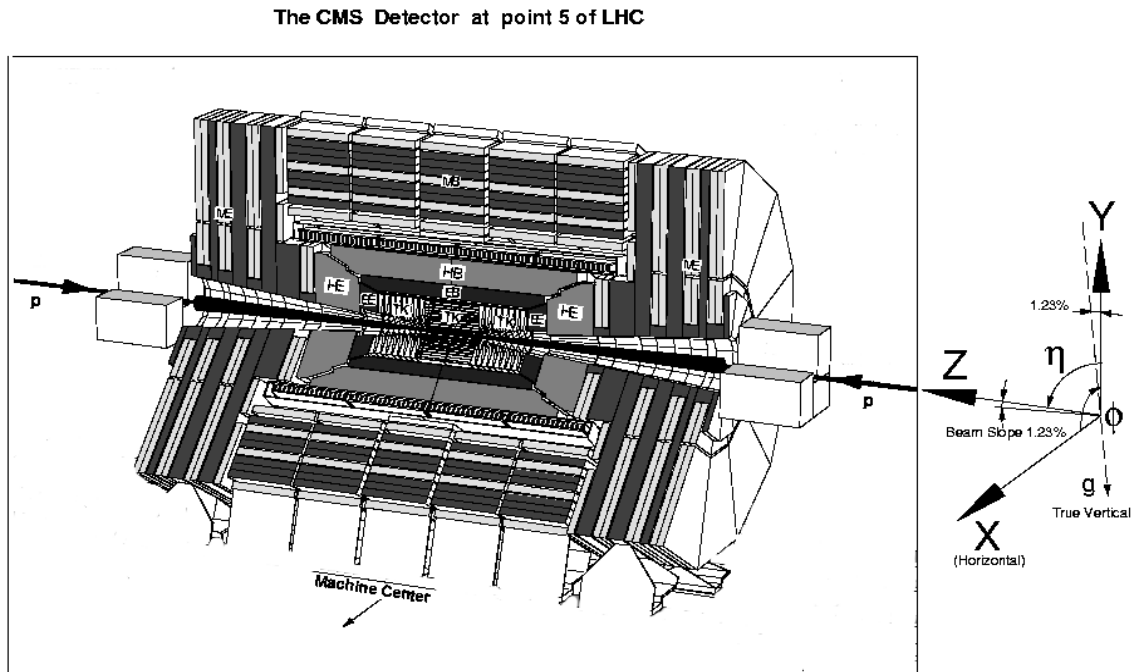


Figure A.1: The CMS coordinate system. Adapted from [27].

The CMS coordinate system is shown in figure A.1. The cartesian system (x, y, z) is right handed, with the nominal interaction point as origin and the x -axis pointing towards the center of the LHC ring. The polar coordinates are defined by:

$$\phi = \arctan\left(\frac{y}{x}\right) \quad (\text{A.1})$$

$$\theta = \arccos\left(\frac{z}{\sqrt{x^2 + y^2}}\right) \quad (\text{A.2})$$

A.1.2 Local Pixel Coordinate System

The local coordinate systems of the CMS pixel barrel and endcap detectors are shown in Fig. A.2. The z -axis is always perpendicular to the surface of the detector module. For barrel detectors the local x -axis is on the plane transverse to the beam direction and the local y -axis is parallel to the beam axis, while for endcap detectors, the local x -axis is along the radial direction.

The angles α and β are defined as projections with respect to the detector unit surface onto the local x - z (α) and y - z planes (β) (Fig. A.3).

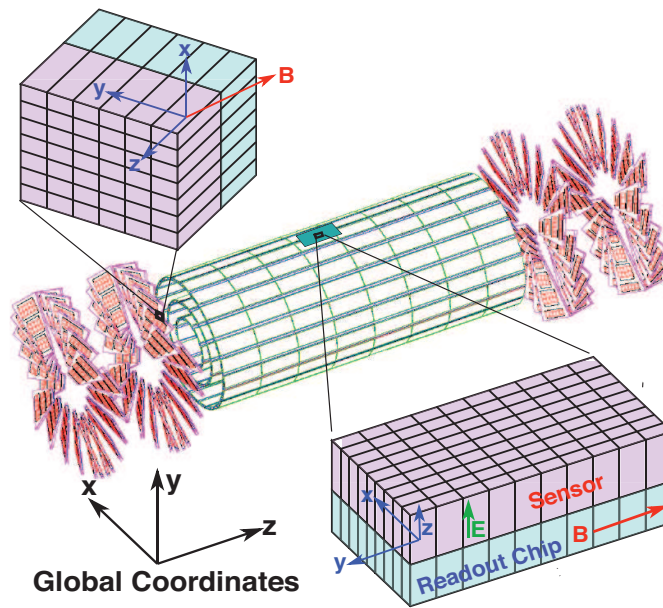


Figure A.2: Layout of the CMS pixel tracking system and the local coordinate systems in the pixel barrel and endcap detectors. Taken from [31].

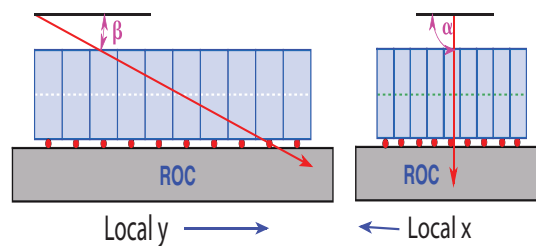


Figure A.3: The local angles α and β in the pixel detector [31].

A.2 Kinematic Quantities

Definition of some often used kinematic quantities:

- Pseudorapidity η :

$$\eta = -\ln \left(\tan \left(\frac{\theta}{2} \right) \right) \quad (\text{A.3})$$

- The distance of two objects defined in the plane transverse to the beam-line $\Delta\phi$:

- $\Delta R = \sqrt{\Delta\phi^2 + \Delta\eta^2}$

- Transverse Momentum p_T

$$p_T = \sqrt{(p_x)^2 + (p_y)^2} \quad (\text{A.4})$$

- The k_T distance $d_{i,j}$ of two particles i and j :

$$d_{i,j} = \min(p_{Ti}^2, p_{Tj}^2) \Delta R_{ij}^2 \quad (\text{A.5})$$

where p_{Ti} is the transverse momentum of particle i .

- The scalar sum over the transverse momenta of the n selected jets in an event H_T :

$$H_T = \sum_{j=1}^n p_{T,j} \quad (\text{A.6})$$

- The absolute value of the vectorial sum over the transverse momenta of the n selected jets in an event H_T^{miss} .

$$H_T^{miss} = \left| \sum_{j=1}^n \vec{p}_{T,j} \right| \quad (\text{A.7})$$

- The absolute value of the vectorial sum over the uncorrected energy deposits in calorimeter towers E_T^{miss} .

- The absolute value of the vectorial sum over all particles in the final state of an event after hadronization, except for neutrinos, muons and SUSY LSP \cancel{E}_T .

A.3 Abbreviations

List of abbreviations commonly used in this thesis. The abbreviations are listed in the order of their appearance in the text.

SM	Standard Model
SUSY	Supersymmetry
MSSM	Minimal Supersymmetric Standard Models
mSuGra	minimal Super Gravity (a special SUSY model)
LSP	Lightest Stable Particle

LHC	Large Hadron Collider
CERN	Conseil Europeen pour la Recherche Nucleaire (nowadays European laboratory for particle physics)
CMS	Compact Muon Solenoid
HCAL	Hadron Calorimeter
ECAL	Electromagnetic Calorimeter

MC	Monte Carlo
ME	Matrix Element
PS	Parton Shower

QCD	Quantum chromodynamics
CL	Confidence Level
$\mathcal{L}_{min}^{5\sigma}$	the minimal necessary luminosity to claim a 5σ discovery

Appendix B

B.1 Quantification of the Sensitivity of a Search for New Phenomena

Different ways to quantify the sensitivity of a search for new phenomena are discussed in literature. The quantification used in this analysis is based on the definition of a *sensitivity region* [68]: *The region of the parameters m for which:*

$$\gamma_\alpha(m) > CL, \tag{B.1}$$

where $\gamma(m)$ is the probability that a discovery will be claimed, assuming that a signal exists, and CL is the Confidence Level chosen for the limits in case there is no discovery. Here, γ_α depends on the desired test significance level α . The significance level of a test quantifies the probability of rejecting the default hypothesis if it is indeed true. In case of a counting experiment the sensitivity region can be defined by the condition:

$$S_m > S_{min}, \tag{B.2}$$

where S_m is the number of signal events as a function of the cut parameter m and S_{min} the minimum number of signal events necessary to fulfill the condition of Eq. B.1.

Assuming that the distribution of the number of observed events follows a Gauss distribution the condition in Eq. B.2 can be rewritten as:

$$S_{min} = a\sqrt{B} + b\sqrt{B + S_{min}}, \tag{B.3}$$

where B is the expected number of background events and a and b are the number of standard deviations corresponding to one sided Gaussian tests of significance α and β , respectively. To account for the deviations from Gaussian behavior that occurs in the Poisson tails an extended version of Eq. B.3 is used:

$$S_{min} = \frac{a^2}{8} + \frac{9b^2}{13} + a\sqrt{B} + \frac{b}{2}\sqrt{b^2 + 4a\sqrt{B} + 4B} \tag{B.4}$$

If the choice $a = b$ is made the maximum sensitivity is attained when:

$$\frac{1}{\sigma_{min}} = \frac{\epsilon(t) \cdot \mathcal{L}}{a^2 \cdot (5/8 + 9/13) + 2a\sqrt{B(t)}} \tag{B.5}$$

is maximal. Here, σ_{min} is the minimum "detectable" (according to the chosen criteria) signal cross-section, $\epsilon(t)$ is the signal efficiency of the chosen cut t and \mathcal{L} is the integrated luminosity. The advantages of this definition of signal sensitivity compared to the commonly used expressions S/\sqrt{B} and $S/\sqrt{S+B}$ are discussed in Ref. [68].

In order to deduce the minimal luminosity required for a potential 5σ discovery of SUSY events ($\mathcal{L}_{min}^{5\sigma}$), σ_{min} is set to the cross-section of the various parameter-sets and Eq. B.5 is solved for \mathcal{L} .

B.2 Control Distributions

Sect. 4.9.2 deals with the effects of moderate to large mis-measurements on different variables. In this section three relevant variables for jet mis-measurement of jets are discussed. These variables are the minimal angle between \vec{H}_T^{miss} and the three leading jets in the transversal plane $\Delta\phi(H_T^{miss}, j)$ (Fig. B.1), a variable akin to the latter called *biased* $\Delta\phi$ and the angle $\Delta\phi(p_T^{miss}, H_T^{miss})$ between a track based missing energy p_T^{miss} and the calorimeter-jet based H_T^{miss} .

In SM events without neutrinos large missing energy is in most cases due to severe mis-measurement of at least one of the leading jets. This fact is exploited by the variable $\Delta\phi(H_T^{miss}, j)$, as H_T^{miss} is typically pointing into the direction of one of the leading jets, if the measured jet-energy is too small (Fig. B.1(a)). However, when the measured jet-energy is too large H_T^{miss} is pointing in the opposite direction (Fig. B.1(b)).

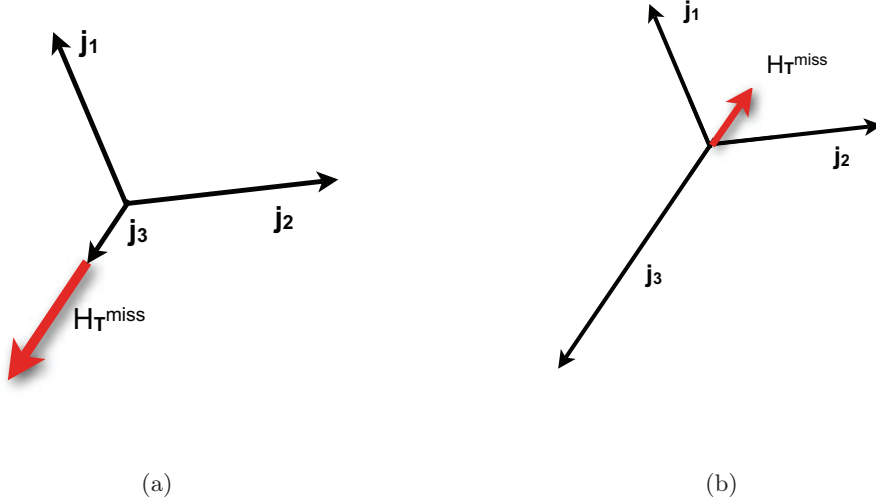


Figure B.1: A three jet QCD events in which the measured energy of the third jet j_3 is a) too small or b) too large. The direction and amplitude of the corresponding H_T^{miss} is indicated by a red arrow.

The *biased* $\Delta\phi$ is very similar to $\Delta\phi(H_T^{miss}, j)$ but excludes the tested jet from the calculation of H_T^{miss} :

$$biased \Delta\phi = \min_k \left(\Delta\phi \left(\left(\sum_{j=0}^{j=n} -\vec{j}_i \right) + \vec{j}_k, \vec{j}_k \right) \right), \quad (\text{B.6})$$

where n is the number of jets and \vec{j}_i the momentum of jets. This variable tests if there is at least one jet which, if rescaled by a certain factor, would be able to balance the event. For typical QCD events, with one dominating jet mis-measurement, this angle tends to be small. The variable *biased* $\Delta\phi$ solves the ambiguity of over/under estimated jet energies. In both cases the tested jet and the *biased* H_T^{miss} should point into the same ϕ -direction.

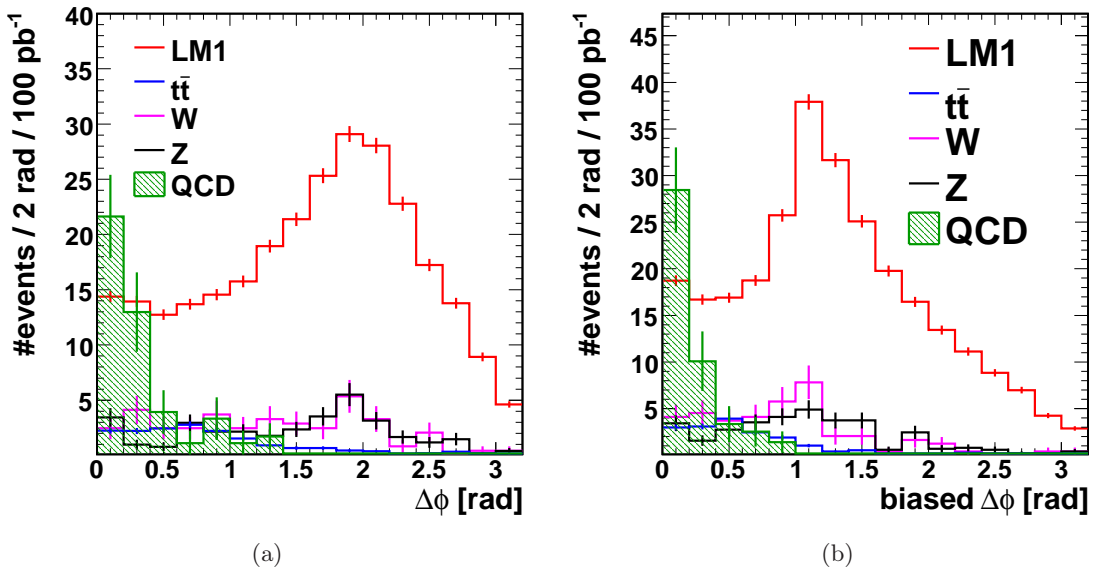


Figure B.2: Distribution of $\Delta\phi(H_T^{miss}, j)$ (a) and *biased* $\Delta\phi$ (b) after the pre-selection and a cut on $H_T^{miss}/H_T > 0.5$.

In Fig. B.2 the distribution of $\Delta\phi(H_T^{miss}, j)$ and *biased* $\Delta\phi$ are presented after a cut on $H_T^{miss}/H_T > 0.5$. In both distributions QCD events tend to be centered around zero while events with real missing transverse energy, from neutrinos or LSP, tend to have larger values of $\Delta\phi$. A cut on $\Delta\phi(H_T^{miss}, j) > 0.5$ or *biased* $\Delta\phi > 0.5$ could efficiently suppress most of the remaining QCD background.

A comparison of the kinematics of the calorimeter jets with that of the measured tracks may also be used to indicate mismeasurement of jets. A missing transverse momentum is calculated from the tracks as:

$$\vec{p}_T^{miss} = \sum_{i=1}^n -\vec{p}_{T_i}, \quad (\text{B.7})$$

where \vec{p}_{T_i} are the momenta of the tracks below 500 GeV/c. When track and jet kinematics agree, this missing transverse momentum points in the direction of H_T^{miss} determined from jets. For this comparison it does not matter whether H_T^{miss} is mismeasured due to neglected jets or other disturbing sources. Fig. B.3 shows the $\Delta\phi(p_T^{miss}, H_T^{miss})$ distribution after the final selection on α_T apart from the H_T^{miss} ratio cut. The $\Delta\phi(p_T^{miss}, H_T^{miss})$ variable is

an interesting supplement to H_T^{miss} ratio. As p_T^{miss} is based on trajectory measurements, it has entirely different sources of systematic uncertainties as those affecting the calorimeter based H_T^{miss} . This variable would also identify events in which a calorimeter jet is lost, or several jets are mismeasured.

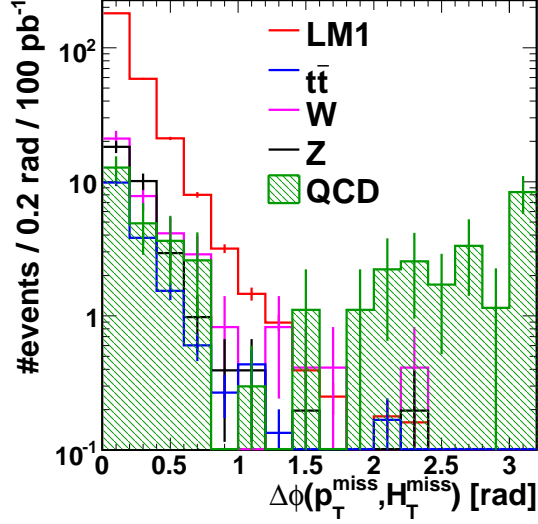


Figure B.3: The distribution of $\Delta\phi(p_T^{miss}, H_T^{miss})$ after the pre-selection and a cut on $H_T^{miss}/H_T > 0.5$.

In Fig. B.4 the correlation between the final selection variables and the control variables is presented, for dijet events (upper row), for events with more than two jets (lower row), for QCD events (left) and for LM1 SUSY events (right). Several features are worth noticing:

- The *biased* $\Delta\phi$ is almost 100% correlated to $Th\Delta\phi$. So these two variables are exchangeable.
- The variables α_T and *biased* $\Delta\phi$ show nearly no correlation (the absolute value of the correlation factor is smaller than 10%) in QCD events but are highly correlated (correlation factor $\approx 70\%$) in signal events. Events with large α_T have typically also large *biased* $\Delta\phi$. This allows a cut on *biased* $\Delta\phi$ which rejects possible remaining QCD events, while keeping the signal efficiency high.
- The same is true for the correlation of H_T^{miss} and H_T^{miss}/H_T with $\Delta\phi(H_T^{miss}, j)$ in dijet events. The correlation is small for QCD events (the absolute value of the factor is smaller than 10%) and large for LM1 SUSY events (the correlation factor is 29% for H_T^{miss} vs. $\Delta\phi$ and 56% for H_T^{miss}/H_T vs. $\Delta\phi$).
- The variable $\Delta\phi(p_T^{miss}, H_T^{miss})$ is nearly uncorrelated with all final selection variables in QCD events. Mismeasurements which affect the calorimeter-jet based variables do not necessarily increase $\Delta\phi(p_T^{miss}, H_T^{miss})$. For SUSY events $\Delta\phi(p_T^{miss}, H_T^{miss})$ is anti-correlated to all final selection variables. In these events a sizeable amount of energy is carried away by the LSP, therefore p_T^{miss} and H_T^{miss} point in the same direction.

Good combinations of selection and QCD control variables would be H_T^{miss} and H_T^{miss}/H_T in combination with $\Delta\phi(H_T^{miss}, j)$, and α_T in combination with *biased* $\Delta\phi$. The variable $Th\Delta\phi$ is very robust against systematic uncertainties hence a cut on a control variable would decrease the signal efficiency without adding much additional safety.

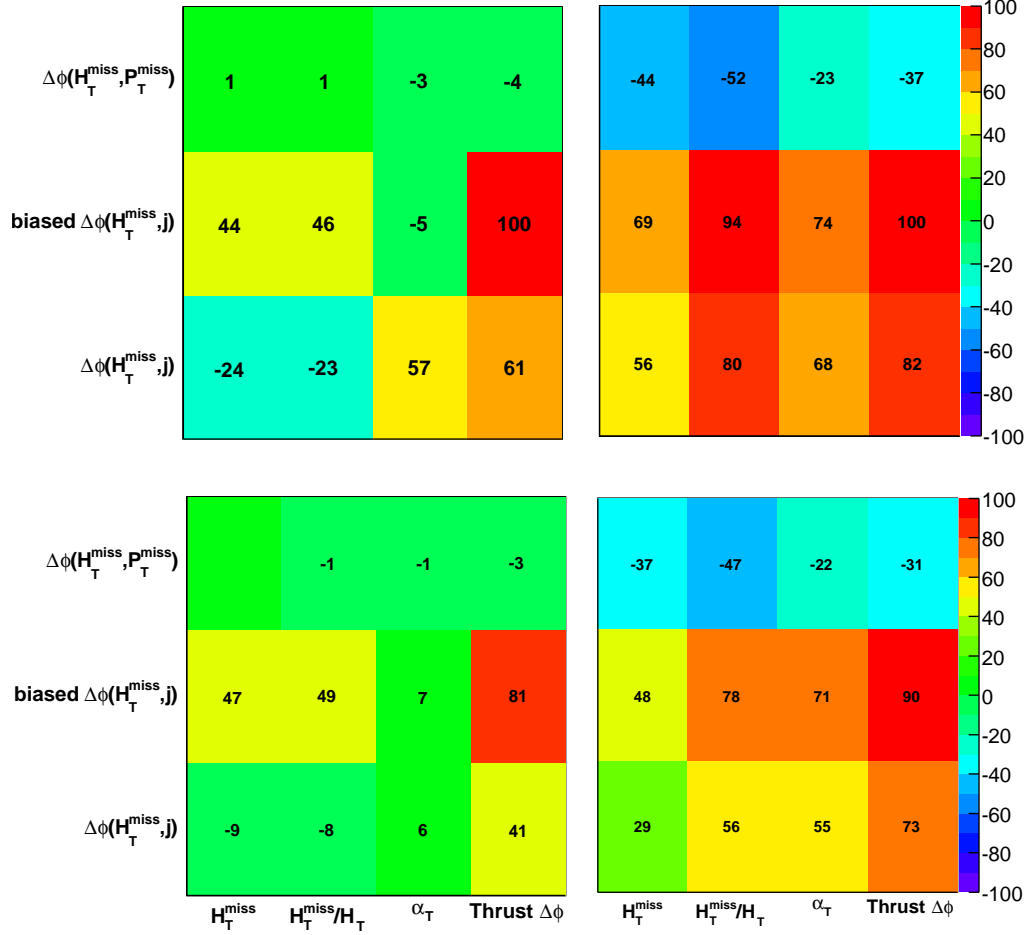


Figure B.4: Correlation between final selection variables and possible control variables in %. In the upper row correlation factors for dijet events are presented, in the lower row for events with more than two jets. On the left side are the correlation factors for QCD events, on the right those for SUSY events.

B.3 Event yields after Detector Performance Degradations

Table B.1: Expected number of events for an integrated luminosity of 100 pb^{-1} after different selection paths for background samples (QCD, $t\bar{t}$, W, Z +jets, and $Z \rightarrow \nu\bar{\nu}$) and the LM0 signal point. The given numbers are for the default case, for a gaussian p_T and gaussian ϕ smearing, for a $\pm 5\%$ jet-energy scaling. The uncertainties are statistical and correspond to the number of events in the simulated samples. For less than 1 event the error is the Poisson upper limit for a 68% CL.

(a) Final selection cut $H_T^{miss} > 250 \text{ GeV}/c$ plus requirement $\Delta\phi(H_T^{miss}, j_{1,2,3}) > 0.3 \text{ rad}$

	QCD	$W \rightarrow \nu l$	$t\bar{t}$	$Z \rightarrow \nu\nu$	Z+jets	LM0
no smearing	12 ± 3	22 ± 3	11 ± 1	25 ± 2	0.6 ± 0.4	591 ± 6
10 % gaussian p_T smearing	67 ± 5	23 ± 3	13 ± 2	26 ± 2	0.9 ± 0.5	613 ± 6
0.1 rad gaussian ϕ smearing	174 ± 6	23 ± 3	12 ± 2	26 ± 2	0.9 ± 0.5	620 ± 6
+5 % energy scale	19 ± 4	27 ± 3	14 ± 1	33 ± 3	0.6 ± 0.4	698 ± 6
-5 % energy scale	11 ± 3	15 ± 3	8 ± 1	19 ± 2	$0.3^{+0.4}_{-0.3}$	488 ± 5

(b) Final selection cut $H_T^{miss}/H_T > 0.5$

	QCD	$W \rightarrow \nu l$	$t\bar{t}$	$Z \rightarrow \nu\nu$	Z+jets	LM0
no smearing	28 ± 5	32 ± 4	14 ± 1	28 ± 2	1 ± 1	492 ± 5
10 % gaussian p_T smearing	61 ± 7	31 ± 4	15 ± 1	32 ± 3	2 ± 1	497 ± 5
0.1 rad gaussian ϕ smearing	37 ± 6	33 ± 4	14 ± 1	32 ± 3	1 ± 1	500 ± 5
+5 % energy scale	43 ± 6	41 ± 4	18 ± 1	39 ± 3	1 ± 1	548 ± 6
-5 % energy scale	30 ± 5	22 ± 3	11 ± 1	22 ± 2	1 ± 1	430 ± 5

(c) Final selection cut $\alpha_T > 0.6$

	QCD	$W \rightarrow \nu l$	$t\bar{t}$	$Z \rightarrow \nu\nu$	Z+jets	LM0
no smearing	1 ± 1	6 ± 2	3.5 ± 0.3	7 ± 1	0.6 ± 0.4	181 ± 3
10 % gaussian p_T smearing	0 ± 1	9 ± 2	3.9 ± 0.4	9 ± 1	1 ± 1	182 ± 3
0.1 rad gaussian ϕ smearing	0 ± 1	7 ± 2	3.7 ± 0.4	8 ± 1	0.6 ± 0.4	186 ± 3
+5 % energy scale	2 ± 1	11 ± 2	6.5 ± 0.5	14 ± 2	0.9 ± 0.5	263 ± 4
-5 % energy scale	0 ± 1	2 ± 1	2 ± 0.3	6 ± 1	0.3 ± 0.3	112 ± 3

(d) Final selection cut $Th\Delta\Phi > 1.0 \text{ rad}$

	QCD	$W \rightarrow \nu l$	$t\bar{t}$	$Z \rightarrow \nu\nu$	Z+jets	LM0
no smearing	0 ± 1	18 ± 3	3.2 ± 0.3	18 ± 2	0.6 ± 0.4	346 ± 4
10 % gaussian p_T smearing	3 ± 2	17 ± 3	4.1 ± 0.4	21 ± 2	1 ± 1	345 ± 4
0.1 rad gaussian ϕ smearing	5 ± 2	17 ± 3	3.9 ± 0.4	22 ± 2	0.6 ± 0.4	354 ± 4
+5 % energy scale	1^{+2}_{-1}	23 ± 3	4.7 ± 0.4	25 ± 2	1 ± 1	385 ± 5
-5 % energy scale	0 ± 1	14 ± 2	2.4 ± 0.3	14 ± 2	$0.3^{+0.4}_{-0.3}$	303 ± 4

Bibliography

- [1] L. Evans and P. Bryant, “LHC machine,” *Journal of Instrumentation* **3** (2008) S08001.
- [2] CMS Collaboration, “The CMS experiment at the CERN LHC,” *Journal of Instrumentation* **3** (2008) S08004.
- [3] ATLAS Collaboration, “The ATLAS experiment at the CERN Large Hadron Collider,” *Journal of Instrumentation* **3** (2008) S08003.
- [4] LHCb Collaboration, “The LHCb detector at the CERN LHC,” *Journal of Instrumentation* **3** (2008) S08005.
- [5] ALICE Collaboration, “The ALICE experiment at the CERN LHC,” *Journal of Instrumentation* **3** (2008) S08002.
- [6] TOTEM Collaboration, “The TOTEM experiment at the CERN Large Hadron Collider,” *Journal of Instrumentation* **3** (2008) S08007.
- [7] LHCf Collaboration, “The LHCf detector at the CERN Large Hadron Collider,” *Journal of Instrumentation* **3** (2008) S08006.
- [8] C. Berger, “Elementarteilchenphysik,” *Springer* (2002).
- [9] G. Jungman and M. Kamionkowski, “Supersymmetric Dark Matter,” *Phys. Rept.* **267** (1996) 195–373.
- [10] S. Martin, “A Supersymmetry Primer,” (1997) [arXiv:hep-ph/9709356](https://arxiv.org/abs/hep-ph/9709356).
- [11] **Particle Data Group** Collaboration, C. Amsler et al., “The Review of Particle Physics,” *Physics Letters* **B667** (2008).
- [12] P. Schmuesser, “Feynman-Graphen und Eichtheorien fuer Experimentalphysiker,” *Springer* **2** (1994).
- [13] D. J. H. Chung et al., “The Soft Supersymmetry-Breaking Lagrangian: Theory and Applications,” *Phys. Rept.* **407** (2005) 1–203, [arXiv:hep-ph/0312378](https://arxiv.org/abs/hep-ph/0312378).
- [14] H. Georgi and S. Glashow, “Unity of All Elementary-Particle Forces,” *Physical Review Letters* **32** (1974) 438–441.
- [15] J. Zinn-Justin, “Renormalization and Renormalization Group Equation,” *NATO ASI Series C* **530** (1999) 375–388.

- [16] CMS Collaboration, “CMS physics: Technical Design Report,” *CERN-LHCC-2006-021* **2** (2006).
 - [17] Review Committee, “Run II luminosity performance of the Fermilab Tevatron,” *Department of Energy* (2002).
 - [18] DESY, “TESLA, an international, interdisciplinary center for research,” http://tesla.desy.de/new_pages/TDR_CD/brochure (2001).
 - [19] I. Abt, T. Ahmed, S. Aid, et al., “The H1 detector at HERA,” *Nucl. Instrum. Meth. A* **386** (1997) 310–347.
 - [20] S. Catani et al., “The QCD and Standard Model Working Group: Summary Report,” (2000) [arXiv:hep-ph/0005114](https://arxiv.org/abs/hep-ph/0005114).
 - [21] CMS Collaboration, “The Level-1 Trigger - Technical Design Report,” *CERN/LHCC 2000-038* **1** (2000).
 - [22] CMS Collaboration, “CMS physics: Technical Design Report,” *CERN-LHCC-2006-001* **1** (2006).
 - [23] CMS Collaboration, “The Muon Project - Technical Design Report,” *CERN/LHCC 97-32* (1997).
 - [24] CMS Collaboration, “Calorimeter Jet Quality Criteria for the First CMS Collision Data,” *CMS PAS JME-09-008* (2009).
 - [25] CMS Collaboration, “The Hadron Calorimeter Project - Technical Design Report,” *CERN/LHCC 97-31* (1997).
 - [26] S. Smith and E. Purcell, “Visible Light from Localized Surface Charges Moving Across a Grating,” *Physical Review* **92** (1953) 1069.
 - [27] CMS Collaboration, “The Electromagnetic Calorimeter Project - Technical Design Report,” *CERN/LHCC 97-33* (1997).
 - [28] CMS Collaboration, “The Tracker System Project - Technical Design Report,” *CERN/LHCC 94-38* (1994).
 - [29] CMS Collaboration, “Commissioning and Performance of the CMS Pixel Tracker with Cosmic Ray Muons,” *Journal of Instrumentation* **5** (2010).
 - [30] S. Dambach, “CMS Pixel Module Readout Optimization and Study of the B^0 Lifetime in the Semileptonic Decay Mode,” *ETH* (2009).
 - [31] M. Swartz, D. Fehling, G. Giurgiu, et al., “A New Technique for the Reconstruction, Validation, and Simulation of Hits in the CMS Pixel Detector,” *CMS NOTE-2007/033* (2007).
 - [32] P. Trueb, “CMS Pixel Module Qualification and Monte Carlo Study of $H \rightarrow \tau^+\tau^- \rightarrow \ell^+\ell^- \cancel{E}_T$,” *ETH* (2008).
 - [33] **GEANT4** Collaboration, S. Agostinelli, J. Allison, K. Amako, et al., “GEANT 4–A Simulation Toolkit,” *Nucl. Instrum. Meth. A* **506** (2003) 250–303.
-

-
- [34] CMS Collaboration, “The CMS Silicon Strip Tracker Operation and Performance with Cosmic Rays in 3.8 T Magnetic Field,” *CMS-CFT-09-002* (2009).
- [35] CMS Collaboration, “Simulation of Cosmic Muons and Comparison with Data from the Cosmic Challenge using Drift Tube Chambers,” *CMS NOTE 2007/024* (2007).
- [36] CMS Collaboration, “Search for Heavy Stable Charged Particles with 100 pb^{-1} and 1 fb^{-1} in the CMS Experiment,” *CMS PAS EXO-08-003* (2008).
- [37] A. Rizzi, K. Nawrocki, P. Traczyk, et al., “Search for Heavy Stable Charged Particles with 100 pb^{-1} and 1 fb^{-1} at CMS experiment,” *CMS AN-2007/049* (2007).
- [38] T. Sjostrand, S. Mrenna, and P. Skands, “PYTHIA 6.4: Physics and Manual,” *FERMILAB-PUB-06-052-CD-T* (2006) [arXiv:hep-ph/0603175](#).
- [39] F. Maltoni and T. Steltzer, “MadEvent: Automatic Event Generation with MadGraph,” *JHEP* **0302** (2003) 027, [arXiv:hep-ph/0208156](#).
- [40] L. Mangano, M. Moretti, F. Piccini, et al., “ALPGEN, a Generator for Hard Multiparton Processes in Hadronic Collisions,” *JHEP* **0307:001** (2003) 001, [arXiv:hep-ph/0206293](#).
- [41] G. Marchesini et al., “HERWIG: A Monte Carlo Event Generator for Simulating Hadron Emission Reactions with Interfering Gluons. Version 5.1 ,” *Comput. Phys. Commun.* **67** (1991) 465–508.
- [42] J. M. Campbell, J. W. Huston, and W. J. Stirling, “Hard Interactions of Quarks and Gluons: A Primer for LHC Physics,” *Reports on Progress in Physics* **70** (2007) 89.
- [43] G. Altarelli and G. Parisi, “Asymptotic Freedom in Parton Language,” *Nucl. Phys. B* **126** (1977) 298–318.
- [44] S. Catani, F. Krauss, R. Kuhn, and B. Webber, “QCD Matrix Elements + Parton Showers,” *JHEP* **11** (2001) 063, [arXiv:hep-ph/0109231](#).
- [45] F. Krauss, “Matrix Elements and Parton Showers in Hadronic Interactions,” *JHEP* **08** (2002) 015, [arXiv:hep-ph/0205283](#).
- [46] M. L. Mangano, M. Moretti, and R. Pittau, “Multijet Matrix Elements and Shower Evolution in Hadronic Collisions: $Wb\bar{b} + n$ Jets as a Case Study,” *Nucl. Phys. B* **632** (2001) 343–362, [arXiv:hep-ph/0108069](#).
- [47] M. Mangano, M. Moretti, F. Piccinini, and M. Treccani, “Matching Matrix Elements and Parton Shower Evolution for top-quark Production in Hadron Collisions,” *JHEP* **01** (2007) 013, [arXiv:hep-ph/0611129](#).
- [48] J. Alwall, S. Hoeche, F. Krauss, et al., “Comparative Study of Various Algorithms for the Merging of Parton Showers and Matrix Elements in Hadronic Collisions,” *Eur. Phys. J. C.* **C53** (2008) 473–500, [arXiv:hep-ph/0706.2569](#).
- [49] J. Alwall, S. de Visscher, and F. Maltoni, “QCD Radiation in the Production of Heavy Colored Particles at the LHC,” *Journal of High Energy Physics* **2009** (2009) 017, [arXiv:hep-ph/0810.5350](#).
-

- [50] CMS Collaboration, “Plans for Jet Energy Corrections at CMS,” *CMS PAS JME-07-002* (2008).
 - [51] N. Amapane, R. Bellan, S. Bolognesi, et al., “Local Muon Reconstruction in the Drift Tube Detectors,” *CMS NOTE -2009/008* (2009).
 - [52] R. Fruehwirth, “Application of Kalman Filtering to Track and Vertex Fitting,” *Nucl. Instrum. Meth. A* **262** (1987) 444 – 450.
 - [53] Z. Hatherell, G. Karapostoli, M. Pioppi, et al., “Study of Isolation Properties of SUSY low- p_T Leptons,” *CMS AN-2009/0167* (2009).
 - [54] M. Mulders, I. Bloch, E. James, et al., “Muon Identification in CMS,” *CMS AN-2008/098* (2008).
 - [55] S. Baffioni, C. Charlot, F. Ferri, et al., “Electron Reconstruction in CMS,” *CMS NOTE 2006/040* (2006).
 - [56] R. Fruehwirth and T. Speer, “A Gaussian-Sum Filter for Vertex Reconstruction,” *Nucl. Instrum. Meth A* **534** (2004) 217–221.
 - [57] CMS Collaboration, “ E_T Performance in CMS,” *JME-07-001* (2007).
 - [58] CMS Collaboration, “The Trigger and Data Acquisition Project - Technical Design Report,” *CERN/LHCC 2002-026 2* (2002).
 - [59] B. C. Allanach, “SOFTSUSY: A C++ Program for Calculating Supersymmetric Spectra,” *Comput. Phys. Commun.* **143** (2002) 305–331, [arXiv:hep-ph/0104145](#).
 - [60] A. Djouadi, M. M. Muehlleitner, and M. Spira, “Decays of Supersymmetric Particles: the Program SUSY-HIT (SUspect-SdecaY-Hdecay-InTerface),” *ActaPhys.Polon* **B38** (2006) 635–644, [arXiv:hep-ph/0609292](#).
 - [61] D. R. Stump, “A New Generation of CTEQ Parton Distribution Functions with Uncertainty Analysis,” *Nuclear Physics B - Proceedings Supplements* **117** (2003) 265 – 267.
 - [62] D. Acosta, F. Ambrogini, P. Bartalini, et al., “The Underlying Event at the LHC,” *CMS NOTE 2006-067* (2006).
 - [63] C. Collaboration, “CMS High Level Trigger,” *CERN-LHCC-2007-021* (2007).
 - [64] CMS Collaboration, “Search Strategy for Exclusive Multi-Jet Events from Supersymmetry at CMS,” *CMS PAS SUS-09-001* (2009).
 - [65] L. Randall and D. Tucker-Smith, “Dijet Searches for Supersymmetry at the LHC,” *Phys. Rev. Lett.* **101** (2008) [arXiv:hep-ph/0806.1049](#).
 - [66] CMS Collaboration, “SUSY Searches with Dijet Events,” *CMS PAS SUS-08-005* (2008).
 - [67] CMS Collaboration, “Study of Hadronic Event-Shape Variables,” *CMS PAS QCD-08-003* (2008).
-

- [68] G. Punzi, “Sensitivity of Searches for New Signals and its Optimization,” *Statistical Problems in Particle Physics, Astrophysics, and Cosmology, Proceedings of the PHYSTAT 2003 Conference held 8-11 September (2003)* 79.
- [69] CMS Collaboration, “Initial Measurement of the Inclusive Jet Cross Section at 10 TeV with CMS,” *CMS PAS QCD-08-001* (2009).
- [70] CMS Collaboration, “Prospects for the First Measurement of the $t\bar{t}$ Cross Section in the Muon-Plus-Jets Channel at $\sqrt{s} = 10\text{TeV}$ with the CMS Detector,” *CMS PAS TOP-09-003* (2009).
- [71] CMS Collaboration, “Towards a Measurement of the Inclusive $W \rightarrow e\nu$ and $\gamma^*/Z \rightarrow e^+e^-$ Cross Sections in pp Collisions at $\sqrt{s} = 10\text{TeV}$,” *CMS PAS EWK-09-004* (2009).
- [72] Butterworth, J. M., et al., “The Tools and Monte Carlo Working Group Summary Report,” (2010) [arXiv:hep-ph/1003.1643](https://arxiv.org/abs/1003.1643).
- [73] CMS Collaboration, “Measuring Electron Efficiencies at CMS with Early Data,” *CMS EGM-07-001* (2008).
- [74] D. Acosta, P. Bartalini, A. Drozdetskiy, et al., “Measuring Muon Reconstruction Efficiency from Data,” *CMS NOTE 2006/060* (2006).
- [75] CMS Collaboration, “Measurement of the Jet Energy Resolutions and Jet Reconstruction Efficiency at CMS,” *CMS PAS JME-09-007* (2009).
- [76] CMS Collaboration, “Towards the Search for the Standard Model Higgs Boson Produced in Vector Boson Fusion and Decaying into a tau Pair in CMS with 1 Inverse Femtobarn: tau Identification Studies,” *CMS PAS HIG-08-001* (2008).
- [77] CMS Collaboration, “Data-Driven Estimation of the Invisible Z Background to the SUSY MET Plus Jets Search,” *CMS PAS SUS-08-002* (2008).
- [78] R. Cousins, J. Linnemann, and J. Tucker, “Evaluation of Three Methods for Calculating Statistical Significance when Incorporating a Systematic Uncertainty into a Test of the Background-Only Hypothesis for a Poisson Process,” *Nucl. Instrum. Meth. A* **595** (2008) 480–501.
- [79] T. Li and Y. Ma, “Analysis Methods for Results in Gamma-Ray Astronomy,” *The Astrophysical Journal* **272** (1983) 317–324.

Acknowledgements

In the first place I would like to thank Prof. Dr. Claude Amsler for giving me the opportunity, the freedom and the necessary support to pursue my thesis. Whereas this work is concerned with a very particular field of particle physics his extensive knowledge about general physics helped me to keep in mind the greater picture. I am especially grateful that he gave me the opportunity to study and work at CERN and to experience the start-up of a new particle collider. I am also much obliged to Prof. Dr. Vincenzo Chiochia who shared his knowledge about the intricate details of the CMS pixel detector and who gave me the chance to participate in the very first commissioning of the pixel detector with cosmic ray muons.

A special thanks goes to all those people with whom I worked on the SUSY analysis described in this thesis. To Oliver Buchmueller who first suggested an α_T based di-jet analysis and whose ability to motivate people I admire, to Markus Stoye who never accepted (too) simple answers and who never failed to spot the weak link in an argumentation, to Henning Flächer who managed to keep a clear head even in busy times and to Rob Bainbridge, Tom Whyntie, Jad Marrouche and to all those who joined later, it was a pleasure working with you!

I am also grateful to the referees of our publications, especially to Gigi Rolandi, for insisting on a tight scrutiny of our analysis approach. In the end this really helped us to gain more insight into the power of our final selection variables. I also want to thank Prof. Luc Pape and Dr. Filip Moortgaat with whom I first discussed the concept of a data-driven estimation of the QCD background. The ratio method described in this thesis was ultimately inspired by this exchange. For his help with the statistical approach to this method I am much obliged to Louis Lyon. Furthermore I am grateful to Simon de Visscher whose help with event generator issues and his willingness to discuss and explain I appreciate. I would also like to thank all the members of the CMS collaboration, who build the CMS detector and who contributed to the software used within this analysis.

Thanks also to the whole University of Zurich CMS group for the friendly atmosphere they provided. A special thanks goes to my former and more recent office mates Enver Alagoz, Barbara Millan and Andreas Jäger for the fruitful discussions as well as the kind distractions and most of all for their helpfulness, it was a good time! I wish you all the best and good luck with your own thesis!

Last but in no way least I want to express my gratitude to my parents and to the person with whom I shared my flat and my life in the last four years. The one who messed up the flat when it looked far to tidy and who was there when I needed him the most. Thanks!